The high pressure phase transformations of silicon and germanium at the nanoscale

Larissa Q. Huston

A thesis submitted for the degree of
Doctor of Philosophy in Physics at
The Australian National University

March, 2019

Declaration

This thesis is an account of research undertaken between March 2015 and March 2019 at Department of Electronic Materials Engineering, Research School of Physics and Engineering, College of Science, The Australian National University, Canberra, Australia.

Except where acknowledged in the customary manner, the material presented in this thesis is, to the best of my knowledge, original and has not been submitted in whole or part for a degree in any university.

Larissa Huston
March, 2019

Acknowledgements

This work would not have been possible without the guidance of my supervisors Prof Jodie Bradby, Prof Jim Williams and Dr Bianca Haberl. I thank them for providing me with this wonderful project and also giving my the opportunities and freedom to explore my own ideas. I also thank them for their genuine interest in helping me grow as a scientist. I would like to thank Jodie for helping me smoothly transition into my PhD by ensuring that I had a good working environment, help to learn the required technical skills, encouragement to participate in outreach, and support since the beginning of my PhD. During my time at ANU, I have learned the importance of good culture in the workplace and would like to thank Jodie for her leadership of our group which has made it a productive, open and friendly environment. I am thankful for Jim's patience (especially with my typos), his discussions, his time, and his open-mindedness to my sometimes unusual ideas. I would like to thank Bianca for supporting me from afar, especially via email discussions but also being great support during my long term visit to the USA.

I would like to thank Ao.Univ.Prof. Dr. Alois Lugstein from TU Wien in Austria for growing many of the nanowires samples and for his enthusiasm and support throughout my project. I would also like to thank Dr Manfred Reiche from the Max Planck Institute of Microstructure Physics for fabrication the etched Si nanowires and Dr Clemens Zeiner (TU Wien) for processing the Ge nanowires.

My thanks goes to Dr Brett Johnson (University of Melbourne) for removing the Au from the SiNWs in Chapter 4 and 5 and Leonardus Bimo Bayu Aji for providing me with the a-Si sample used in Chapter 5. I would also like to thank Prof Jodie Bradby and Dr Thomas Shiell for performing the XRD measurements in Chapter 3, Dr Sherman Wong for collecting the XRD of the samples I made (Fig. 4.1 and 5.2), and Lachlan Smillie for performing the transmission electron microscopy in Chapter 6.

Throughout my project, I have required training for the use of many instruments and techniques. I would thus like to thanks the following people for patiently sharing their expertise with me: Dr Kiran Mangalampalli (high and low nanoindentation stages), Dr Felipe Kremer (transmission electron microscopes) and Lachlan Smillie (focused ion beam). I would like to thank Dr Tuan Thien Tran for fabricating the devices used for electrical nanoindentation measurements which were not included in the thesis.

During my PhD, I had the pleasure of visiting the High Pressure Collaborative Access Team (HPCAT) at the Carnegie Institute of Washington in Argonne National Laboratory. I would like to thank Dr Guoyin Shen for hosting me HPCAT. It was a pleasure to work with him and I appreciate his discussion and sharing of his wisdom This trip could not have been a success without the technical support from Dr Jesse Smith, Dr Ross Hrubiak, Curtis Kenney-Benson, Rich Ferry, Eric Rod, Dr Changyong Park, Dr Stanislav Sinogeikin and Dr Cheng Ji. Part of this trip also involved a trip to Oak Ridge National lab where transmission electron microscopy of the nanowires compressed at high

temperature. I would like to thank Dr David Cullen for performing the transmission electron microscopy, and Dr Donovan Leonard, Dorothy Coffey and Shawn Reeves for help with sample preparation. I would also like to thank Dr Sergey Tkachev from GSECARS, Argonne National Laboratory for gas loading *a lot* of diamond anvil cells for me. Finally, I would like to thank Freda Humble, Dr Ross Hrubiak and Matthew Diamond for making me feel welcome at HPCAT.

I would like to thank all of my funding sources who made this work possible. I would like to thank the Australian Research Council for providing funding for my project and the Australian Government Research Training Program for providing me with a stipend. I am grateful for the financial support for this trip that I received from the Australian Nanotechnology Network and the Robert and Helen Crompton Award who made my extended trip to HPCAT possible. The work in section 4.5 was supported by the The International Synchrotron Access Program (ISAP) administered by the Australian Synchrotron. I would like to thank the various funding sources for the user facilities that I accessed. HPCAT operations are supported by DOE-NNSA's Office of Experimental Sciences. Use of the COMPRES-GSECARS gas loading system was supported by COMPRES under NSF Cooperative Agreement EAR -1606856 and by GSECARS through NSF grant EAR-1634415 and DOE grant DE-FG02-94ER14466. This research used resources of the Advanced Photon Source, a U.S. Department of Energy (DOE) Office of Science User Facility operated for the DOE Office of Science by Argonne National Laboratory under Contract No. DE-AC02-06CH11357. Electron microscopy of the Si nanowires in Chapters 4 and 5 was conducted at the Center for Nanophase Materials Sciences, which is a DOE Office of Science User Facility. The authors would like to thank AFAiiR (for ion implantation), the ANU node of Microscopy Australia (for transmission electron microscopy) and the Australian National Fabrication Facility (focused ion beam and scanning electron microscopy) for use of their facilities and technical support.

Ordinarily an acknowledgement for figures would be warranted, but in this work all figures are original.

I would like to acknowledge all the members (former and current) of my research group for their help, support and fruitful discussions over the years. Thank you to Toby Hendy, Xingshuo Huang, Shao Qi Lim, Dr Kiran Mangalampalli, Dr Christian Notthoff, Dr Thomas Shiell, Lachlan Smillie, Chris Tanner, Dr Tuan Thien Tran, Dr Sherman Wong, and Dr Wenjie Yang. Additionally, I would like to thank all my colleagues from EME, particularly Julie Arnold, for always being happy to help.

Finally I would like to acknowledge my family (Siau Goh, David Huston, Clarice Huston) and partner (Lachlan Smillie) for their love, believing in me, and being there for me in both good and bad times. I would additionally like to thank my dad for his help with proofreading.

Abstract

Semiconducting materials are critical for the electronics industry with the two most important semiconductors being Si and Ge. Most Si and Ge has a diamond cubic (dc) structure. However, many other phases of Si and Ge that are accessible via the application of high pressure. Compression to 10-11 GPa leads to both Si and Ge phase transforming to a metallic (β-Sn) structure. On decompression, the β-Sn phase transforms into one of several metastable phases; bc8-Si, r8-Si, hd Si and Ge, and st12-Ge depending on a number of factors including temperature, decompression rate and shear.

The difference between nanoscale and bulk behaviour is a recurring theme of materials science over the past decades. However, this effect has not been investigated with respect to high pressure phase transformations of Si and Ge. To determine the effect of size on the phase transformations of Si and Ge, nanowires (NWs) were compressed and low load nanoindentation was performed. By using these two methods, other effects such as large pressure gradients in a sample and interaction with an underlying substrate could be probed. To add further understanding, the effect of temperature and decompression rate on these small volumes of Si and Ge is also investigated. To study the effects of size SiNWs of two sizes (80-150 nm and 200-250 nm) and GeNWs (40-60 nm) in diameter were compressed using a diamond anvil cell, and low load nanoindentation of Si and Ge was performed at various temperatures and decompression rates. The materials were analysed using x-ray diffraction, Raman spectroscopy, and transmission electron microscopy.

At ambient temperature that both sets of SiNWs experienced a suppressed dc-Si to β-Sn-Si phase transformation, with some of the smaller diameter SiNWs observed to phase transform directly to sh-Si. On decompression β-Sn-Si was found to persist until lower pressures than in bulk-Si, and a-Si was the dominant end phase. These suppressed phase transformations were attributed to the small size of the SiNWs making nucleation of new crystalline phases difficult.

The effect of temperature on the high pressure phase transformation of the SiNWs was also investigated. Temperature was found to have a significant impact on the end phases formed. At low temperatures, a-Si was the dominant end phase, at moderate temperatures bc8-Si and dc-Si were present, and at the high temperatures dc-Si was the dominant end phase. This behaviour differed to bulk Si.

Nanoindentation at ambient temperature and 105°C was performed, noting that the phase transformed material volume is also small. At low temperatures, a-Si was the dominant end phase. At the 105°C, a-Si was the dominant phase for fast unloading, however the portion of r8/bc8-Si increased with the next lowest unloading rate. For indents in dc-Si at the slowest unloading rate, the only end phase observed was dc-Si. This phase may have formed via nucleation and growth from the underlying crystalline substrate.

A similar study was performed on Ge. Like in Si, the dc-Ge to β-Sn-Ge phase transformation was suppressed on compression and β-Sn-Ge persisted until lower pressures

than bulk. The end phases of GeNWs were found to be a-Ge, hd-Ge, and dc-Ge. For nanoindentation of Ge, it was found that lowering the temperature of nanoindentation promotes the formation of r8-Ge and a-Si end phases instead of defective dc-Ge at ambient temperature.

These results further the understanding on how size, temperature and decompression affect the pressure induced phase transformation pathways of Si and Ge are formed. These results are of technological significance as the synthesis of near phase pure nanowires should allow for the testing of their properties.

List of Publications

[1] L. Q. Huston, A. Lugstein, J. S. Williams, and J. E. Bradby, "The high pressure phase transformation behavior of silicon nanowires," *Applied Physics Letters*, vol. 113, no. 12, p. 123103, 2018.

[2] L. Q. Huston, B. C. Johnson, B. Haberl, S. Wong, J. S. Williams, and J. E. Bradby, "Thermal stability of simple tetragonal and hexagonal diamond germanium," *Journal of Applied Physics*, vol. 122, no. 17, p. 175108, 2017.

[3] L. Q. Huston, M. S. R. N. Kiran, L. A. Smillie, J. S. Williams, and J. E. Bradby, "Cold nanoindentation of germanium," *Applied Physics Letters*, vol. 111, no. 2, p. 021901, 2017.

[4] D. H. Yu, M. Avdeev, D. H. Sun, L. Q. Huston, T. B. Shiell, Q. B. Sun, T. Lu, Q. Gu, H. Liu, J. E. Bradby, N. Yie, Y. Liu, J. Y. Wang, and G. J. McIntyre, "Understanding the Unusual Response to High Pressure in KBe2BO3F2," *Scientific Reports*, vol. 7, 2017.

[5] Q. Sun, C. Zheng, L. Q. Huston, T. J. Frankcombe, H. Chen, C. Zhou, Z. Fu, R. L. Withers, L. Norén, J. E. Bradby, J. Etheridge, and Y. Liu, "Bimetallic ions codoped nanocrystals: Doping mechanism, defect formation, and associated structural transition," *The Journal of Physical Chemistry Letters*, vol. 8, no. 14, pp. 3249–3255, 2017.

[6] Q. Sun, L. Q. Huston, T. J. Frankcombe, J. E. Bradby, T. Lu, D. Yu, C. Zhou, Z. Fu, and Y. Liu, "Trans-regime structural transition of (In3+ + Nb5+) co-doped anatase TiO2 nanocrystals under high pressure," *Crystal Growth & Design*, vol. 17, no. 5, pp. 2529–2535, 2017.

[7] T. T. Tran, H. S. Alkhaldi, H. H. Gandhi, D. Pastor, L. Q. Huston, J. Wong-Leung, M. J. Aziz, and J. S. Williams, "Suppression of ion-implantation induced porosity in germanium by a silicon dioxide capping layer," *Applied Physics Letters*, vol. 109, no. 8, p. 082106, 2016.

[8] L. Q. Huston, A. Lugstein, G. Shen, D. A. Cullen, B. Haberl, J. S. Williams, and J. E. Bradby, "Synthesis of novel phases in Si nanowires using controlled pressurization pathways and temperature," 2019. Under preparation.

[9] L. Q. Huston, A. Lugstein, G. Shen, D. A. Cullen, B. Haberl, J. S. Williams, and J. E. Bradby, "Pressure-induced phase transformations in small volumes of si," 2019. Under preparation.

Contents

List of Figures

List of Tables

List of Abbreviations

Phases of silicon and germanium

a-Si/Ge	Amorphous Si/Ge
bc8-Si/Ge	Body Centred Cubic, 8 atoms per unit cell Si/Ge
dc-Si/Ge	Diamond Cubic Si/Ge
r8-Si/Ge	Rhombehedral, 8 atoms per unit cell Si/Ge
st12-Si/Ge	Simple Tetragonal, 12 atoms per unit cell Si/Ge

Techniques/Other

BF	Bright Field
DAC	Diamond Anvil Cell
DF	Dark Field
FIB	Focussed Ion Beam
GeNWs	Germanium nanowires
HRTEM	High Resolution Transmission Electron Microscopy
SEM	Scanning Electron Microscopy
SADP	Selected Area Diffraction Pattern
SiNWs	Silicon nanowires
TEM	Transmission Electron Microscopy
XRD	X-Ray Diffraction
XTEM	Cross-sectional Transmission Electron Microscopy

Chapter 1

Introduction

During the past century, semiconducting materials such as Si and Ge have become critical for society. These materials are the basis of a wide range of applications such as computing and solar cells. Si is the most widely used semiconducting materials due to its abundance, non-toxicity, and low cost. However, the use of Si is limited by some its properties (such as an indirect band gap) which arise from its diamond cubic (dc) crystal structure. One way to alter the properties is to change the crystal structure; this can be done using high pressure,[1] and growth.[2]

High pressure can induce phase transformations in materials allowing for the creation of new crystal structures.[3] Phase transformations can be either reversible or irreversible. Some irreversible phase transformations results in phases that are metastable– stable at ambient pressure, despite not being the thermodynamically favoured phase. Si and Ge are two examples of materials, where metastable phase can be formed via high pressure.[4–6] Some of the metastable phases of Si and Ge have properties of interest making them potential candidates for technological applications such as electronic devices or solar cells.[7,8]

Research on high pressure induced phase transformations of Si dates back to 1962 when a sudden drop in resistivity was observed when loading dc-Si to high pressure.[9] This was attributed to a phase transformation from the commonly known semiconducting phase (dc-Si) to a new metallic structure. This metallic structure has the same crystallographic structure as white tin (β-Sn, $I4_2/amd$).[10] Many more metallic phases and a series of phases that are metastable at ambient pressure have since been discovered.[4,6,9–19] Similar phase transformations have also been discovered in Ge.[4,9,10,13,20–24] A comprehensive list of the known phases of Si and Ge, including their structure, spacegroup and their first observation, is provided in Table 1.1.

Several experimental methods can be used to generate sufficiently high pressures to cause phase transformations.[3,25] These include nanoindentation, diamond anvil cells (DACs), piston cylinders, and multianvil cells. This work will focus on DACs and nanoindentation. Figure 1.1 shows a basic schematic of how these apparatuses apply high pressure. DACs squeeze a small volume of material between diamonds.[3] Nanoindentation involves pressing a sharp tip into a material, creating high pressure in a small selected region of a sample.[25]

The final phase formed after decompression in Si and Ge is determined by a number of factors. These are the rate of increase/decrease in pressure, the hydrostaticity of pressure application, temperature, the presence of impurities and the size of the material used.

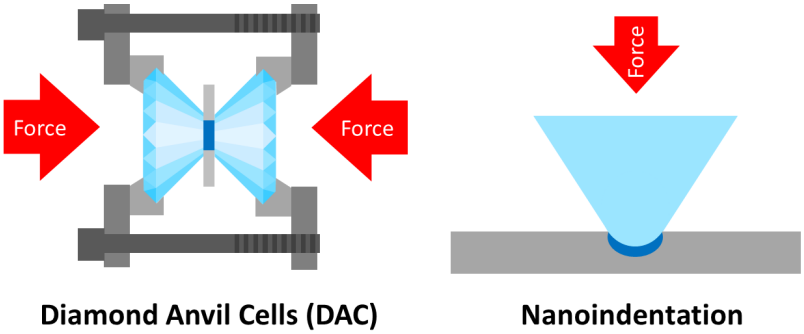

Figure 1.1: Two methods of inducing high pressure in materials, a diamond anvil cell and nanoindentation.

Table 1.1: The known structures of Si and Ge and their corresponding space groups and phase numbers (where applicable). The references within the table are when the phase was first discovered. Note that some phases have been assigned Roman numerals and these are shown where applicable. In this thesis the phases are referred to by their abbreviations (i.e. dc-Si)

Structure	Abbreviation	Space Group	Si	Ge
diamond cubic	*dc*	$Fd\bar{3}m$	Si-I	Ge-I
amorphous	*a*	N/A	N/A	N/A
white tin	β-Sn	$I4_1/amd$	Si-II[10]	Ge-II[9,10]
simple tetragonal	*st12*	$P4_32_12$	[11]	Ge-III[20]
body centred cubic	*bc8*	$Ia\bar{3}$	Si-III[4]	Ge-IV[21]
hexagonal diamond	*hd*	$P6_3/mmc$	Si-IV[12]	Ge-V[22]
simple hexagonal	*sh*	P6/mmm	Si-V[13]	[23]
orthorhombic	*Cmca*	Cmca	Si-VI[14]	[23]
hexagonal close packed	*hcp*	$P6_3/mmc$	Si-VII	[23]
tetragonal	*Si-VIII*	$P4_12_12$	Si-VIII[15]	-
tetragonal	*Si-IX*	$P4_222$	Si-IX[15]	-
faced centred cubic	*fcc*	$Fm\bar{3}m$	Si-X[16]	-
body-centered orthorhombic	Imma	Imma	Si-XI[17]	[18]
rhombohedral	*r8*	$R\bar{3}$	Si-XII[6]	[24]
unknown	*Si-XIII*	unknown	Si-XIII[19]	-

This thesis will focus on the effects of some of these factors including size, decompression rate and temperature. How these factors influence the phase transformation behaviour of different materials will be discussed later in this chapter (Section 1.4). The general high pressure phase transformation behaviour of Si and Ge will be discussed.

1.1 Phase transformations of silicon and germanium

This section summarises the pressure induced phase transformations of Si and Ge at ambient temperature. These measurements were typically made using DACs or similar high pressure equipment. More information about DACs is outlined in Section 2.1.2 of the following chapter.

1.1.1 Silicon

The series of known high pressure induced phase transformations in Si is shown in Fig. 1.2. Subjecting dc-Si, to ∼11.3 GPa of pressure causes it to phase transform to the metallic β-Sn structure.[10,26] This phase transition is known to be "sluggish",[21] due to the fact that it is a reconstructive phase transformation, meaning that bonds between atoms are broken and rearranged during the phase transformation, involving a ∼22% decrease in volume.[27] The dc-Si to β-Sn-Si phase transformation pressure measured experimentally is in good agreement with many theoretical studies.[27–29] At higher pressures, Si undergoes a series of reversible metal to metal phase transformations such as β-Sn to Imma at 13 GPa, Imma to simple hexagonal (sh) at 15 GPa. These two phase transformations are said to be displacive, involving a shift of some of the β-Sn-Si atoms to positions in the sh-Si unit cell, with the Imma phase being a transition structure.[27] The β-Sn, Imma and sh structure are also calculated to be similar in energy.[30] Sh-Si then transforms to Cmca-Si at 38 GPa, Cmca-Si to hcp-Si at 42 GPa and hcp-Si to fcc-Si at 79 GPa.[16,31] The fcc phase has been found to be stable up to 248 GPa.[32] During decompression, these phase transformations are found to be reversible until the β-Sn phase.[16,31] Figure 1.3 summarises the phase transformations observed on decompression (below 20 GPa). When decompressing from β-Sn-Si, Si does not revert back to its original dc structure phase, due to a large energy barrier, calculated to be ∼0.23 eV at 8 GPa.[28] Instead, β-Sn-Si phase transforms to r8-Si (rhombohedral 8 atoms per unit cell) at ∼10 GPa which transforms to bc8-Si (body centred cubic, 8 atoms per unit cell) at 3 GPa.[5,6] Theoretical modelling has indicated that β-Sn-Si phase transforms to r8-Si via a body centred tetragonal (bt8) phase which requires an activation energy of 0.16 eV at 8 GPa, a value much lower than the β-Sn-Si to dc-Si transition.[28] Two other tetragonal phases have also between reported to form during fast decompression from above ∼11 GPa, however these phases have not be reported since their initial observation.[15]

Amorphous Si (a-Si) has also been studied under high pressure where two different general behaviours have been observed.[33–37] The first of these is similar phase transformation behaviour to dc-Si.[33,34] In other studies, a-Si was found to undergo a sudden increase in density at ∼14 GPa, forming high density amorphous (HDA) Si. Upon decompression, HDA-Si phase transforms back to a low density amorphous (LDA) structure.[35–37] This discrepancy was later attributed to the presence of impurities contained within the a-Si starting materials.[38] This is described in more detail in section 1.3.

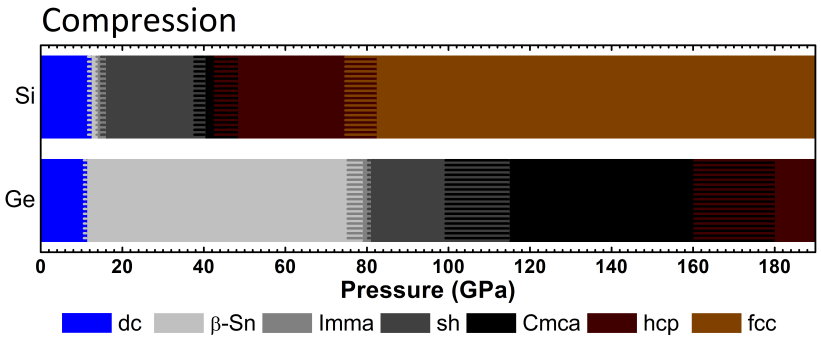

Figure 1.2: A summary of the high pressure phase transformations of Si and Ge during compression. The Si data is from Refs.[14,26,31,32] and the Ge data is from Refs.[13,18,23,39]. Note that when multiple phases are observed, inter-meshing horizontal lines of the appropriate colours are used.

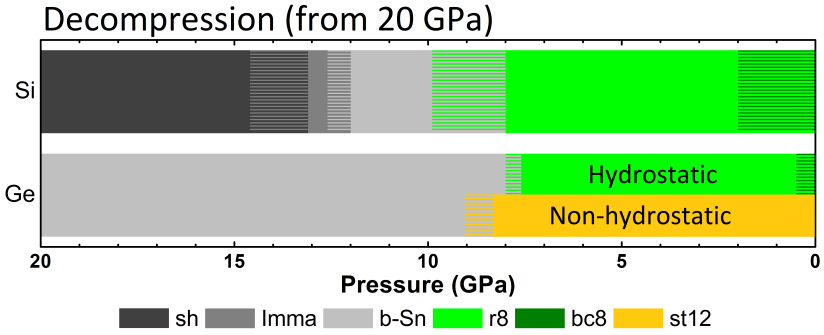

Figure 1.3: A summary of the high pressure phase transformations of Si and Ge during decompression below 20 GPa. The Si data is from Refs.[5,31] and the Ge data is from Ref.[40] Note that when multiple phases are observed, inter-meshing horizontal lines of the appropriate colours are used.

1.1.2 Germanium

The pressure induced phase transformations of Ge are broadly similar to those of Si as shown in Fig. 1.2 and 1.3. Dc-Ge phase transforms to β-Sn-Ge at a pressure of $\sim$10 GPa.[13] Further increasing the pressure results in phase transformations to metallic structure that are similar to those observed in Si except that β-Sn-Ge and the other metallic phases are stable until much higher pressures. The β-Sn to Imma phase transformation occurs at 75 GPa,[18] Imma to sh at 81 GPa,[39] sh to Cmca at 100 GPa[23] and Cmca to hcp at 170 GPa.[23] No further phase transformations in Ge have been observed up to 190 GPa.[23]

Similar to Si, all of the metal to metal phase transformations are reversible and until β-Sn-Ge. When β-Sn-Ge phase transforms on decompression, both bc8-Ge[21] and st12-Ge[4,20] are observed as end phases. The pathway to the bc8-Ge end phase involves the formation of the intermediate r8 phase between 9 GPa to 0.5 GPa.[40] Bc8-Ge was found to be unstable at ambient pressure and transform to the hexagonal diamond (hd-Ge) phase within days.[21,40] The main factor in determining the end phase of Ge that forms is thought to be the presence of shear. A highly hydrostatic unloading environment will cause β-Sn-Ge to transform to r8-Ge and a non-hydrostatic environment favours the formation

st12-Ge.[40]

Again like in Si, different high pressure behaviours have been reported in a-Ge. Some studies found that like dc-Ge, a phase transformation to β-Sn-Ge occurs on compression.[37,41–43] However other studies have reported that a-Ge undergoes a densification to HDA-Ge on compression.[44–47] Several different phase transformation pathways are reported to occur during decompression. These include phase transformation to st12-Ge[37,45,48] bc8-Ge[43,49,50] and dc-Ge,[41] from β-Sn-Ge and the formation of LDA-Ge from HDA-Ge.[44,45]

1.2 Properties and stability of metastable phases of silicon and germanium

Some of the phases of Si and Ge are stable at ambient temperature and have interesting properties. This section outlines the known and predicted properties and stability of different metastable phases of Si and Ge. Tables 1.2 and 1.3 provide a summary of the properties (1.2) and stability (1.3) of the various phases of Si and Ge which will now be summarised for each phase.

Table 1.2: A summary of the measured and theoretical properties of the metastable phases of Si and Ge.

Phase	Theory	Experimental
dc-Si		indirect band gap (1.1 eV[51])
bc8-Si	semimetal	direct band gap (0.03 eV[52])
r8-Si	indirect band gap (0.24 eV[7])	semiconductor[53] with good optical absorption[54]
hd-Si	indirect band gap (0.95 eV[55,56])	indirect band gap (<1 eV[8])
dc-Ge		indirect band gap (0.66 eV[51])
bc8-Ge	semimetal[57,58]	-
r8-Ge	semimetal[57]	-
hd-Ge	semimetal[7,59] or direct band gap semiconductor (0.55 eV[60])	-
st12-Ge	indirect band gap (0.54 eV[57])	indirect band gap (0.59 eV[61]

- **Bc8-Si** was recently reported to be a low direct band gap semiconductor with a band gap of 0.03 eV.[52] Theoretical studies report that bc8-Si is a semimetal[55] or a direct band gap semiconductor.[60] Theoretical work on bc8-Si nanoparticles suggests that they are a good candidate for multiple exciton generation solar cells.[63] Bc8-Si is stable at ambient temperature. Above 150°C, it phase transforms to hd-Si.[8,64,65] This phase transition has an activation energy of 1.6 eV.[22]

Table 1.3: The annealing behaviour of different phases of Si and Ge.

Phase	Transforms to	Temperature	Activation Energy
bc8-Si	hd-Si	200°C	1.6 eV[22]
hd-Si	dc-Si	740°C	5.9 eV[54]
bc8-Ge	hd-Ge	25°C	0.9 eV[22]
hd-Ge	dc-Ge	540°C	4.3 eV[62]
st12-Ge	dc-Ge	300°C	1.44 eV[62]

- A theoretical study reported that **r8-Si** has a large absorption in the solar spectrum.[7] As this phase has not yet been isolated at ambient temperature, no direct measurement of the absorption of this phase has been made. However, a recent study that measured the optical absorption of a thin film of a mixture of r8-Si and bc8-Si has yielded promising results with higher optical absorption than dc-Si.[54]

- **Hd-Si** is theoretically predicted to be an indirect band gap semiconductor with a band gap of 0.95 eV.[55,56] This band gap is predicted to become direct when subjected to strain.[56] An experimental study reported that hd-Si has an indirect band gap of <1 eV.[8] Hd-Si has been found to transform to dc-Si upon annealing at 750°.[22,54] This phase transformation has an activation energy of 5.9 eV.[54]

- **Bc8-Ge** is theoretically predicted to be either to have no band gap[60], or semimetallic properties.[57,58] Bc8-Ge is unstable at ambient temperature, phase transforming hd-Ge within hours.[21,22,40,66] This phase transformation has an activation energy of 0.9 eV.[22]

- No experimental measurements of the properties of **hd-Ge** have been made, however, theoretical studies predict a small overlap of band structure at 0.19 eV,[57] or a direct gap of 0.55 eV at the zone centre.[60] Hd-Ge phase transforms to dc-Si at 540°C with an activation energy of 4.3 eV.[62]

- It was recently reported that **st12-Ge** has an indirect band gap of 0.59 eV.[61] The st12 phase of Si has been predicted to have superconducting properties, possibly implying that st12-Ge might also have this property.[55,60]. St12-Ge phase transforms to dc-Ge at 300°C.[20,61,62,67] This phase transformation has an activation energy of 1.44 eV.[62] Interestingly, st12-Ge nanoparticles are more stable than bulk samples.[68]

1.3 Nanoindentation induced phase transformations

This section provides an overview of the deformation behaviour of Si and Ge via point loading via either indentation or nanoindentation. The earliest study to suggest phase transformations induced by indentation was by Gridneva in 1972.[69] Several years later Gerk and Tabor reported a correlation between the phase transformation pressure and the indentation hardness of a material.[70] The study of indentation-induced[i] phase trans-

[i]Note that most of the studies in this section use nanoindentation. The name nanoindentation can be misleading and is not just for nanosized forced and depths.

formations is complex. Unlike in high pressure cells, where all the material is subjected to pressure, there is material surrounding the indented region that is not under the same pressure. Because of this difference in the mechanism for inducing pressure, other deformation mechanisms such as cracking, crystalline defects and extrusion compete with phase transformation. The phase transformation behaviour of both Si and Ge during nanoindentation will be the focus of the next two sections.

1.3.1 Nanoindentation of silicon

Like in DACs, Si undergoes metallisation to β-Sn-Si during loading in nanoindentation.[71,72] This occurs in the small region underneath the tip where the pressure is sufficiently high enough for phase transformation to occur. This region will be referred to as the phase transformation zone. Weppelman et al.[73,74] found the dc to β-Sn phase transformation of Si to occur at 11.3 GPa by analysing the nanoindentation curves using contact mechanics. On unloading from β-Sn-Si, phase transformations to either a mixture of r8/bc8-Si or a-Si occur, depending on the unloading rate.[75,76] A slow unloading rate results in a mixture of ∼70% r8-Si and ∼30% bc8-Si.[77] This phase transformation was found to occur at 8.4 GPa.[73] The r8 phase, which is not typically observed after decompression is believed to be stabilised by residual pressure that is present after nanoindentation.[77] Fast unloading results in a-Si.[75,76]

In addition to phase transformation, crystalline defects occur underneath the phase transformation zone in an indent.[78–80] These defects arise due to the different components of stress under the tip (hydrostatic and shear). Hydrostatic components are believed to cause phase transformation whilst the shear component is said to promote the nucleation and propagation of defects.[81] The maximum hydrostatic component for a spherical tip occurs directly under the tip whilst the maximum shear component is found at a depth of half the radius of the tip.[76]

The deformation of a-Si via nanoindentation depends on the thermal history, purity and microstructure of the a-Si used.[82,83] When a-Si formed via ion implantation is nanoindented, deformation occurs via plastic flow and no phase transformation occurs.[82,84] However, a-Si can be heated to 450°C to "relax" the sample (i.e. reduce the number of dangling bonds, cause short range ordering).[85] When nanoindenting relaxed a-Si, phase transformation is observed, where the end phase is r8/bc8-Si.[82,84]

1.3.2 Nanoindentation of germanium

In general, phase transformations are more difficult to initiate in dc-Ge than in dc-Si at ambient temperature. Under nanoindentation, Ge usually deforms via the formation and propagation of "defects" such as slip and twinning.[86,87] This deformation mechanism has been observed using both spherical and Berkovich tips.[75,78,88] When the deformation occurs, the local pressure is reduced underneath the indentation tip and the critical pressure required for phase transformation is not reached.[86]

Phase transformation in dc-Ge has been reported in some cases that involve extreme loading conditions such as fast loading rates, high loads, very sharp tips, or cyclic nanoindentation.[87,89–91] Even under such conditions, phase transformation of dc-Ge in nanoin-

dentation does not have a 100% probability.[87]

In contrast to dc-Ge, a-Ge reliably results in phase transformation to β-Sn-Ge on loading and r8-Ge or dc-Ge during unloading.[24,92,93] This is presumably because the formation and propagation of crystalline based defects does not occur in an amorphous structure.[24,92,93]

1.4 Factors that influence phase transformation outcomes

The phase transformation pathways of Si and Ge are influenced by a number of factors including the presence of shear, the level of impurities, the decompression rate, temperature and small particle size. For both low temperatures and small particle sizes, the β-Sn-Si and Imma-Si phases are not observed during compression. Instead dc-Si directly phase transforms to sh-Si.[43,94] Furthermore, nanoparticles remained in the dc-Si phase until higher pressures than bulk-Si.[94] Upon decompression, both low temperature and the use of nanoparticles caused β-Sn-Si to remain until a much lower pressure than regular bulk-Si, and eventually phase transform to a-Si. Thus, it is clear that both temperature and particle size affects the phase transformation behaviour of Si. For the rest of this section, all the factors that influence the high pressure phase transformation behaviour of Si and Ge will be discussed in detail.

1.4.1 Shear

In Si, non-hydrostatic conditions, such as a DAC used without a hydrostatic pressure medium, lowers the onset of the dc-Si to β-Sn-Si phase transformation.[26]

The presence of shear is a key factor that influences the final phase formed after high pressure compression of Ge. When β-Sn-Ge is decompressed under hydrostatic conditions, r8-Ge forms and then transforms to bc8-Ge at 0.5 GPa. Under non-hydrostatic conditions, st12-Ge is the dominant end phase.[40] The use of a (non-hydrostatic) high pressure torsional device also resulted in the formation of st12-Ge at ambient temperature but bc8-Ge and a-Ge at lower temperatures.[95] This study concluded that both the presence of shear and thermal energy were required to promote the formation of st12-Ge.[95]

In nanoindentation, where phase transformation takes place, the bc8-Ge phase is usually observed, suggesting that nanoindentation is quite hydrostatic.[92] However, consistent with the DAC Ge results, st12-Ge has occasionally formed via nanoindentation and indentation using sharp tips such as a Berkovich tip or a Vickers tip.[87,96]

1.4.2 Presence of impurities

The presence of impurities, such as hydrogen, carbon and oxygen, has been found to influence the high pressure behaviour of Si in both DACs and nanoindentation. The results of several studies of a-Si under high pressure using DACs appeared to be inconsistent until the presence of impurities was considered.[38] For low to minimal impurity content, a-Si phase transforms similarly to dc-Si.[33,34] For high hydrogen content (5-12 at.%), a-Si

phase transforms to a HDA phase on compression and then back to a LDA phase on decompression occurs.[35–37] For a-Si with 1.8 at.% hydrogen, 0.9 at.% oxygen and 2 at.% argon, crystallisation to β-Sn-Si and then to an unknown phase occurs between 12.1 GPa and 15.8 GPa respectively on compression.[38] On decompression, β-Sn-Si gradually phase transforms to a-Si between 8 GPa and 0.7 GPa.[38]

The effect of impurities on the phase transformations of Ge has not yet been explicitly studied. However, the inconsistent behaviour of a-Ge under pressure (as outlined in Section 1.1.2),[37,41,44,45,48] would suggest that the presence of impurities has some effect on the phase transformations in a-Ge.

The presence of impurities also affects nanoindentation.[83,97] Studies of thin a-Si films implanted with hydrogen and oxygen reported different end phases compared with pure Si after nanoindentation.[83,97] A 2 at.% concentration of oxygen was found to prevent that formation of r8/bc8-Si most of the time.[83] A hydrogen impurity of 1 at.% inhibited the formation of r8/bc8-Si approximately half of the time.[97] From these studies, it is quite clear that the presence of impurities makes the formation of r8/bc8-Si in nanoindentation significantly more difficult.

1.4.3 Decompression/unloading Rate

Only a few studies have investigated the effect of the decompression rate on the phase transformations of Si using DACs. These studies report that rapid decompression of sh-Si results in amorphisation, whilst slow decompression lead to the formation of β-Sn-Si and then r8-Si.[33,34] It should be noted that both these studies used a-Si as a starting material.

The effect of the unloading rate for the nanoindentation of Si is well understood due to the ease of controlling the unloading time in experiments.[75,89,98] Multiple studies have reported the formation of r8/bc8-Si during slow unloading and the formation of a-Si during fast unloading.[75,89,98] This behaviour is thought to occur because the r8/bc8 phase takes time to nucleate, and when the pressure is lowered enough and r8/bc8-Si has not formed, β-Sn-Si becomes unstable and transforms to a-Si.[99]

The impact of both the loading and the unloading rate has also been studied for nanoindentation of Ge. Phases formed under high pressure (a-Ge and st12-Ge) have been observed using fast loading rates for both spherical and Berkovich tips.[87] When the loading rate was kept constant, fast unloading with a Berkovich tip resulted in the formation of r8-Ge and a-Ge in some indents.[90]

1.4.4 Temperature

Temperature clearly affects the end phases formed in Si on decompression. Instead of the bc8-Si phase that is formed upon unloading at ambient temperature, lowering the temperature of decompression to -155°C results in an a-Si end phase to form.[22,100] Between -155°C and 170°C, bc8-Si forms during unloading.[22] At higher temperatures (170-730°C), the final phase on unloading was reported to be dc-Si.[101] *In situ* studies of Si at high pressure have also been performed. Here, a direct phase transformation from r8-Si to dc-Si (instead of hd-Si) occurs at 10 GPa, 255°C.[102]

The phase transformations of Ge are also affected by temperature.[21,22,50,103] At ambient temperature, the end phase of Ge after decompression is either bc8-Ge or st12-Ge.[21,22] At lower temperatures (-55°C to -110°C) pure bc8-Ge forms.[21,22] At even lower temperatures (-110°C to -140°C), a mixture of bc8-Ge and a-Ge forms. Below -170°C, only the amorphous phase formed.[22,50] A series of *in situ* high temperature studies were also performed on Ge.[101,103] These studies found that at high temperature above 500°C, dc-Ge would melt under compression and then resolidify on decompression.[103] Between 120°C and 500°C, the β-Sn-Ge to dc-Ge transformation was found to be reversible with some hysteresis. St12-Ge was found to form up to around 50°C during decompression.[101].

Temperature also affects the phase transformation of Si via nanoindentation. Whilst indenting at or slightly above room temperature leads to phase transformation, increasing the temperature of indentation eventually leads to other modes of plastic deformation such as twinning and fracture becoming increasingly dominant.[1] The temperature at which this transition to other modes of deformation occurs at is dependent on the geometry of the indentation tip.[1] Studies that used large Vickers and pyramidal indenters reported phase transformation at 20-300°C,[75] and twinning above 350°C.[104–106] A study involving nanoindentation with a Berkovich indenter found that phase transformation occurs below 150°C, twinning and phase transformation both occur at 150-200°C, and only twinning occurs above 200°C.[107]

The effect of temperature on the nanoindentation behaviour of Ge has not been studied. Given that the temperature does have a significant effect on Si, it is likely to also affect Ge.

1.4.5 Size

There are currently only a few studies that have investigated the behaviour of nanoscale volumes of Si under high pressure.[94,108–110] The first of these studies found that 10-50 nm Si nanoparticles remain in the dc phase until much higher pressures than bulk Si.[94] Another study found that 7 nm diameter nanowires (NWs) remain dc-Si up to 15 GPa.[108] As both these studies found that dc-Si remains present until much higher pressure than bulk-Si, it would appear that there is difficulty in nucleation the β-Sn-Si phase. Interestingly, 60-80 nm diameter SiNWs undergo phase transformation to β-Sn-Si at a lower pressure than bulk Si. In this study, decompression was not reported.[109] Finally, 50-700 nm diameter SiNWs were observed to phase transform almost exactly like bulk Si during both compression and decompression.[110] Unlike bulk-Si and the 50-700 nm diameter SiNWs, the 10-50 nm nanoparticles phase transformed to a-Si on decompression, suggesting that the r8-Si phase is difficult to nucleate in small volumes.[94] These studies appear to have somewhat contradictory result and therefore the phase transformation pathways and the end phase of SiNWs/nanoparticles are not clear.

There is some evidence of a size dependence on the high pressure phase transformation behaviour of Ge. Very small Ge nanoparticles of <5 nm in size undergo pressure induced amorphisation to a metallic amorphous phase on compression.[111] Whilst matrix free nanoparticles of intermediate sized have not been compressed, polycrystalline Ge with crystal sizes between 13-100 nm has an elevated dc-Ge to β-Sn-Ge phase transformation.[112] A study of $\sim$80 nm diameter Ge nanowires (GeNWs) reported that the dc-Ge

to β-Sn-Ge has a slightly lower onset pressure than bulk-Ge.[113] On decompression, dc-Ge was observed as the end phase.[113].

The effect of size of the nanoindentation phase transformation volumes of Si has not directly been studied. However, it appears that smaller phase transformation volumes are more likely to phase transform to a-Si.[80] Comparing studies of large indents with studies using small indents hints at a size dependence. For example, it is possible to obtain 100% phase transformation to r8/bc8-Si when using large indenter tips ($\sim$21.5 μm diameter).[114] However with smaller indentation tips ($\sim$5 μm diameter), there is always a fraction of indents that contain a-Si.[80] Given that small volumes (nanoparticles) in a DAC also have an a-Si end phase,[94] the formation of a-Si in indentation might, in part, be due to the size of the phase transformation volume formed in nanoindentation. It would therefore be interesting to study the effect of the phase transformation volume size on the end phase.

1.5 Summary, directions, and aims of this thesis

This chapter has outlined the behaviour of Si and Ge under the application of pressure via DAC and nanoindentation, including the phase transformations that occur, the properties and stability of the phases that can be recovered at ambient pressure, and the factors that influence the phase transformation behaviour. A summary is provided in Table 1.4. This table shows that the effects of many of the factors that influence high pressure phase transformation behaviour of Si and Ge are not well understood. This thesis aims to address the lack of understanding of the influence of the size of the phase transformation volume and temperature on phase transformation behaviour of Si and Ge. The questions or areas studied are listed in blue in Table. 1.4.

The first point that this work will address is the size dependence of the high pressure phase transformations of Si. Currently, the studies that have investigated both compression and decompression report on either very small (10-50 nm) or near bulk (up to 700 nm) material.[94,110] Work on intermediate size ranges (80-500 nm) has at most only reported the behaviour on compression. This work aims to address this intermediate size range by studying the behaviour of SiNWs with two different intermediate diameter ranges: 80-150 nm and 200-250 nm.

Secondly, like in Si, there has been limited work on the effect of size on the high pressure phase transformations of Ge. Of these studies, only one study looked at the behaviour of GeNWs.[113] In this work, the high pressure behaviour of slightly smaller 40-60 nm diameter GeNWs is studied.

Thirdly, no work has investigated the temperature dependence of the nanoindentation behaviour of dc-Ge. Similar behaviour to the defect propagation observed in Ge at ambient temperature is observed in Si at high temperatures. Given the similarities between Si and Ge, one might expect some temperature dependence in the nanoindentation of Ge, particularly at lower temperatures.

As the suppression of nucleation of β-Sn-Si (on compression) and r8-Si (on decompression) is observed in 10-50 nm Si nanoparticles, this work will determine if factors that promote nucleation such as higher temperature and slow decompression can be used to promote nucleation of crystalline phases on decompression within small volumes (SiNWs).

Table 1.4: A summary of factors that influence the high pressure phase transformation behaviour of Si and Ge. Open questions are written in blue and italics.

Effect	DAC Si	DAC Ge	Nanoindention of Si	Nanoindention of Ge
Shear	High shear is found to lower the onset pressure of the dc-Si ⇒ β-Sn-Si phase transformation.[26]	On decompression: High shear: β-Sn-Ge ⇒ st12-Ge Low Shear: β-Sn-Ge ⇒ bc8-Ge[40]	High Shear: Extrusion in a-Si and r8-Si Low Shear: r8-Si	Sharp tips *may* induce phase transformation (β-Sn-Ge ⇒ r8-Ge or st12-Ge
Impurity Level	Phase transformation is suppressed at high impurity levels.[38,101]	–	Phase transformation is suppressed at high impurity levels.[83]	–
Strain Rate	Slow: β-Sn-Si ⇒ r8-Si ⇒ bc8-Si Fast: β-Sn-Si ⇒ a-Si[33,34]	Fast: st12 Slow: bc8 Also affected by shear.[40]	Slow: β-Sn-Si ⇒ bc8/r8-Si Fast: β-Sn-Si ⇒ a-Si[75,76]	No significant effect at room temperature.
Temperature	Very High: β-Sn-Si ⇒ dc-Si High: β-Sn-Si ⇒ hd-Si Ambient: β-Sn-Si ⇒ r8-Si ⇒ bc8-Si Low: β-Sn-Si ⇒ a-Si[22]	Very High: β-Sn-Ge ⇒ dc-Ge High: β-Sn-Ge ⇒ hd-Ge Ambient: β-Sn-Si ⇒ st12-Ge/ r8-Ge ⇒ bc8-Ge Low: β-Sn-Ge ⇒ a-Ge[22]	High: defect propagation[107] Ambient: bc8/r8-Si Low: a-Si	*Will lowering the temperature cause phase transformation?*
Size	Bulk: bc8-Si end phase *80-250 nm NWs:?* 10-50 nm: amorphisation on decompression *Will higher temperatures prevent amorphisation?*	<5 nm = pressure induced amorphisation[111] *40-60 nm NWs:?* 80 nm NWs: dc-Ge forms on decompression[113] 13-100 nm nanocrystals = higher transition pressure to β-Sn-Ge.[112]	There may be a size dependence for low loads. *Can this be confirmed?*	–

Variations of temperature can also be used to gain a better understanding of the effect of size in nanoindentation. The behaviour of Si under nanoindentation, using loads that cause phase transformed volumes that have a similar depth to the diameter of Si nanowires, will be monitored at different temperatures. This will give better insight on the effect of small volumes on phase transformation behaviour of Si using both methods of pressure application. This will lead to a better understanding of the size dependent behaviour observed in the nanoindentation of Si.

1.6 Thesis structure

This work is presented in the following chapters:

- **Chapter 2** discusses the methods used for both forming and characterizing the high pressures induced phases of Si and Ge.
- **Chapter 3** presents an investigation on the effect of size on the phase transformations of Si by compression SiNWs of different diameters.
- **Chapter 4** focuses on the effect of temperature on the phase transformations of bulk-Si and Si nanowires.
- **Chapter 5** compares the phase transformations of SiNWs to nanoindentation of bulk-Si with a similar size to the SiNWs.
- **Chapter 6** examines the phases transformations of GeNWs and the temperature dependence of the nanoindentation of Ge.
- **Chapter 7** outlines the conclusions and future directions for this work.

Chapter 2

Experimental Techniques

A variety of techniques were employed for the research presented in this thesis. Two different methods were used to apply pressure: nanoindentation and diamond anvil cells. Several techniques were used to characterise and determine the crystal structure and morphology of the samples. These were Raman spectroscopy, x-ray diffraction (XRD), scanning electron microscopy (SEM), and transmission electron microscopy (TEM). A focused ion beam (FIB) was used to prepare samples for TEM.

In this chapter, the general concepts involved in each of these techniques as well as more specific details of this work are provided.

2.1 Methods of producing high pressure

2.1.1 Nanoindentation

Indentation is a technique that is traditionally used to measure the hardness of materials. It involves pressing a tip with a specific shape (such as a sphere or pyramid) into a material and optically determining the area of the residual impression left by the tip. The hardness (H) is given by the maximum load (P_{max}) divided by the projected area of the residual impression (A_r). This is shown in eq. 2.1. Indentation is limited by the ability for an impression to be optically resolved and therefore is not useful for small materials or thin films.

$$H = \frac{P_{max}}{A_r} \tag{2.1}$$

For site specific hardness testing or the hardness testing for thin layers, very small tips with precise geometries and lower loads are needed. Nanoindentation involves the continuous sensing of depth penetrated by a tip when a load is applied. This allows for the testing of mechanical properties where spatial precision is required.[25,115] The force or the displacement with time can be controlled. An example of a function (in this case with the force varied with time) that is used is shown in Fig. 2.1 (a). It contains three sections, the application of force in a linearly increasing manner: loading, keeping the force constant: hold, and decreasing the force applied: unloading. Nanoindentation data are typically shown as a plot of load applied against the penetration depth. There are two distinct sections of the curve, the first section is the data taken during loading and the section is the data taken during unloading as indicated in Fig. 2.1 (b).

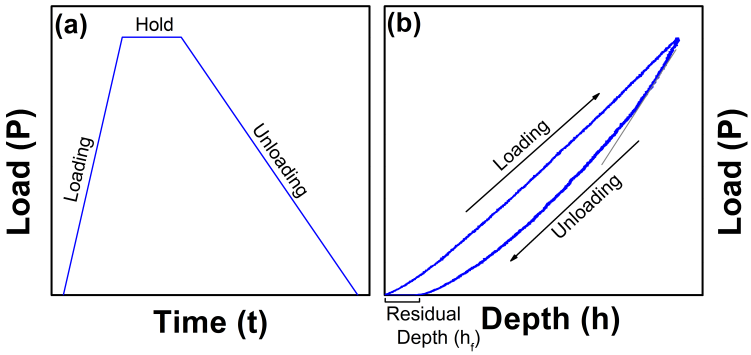

Figure 2.1: (a) An example of a nanoindentation load function. (b) A typical force-depth nanoindentation curve.

A nanoindentation load-depth curve can be used to extract both the hardness and Young's modulus of the material tested. The hardness of a material is calculated by using the load and contact area at the maximum depth (A_p) as described in Eq. 2.2. The stiffness of a material (S) is defined as the gradient of the unloading section of the curve (see eq. 2.3).[116] The stiffness can then be used to work out the reduced Young's modulus (E_r) of a material by using Eq. 2.4, where β is a geometric constant (which is $\sim$1) and $A_p(h_c)$ is the contact area of the tip at depth h_c.[116]

$$H_{IT} = \frac{P_{max}}{A_p} \tag{2.2}$$

$$S = \frac{dP}{dh} \tag{2.3}$$

$$E_r = \frac{1}{\beta}\frac{\sqrt{\pi}}{2}\frac{S}{\sqrt{A_p(h_c)}} \tag{2.4}$$

The reduced Young's modulus takes into account the Young's modulus of both the material being tested and the material of the tip (usually diamond). This value can be converted to Young's modulus of the test material (E) using eq. 2.5 where E_i and ν_i are the modulus and Poisson's ratio respectively for the indenter (usually diamond) and ν is Poison's ratio of the material being tested.

$$\frac{1}{E_r} = \frac{(1-\nu^2)}{E} + \frac{(1-\nu_i^2)}{E_i} \tag{2.5}$$

Whilst the traditional use of nanoindentation is the measurement of mechanical properties, nanoindentation systems have found uses in a wider variety of niche applications such as, tensile testing, microstrain testing of micropillars, the simulation of a pathogen attack on a plant cell, and for the creation of high pressure areas to cause phase transformation in material like in this work.[78,117–119]

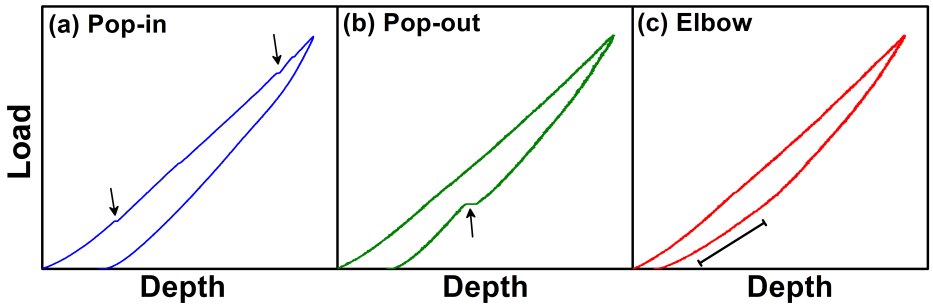

Figure 2.2: Typical load-depth curves from nanoindentation. (a) a curve showing "pop-in" behaviour, (b) a curve displaying "pop-out" behaviour and (c) a curve displaying elbowing.

Phase transformation behaviour during nanoindentation

In this work, nanoindentation is used generate localised high pressure in Si and Ge in order to induce phase transformation. Pressure on the order of 10 GPa is achievable during nanoindentation of Si and Ge, which is high enough for phase transformations to occur. It should be noted that other deformation mechanisms such as slip and the creation of defects can also occur in Si and Ge.[114]

Figure 2.2 shows examples of various features in indentation curves that can be indicative of phase transformations. These include "pop-in", "pop-out" and "elbow" behaviours. The "pop-in" event [Fig. 2.2 (a)] is a sudden increase in depth that occurs during loading. This could be caused by the material being deformed by slip or the material undergoing a phase transformation to a more dense phase. A "pop-out" [Fig. 2.2 (b)] is a sudden change in depth that occurs during unloading. This can occur when a material undergoes a sudden increase in volume such as when β-Sn-Si phase transforms to r8-Si which involves an 8% increase in volume.[5,6] Finally, the elbow [indicated by a black line in Fig. 2.2(c)] is a sudden change in the gradient of the unloading curve. This is can be indicative of phase transformation to an amorphous phase.[75]

Low temperature nanoindentation

To conduct nanoindentation at temperatures below ambient temperature requires a temperature controllable stage. A custom built stage was used in this work [Fig. 2.3]. This stage cools the sample by passing N_2 gas through a copper coil immersed in liquid N_2. The gas flows through the stage to cool it and the sample (which is adhered to the stage using thermally conductive silver paint). The temperature is measured using a thermocouple and is varied by changing the flow rate of the cooled N_2 gas.

The indentation chamber is purged with N_2 gas to remove the water vapour in the air to inhibit the formation of ice on the sample. Nevertheless, the formation of ice on the surface limits the temperature that can be reached in this set-up. This usually occurs at around -60°C, regardless of how long the N_2 has been flowing in the chamber. Additionally, as the temperature is lowered, vibrations from the N_2 flowing through the stage cause significant noise in the data (this becomes increasingly significant at and below -45°C).

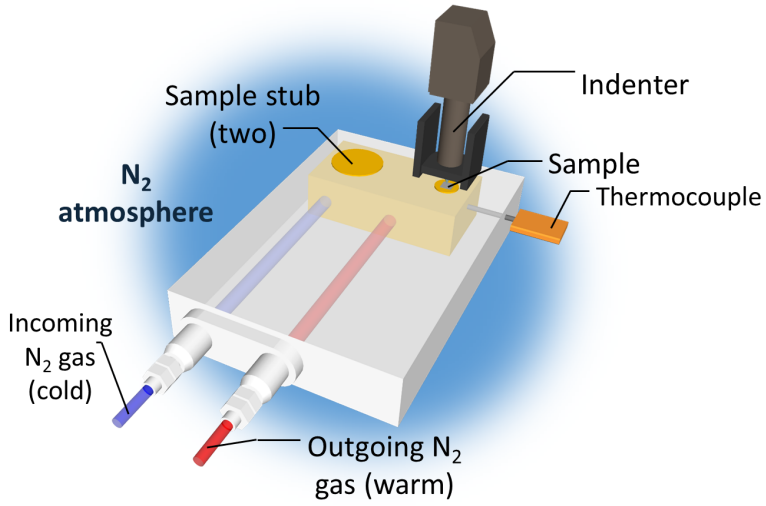

Figure 2.3: A schematic diagram of the stage used for low temperature nanoindentation. Low temperature N_2 gas is passed through the stage for cooling. N_2 is to dry the atmosphere to prevent to build formation of ice crystals.

High temperature nanoindentation

Nanoindentation at 25-250°C can also be performed using another custom built heating stage. This heating stage consists of a metal block which is heated using resistive heating, and a ceramic material that is cooled by water passing through it. The sample is mounted to the heating block using thermally conductive silver paint. As the top of the sample is exposed to air, it is expected that the sample will be slightly cooler than the heated metal block.

A water cooled shield is placed onto the nanoindenter to protect the electronics of the instrument from the heat. A special tip with an extra long shaft is required so that it fits

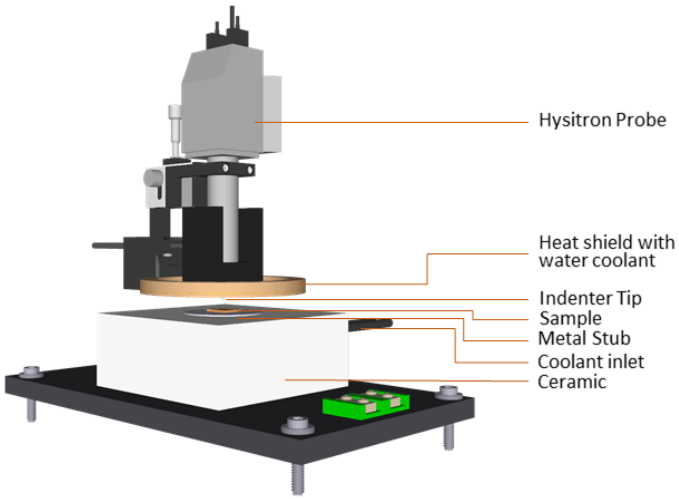

Figure 2.4: The components of the high temperature nanoindentation stage at ANU based on the design of Trenkle et al.[120]

through the shield and maintains distance between the heated sample and the electronics. This tip is not actively heated, thus sufficient time for the tip and sample to equilibrate is required.

Nanoindentation specific experimental details

All the nanoindentation work was performed using a Hysitron TI 950 Triboindenter equipped with a "TriboScanner" probe. The TriboScanner consists of a piezoelectric tube and a three-plate capacitative sensor.[121] The three-plate capacitive sensor is used to apply and measure force and displacement. The three-plate sensor consists of two fixed outer plates and one floating central plate. An AC signal is applied to each of the outer plates. This signal is 180° out of phase for each of the plates such that there is an electric field potential between the plates. This potential is zero at the centre of the plates. The middle plate is attached to the tip. This plate is allowed to change position and the voltage that it experiences varies as a function of position. The relationship between voltage and displacement of the middle plate is calibrated and thus displacement can be measured. To apply a force, a DC offset is applied to either the top or bottom fixed plate. This will cause the plate to be charged and attract the middle plate to the charged plate. This electrostatic attraction between the two plates is also calibrated and determines the force applied.

The entire Triboindenter is placed on a heavy granite block within an enclosed chamber. An active vibration isolation system is also used. This uses a combination piezoelectric accelerometers and electro-dynamic transducers to sense and actively dampen vibrations in the 1-200 Hz. Higher frequency vibrations are naturally dampened by the granite support of the system. Vibrations in the air are shielded by placing the system in the enclosure.

2.1.2 Diamond Anvil cells

A diamond anvil cell (DAC) is a small, conceptually simple, device used to induce high pressure in small samples. Force is applied to the two diamonds, pushing them together whilst holding material between them in a gasket. This is shown schematically in Fig. 2.5. DACs are capable of reaching much higher pressures compared to nanoindentation (which have an upper pressure limit that is essentially defined by the natural yielding processes of the material being tested).[115] A pressure medium (usually a liquid or gas) is often loaded into the gasket to cause the pressure to be applied evenly in all directions creating a quasihydrostatic environment.

Today, DACs are used to generate high pressure under a wide variety of conditions, techniques and applications. These include low and high temperatures, axial and radial probing, single crystal and powder XRD, spectroscopic techniques such as Raman and infrared spectroscopy, and laser heating.[3,122] These applications have specific design requirements and thus there are a large variety of DAC designs. In this work, two types of DACs are used: the symmetric cell and the Boehler (plate cell).[123,124]

A symmetric cell consists of a a piston that fits inside a cylinder containing a seat on each side. Seats are approximately conical pieces of material with a conical hole drilled in

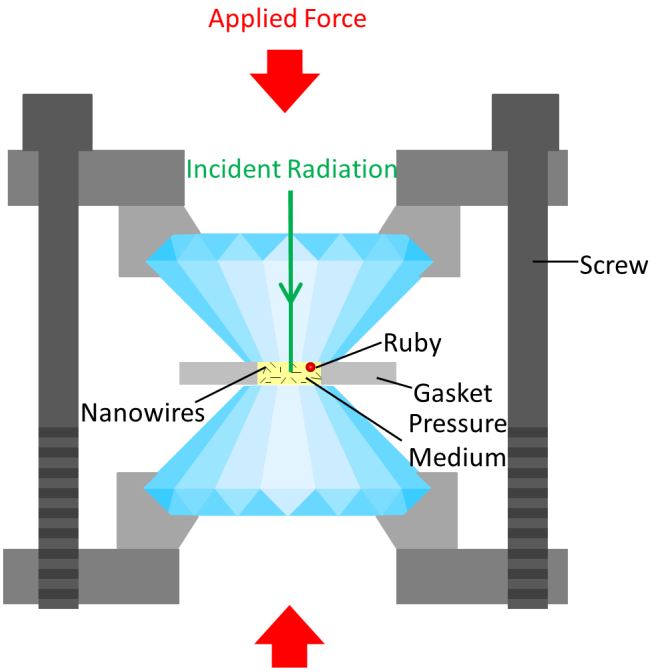

Figure 2.5: A schematic diagram of a diamond anvil cell

the middle. Diamonds are glued to these seats which are held in place with set screws that are used to adjust the alignment of the diamonds. The piston and cylinder are pushed together using screws, with each screw having numerous washers placed onto it. The screws apply a force on the diamonds and the washers help control the force applied.

The pressure that can be reached is determined by the size of the small flat surface at the tip of the diamond (known as the culet) as well as the configuration of the washers. A smaller culet size means that the force applied is concentrated on a smaller area, leading to higher pressures. Washers are conical (Belleville washers) in shape and act like a spring that resists the force applied by tightening the screws, allowing for more controlled pressure adjustments. The stacking configuration of the washers determines the amount of control one has on the pressure in the cell, as well as the range of pressures where pressure can be applied in a controlled manner. For example, having washers stacked in opposing directions will make the spring less stiff, allowing for finer control of the application of pressure, however, the washers will stop deforming elastically at lower pressures, meaning that pressure can only be applied in a controlled manner at low pressure.[125]

Boehler DACs (also known as plate DACs) apply force to the diamonds differently. These DACs consist of two plates with a seat and diamond positioned in the middle of each plate. Two sets of three concentric screws are used to align the diamonds (outside screws) and apply pressure (inside screws).[123] This type of cell relies on the deflection of a metal plates by the screws to push the diamonds together and apply pressure. The seats and diamonds of this type of cell are designed such that the diamond sits partially within the seat, allowing for a high opening angle which is usefully for x-ray diffraction.[123]

Gasket

The purpose of a gasket is to contain a material between the two diamonds, prevent the diamonds from touching, and to act as a supporting ring to reduce the concentration of stresses at the edge of the diamonds.[3] Gaskets usually have a starting thickness of 250-300 μm but are preindented by compressing them between the diamond anvils to a thickness of ∼15-60 μm, depending on the size of the culet. Preindentation reduces the outward plastic flow of the gasket during an experiment.[126] A hole, about 50% of the diameter of the culet, is drilled in the gasket to contain the sample.

A good material for a gasket is something that is hard but has a high enough compressibility such that pressure can be increased. For pressures below 40 GPa, T301 stainless steel is typically used. This material also has the advantage of being cheap. Tungsten is also useful for experiments at high temperatures due to its high melting point.[126] An x-ray transparent material such as beryllium or a mixture of amorphous boron and epoxy can be used as a gasket to allow for taking XRD measurements, through the gasket.[126]

Pressure media

Many DAC experiments are performed under near hydrostatic conditions where a pressure medium is used to evenly apply pressure to the sample.[3] Pressure media are chosen based on their availability, the pressure range at which the medium remains hydrostatic, the amount of interference their signal makes with the sample of interest, and their reactivity.

Organic liquids are some of the most readily available pressure media. The most common of these is a 4:1 mixture of methanol and ethanol. This pressure medium remains hydrostatic until 10.5 GPa.[127]

Condensed gases usually remain hydrostatic up to higher pressures than the 4:1 methanol/ethanol mixture. However, these are less accessible as they require a special apparatus to condense (either cryogenic or with high pressure) the gas into the DAC. An example of a condensed gas pressure medium is Ne. Ne freezes at 4.7 GPa but remains quasihydrostatic until 16 GPa. Alternatively, He can be used. He freezes at 11.8 GPa and remains hydrostatic until >60 GPa.[3]

Soft solids such as MgO, NaCl and CsI can also be used as a pressure medium for harder materials (e.g. ceramics). These medium are simple to load but behave less hydrostatically than liquid or gas media.[126]

Determination of pressure in a diamond anvil cell

Determination of the pressure in diamond anvil cells is typically done using various calibrations. An early method was to use the known phase transformation pressures of various materials as pressure markers. Now, scientists have developed numerous calibration standards such as ruby florescence, measuring the Raman spectrum of the diamond, and placing an internal calibration with a known equation of state in the DAC.[122]

In this work, the main method used is the ruby fluorescence method. This involves placing a ∼5-10 μm ruby inside the cell and measuring its fluorescence using a laser and spectroscope whilst it is under pressure.[128] The shift of the ruby fluorescence lines with pressure is very well known.[129] It should be noted that this method becomes less reliable

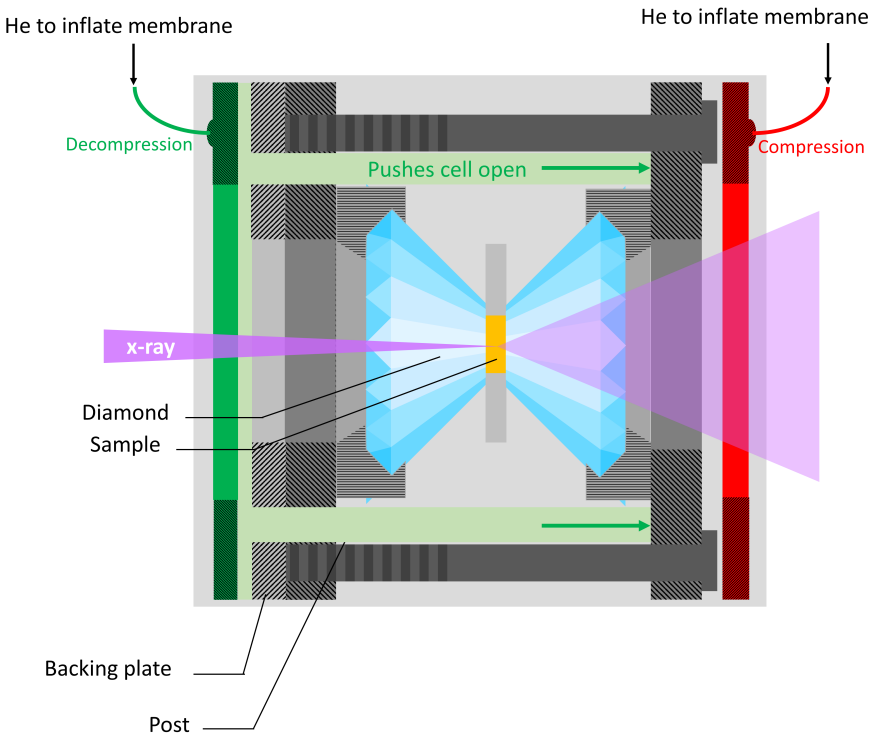

Figure 2.6: A schematic diagram of the double membrane setup used to remotely control the pressure inside a diamond anvil cell.

at very high pressure (∼80 GPa).[129] The pressures used in this thesis were well below this limit.

When using x-rays, it is possible to place a material with a known equation of state into the DAC. Powder diffraction of this material can be collected when it is under high pressure.[3] The XRD peak positions are then compared with the equation of state to determine the pressure inside the cell. Typical materials used in this method are Au, Pt and MnO. These materials are chosen due to their high compressibility (meaning that their d-spacings will shift significantly with pressure) and their stability under pressure. Other considerations for the material include the XRD scattering cross section of the material (if it is too high, it will dominate the XRD signal), peak positions that do not overlap with the sample, and the occurrence of phase transformations. In this work Pt and Au were used. Pt was chosen due to most of its d-spacings not overlapping with any spacings in the different phases of Si and Au was chosen due to it conveniently being present at the top of the nanowires.

Double membrane system for diamond anvil cells

Externally controlling the pressure inside a DAC can be achieved using a membrane system. A membrane is a thin, donut-shaped, metal balloon that can be inflated and deflated in a controlled manner. Examples where externally controlling the pressure is useful include when heating/cooling the DAC, when rapid unloading is required, or to control the decompression rate.

A single membrane system can be used to push the cell closed and thus control compression. Whilst this membrane can be deflated to reduce pressure, completely deflating the membrane will not bring the pressure back to ambient pressure. This problem can be solved by adding a second membrane to the system that pushes the cell open. This is shown in Fig. 2.6. To achieve this, the bottom of the cell is screwed to a plate to hold it in place. Metal bars are then placed into the cell to push the top of the cell.[130] Another plate is placed behind these bars to push them and thus push the DAC open. For this study, the double membrane system was placed in a resistive heating block to allow for remotely controlled compression and decompression at temperatures ranging between 25-165°C.[130]

Even with a double membrane system, it is difficult to have a consistent decompression rate due to the plastic deformation (thinning) of the gasket. This means that the gasket can never reach its original thickness. This leads to the occasional leakage of pressure medium that causes a sudden drop in pressure. In this work, the ruby fluorescence was monitored at intervals ranging for 0.1-5 s depending on the desired decompression rate.

DAC experimental details

All experiments used diamonds with a 400 μm culet size, a stainless steel gasket preindented to 45-60μm with a 180-250 μm diameter hole. Either Ne or 4:1 methanol was used as a pressure medium.

For the majority of ambient temperature experiments, the pressure was controlled by the tightening of the screws, whilst all high temperature and one ambient temperature experiments used the double membrane system to control the pressure.

More specific details of these experiments are provided in each chapter.

2.2 Characterisation techniques

2.2.1 Raman Spectroscopy

The scattering of light by matter can occur by the excitation of a material to a virtual excited state. Relaxation of the excited state produces a scattered photon that may be of the same energy (elastic, Rayleigh) or a different energy (inelastic). Raman scattering is a form of inelastic scattering.[131] These scattering interactions are shown in Fig. 2.7. For Rayleigh scattering, a material is excited to a higher energy state by an incoming photon, and then falls back to its original energy state by emitting a photon at the same energy as the original photon. For Raman scattering, the material gains or loses some energy during the interaction, decaying back to a different energy state and emitting a photon of correspondingly higher or lower energy than the incoming photon. The change in energy ($\Delta E = E_{scattered} – E_{initial}$) between the initial and final energy of the photon is known as the Raman Shift.[131]

If the scattered photon is shifted to a lower frequency, the vibrational mode will be shifted to a higher energy. This is known as Stokes scattering. If the opposite occurs, it is known as anti-Stokes scattering. Anti-stokes is less likely as it requires an already excited state, and most vibrational modes will not be excited at ambient temperature.

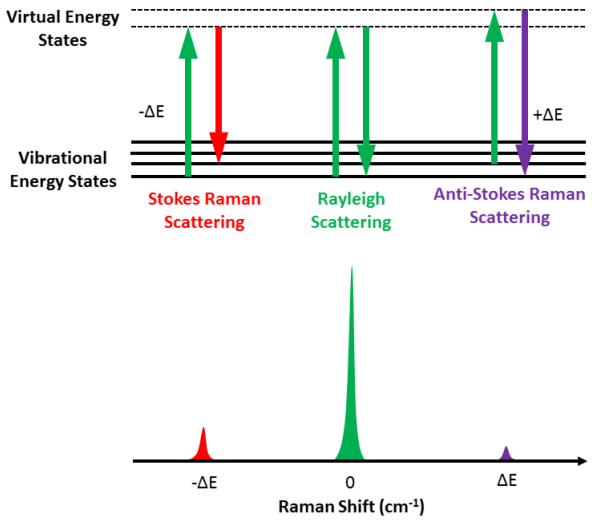

Figure 2.7: Top- a schematic of the excitation process involved in Raman and Rayleigh scattering. Bottom- a sketch of the scattering spectrum involving the scattering processes shown above.

Anti-stokes scattering will increase with temperature as more modes are excited at higher temperatures. Raman spectroscopy is therefore typically performed using the Stokes component of a Raman spectrum.[131] It should be noted that Raman scattering is 5-6 orders of magnitude less than Rayleigh scattering. Raman modes in a material are caused by the interaction between the photon and the vibrational modes of the material. Both structurally and chemically different materials have different phonon modes. Whether a phonon mode is Raman active depends on its anisotropic polarizability when interacting with an oscillating electric field such as a photon. As different materials have different phonon modes, the Raman signal for a material is unique and therefore can be used to identify a material. Figure 2.8 shows typical Stokes Raman spectra of different phases of Si. From this graph, it is clear that different phases of Si have different characteristic Raman spectra. More details can be found in Refs.[131] and[132]. Note that metals are typically not Raman active.

The width of the Raman mode is affected by multiple factors. These include temperature (high temperatures cause peak broadening), instrument parameters (such as the grating and CCD detector used), the exertion of deviatoric stress on a material, and the size of a material (nanocrystallinity causes broadening). The position of a Raman mode can also shift under strain and crystal size. This is due to a change in the lattice parameter causing a change in the phonon energies. The application of high pressure usually shifts phonons to higher energies due to the lattice contracting in size.

Raman setup and experimental details

The majority of the Raman spectroscopy in this work used a Renishaw inVia Reflex confocal Raman system. A schematic of the main components of this system is show in Fig. 2.9. These components are the laser, neutral density filters, a microscope objective, an edge filter, slits, a prism, the diffraction grating and a CCD detector.

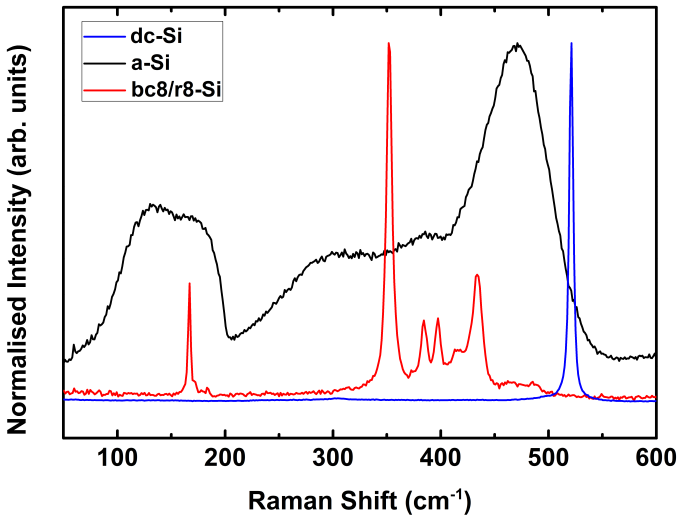

Figure 2.8: Raman spectra of different phases of silicon.

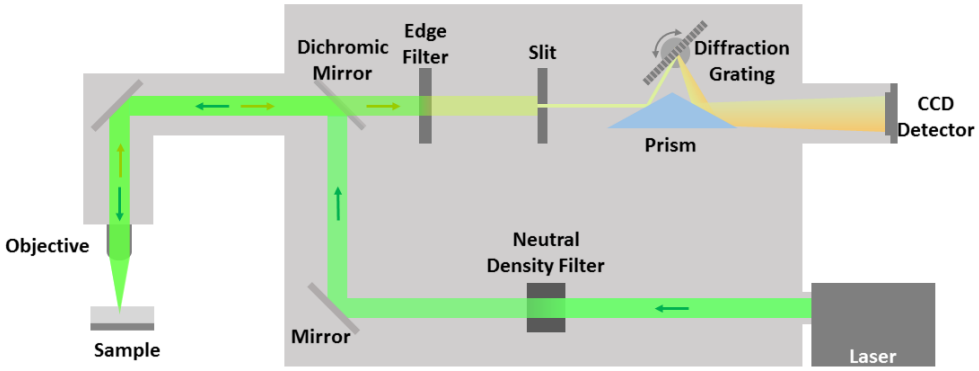

Figure 2.9: A schematic diagram showing the major components of a Renishaw inVia Reflex confocal Raman system.

A laser is used to provide a monochromatic light source. The wavelength of this laser is chosen depending on a number of factors including its penetration depth into a material, avoiding florescence at the region of interest, the spot size the laser can achieve, and any avoiding unwanted interactions (such as absorption) with the sample. The Renishaw Raman system at ANU is equipped with 325, 532, 633 and 785 nm lasers.

Before the laser reaches the sample, it is passed through numerous optical elements. One of the first elements in the laser beam path are neutral density filters. These decrease the laser intensity by a well-defined amount and multiple filters can be used in combination to reduce the laser intensity by different amounts. The power of the laser is chosen based on the capacity of the laser to damage the sample, to reduce fluorescence and to avoid saturation of the detector. Beam steers are mirrors that are used to direct the laser beam down the desired optical path. The beam is then directed to a microscope objective by being reflected off a dichromatic mirror.

The microscope objective is used to focus the laser beam into the sample. The laser then interacts with the sample. The scattered light (which can be a combination of Raman scattering, Rayleigh scattering and fluorescence) is then collected using the same

objective.

The reflected light is then sent through the dichromatic mirror and into a Rayleigh rejection filter. This is required to remove the Rayleigh signal as it is significantly higher than the Raman signal. In this Raman system, an edge filter is used. An edge filter blocks below a particular wavelength. For a Raman system, this wavelength is chosen to be a little bit longer than the laser wavelength such that it blocks the Rayleigh scattered light. It this configuration, only the Stokes Raman scattering is allowed to pass through.

After passing through the Rayleigh rejection filter, the beam passes through a slit. This slit removes light that does not come from the interaction of the laser and the sample. A prism is used to direct the beam to the diffraction grating. The diffraction grating splits the beam into its component wavelengths, directing the light back to the prism. The beam is then directed onto a CCD detector which collects the spectrum.

The resolution of the data is determined by the laser wavelength, the spacing of the grating, and the distance between the diffraction grating and detector. In the Renishaw Raman system, the distance between the detector and grating is fixed and thus only the diffraction grating and laser wavelength can be varied.

The spatial resolution of the Raman system can be improved using a confocal set-up. The Renishaw inVia system achieves this by putting the beam through a narrow slit and reading a small region of the CCD detector, rejecting any signal that did not come from the region that was in focus on the sample. The trade off for this higher resolution is a lower signal (and the need for a more careful alignment).

2.2.2 X-ray Diffraction

X-ray diffraction is a powerful technique used for determining crystal structure of a material. XRD relies on the interference of x-rays as they scatter off planes in the lattice. This causes regions of high and low intensities of x-rays that are characteristic of the spacings between the planes of atoms in a crystal lattice. A crystal lattice can be described by a set of repeating units. A single one of these units is know as the unit cell and it can be described by the the lengths a, b and c, angles α, β and γ and the coordinates of any atoms inside the cell. By determining these spacings and their intensity, the structure of a material can be determined. The diffraction of x-rays off a material can be described using Bragg's law.

Bragg's law is given in equation 2.6 relates the order of the reflection (n), the wavelength of the x-ray beam (λ), the distance between crystallographic planes with miller indices of (hkl) [d_{hkl} (Eqn. 2.7 shows how to calculate this value for an orthorhombic lattice structure)], and the angle of diffraction (θ). It is an empirically derived law and is only an approximation.

$$n\lambda = 2d_{hkl}sin\theta \tag{2.6}$$

$$d_{hkl}^2 = \frac{1}{(h/a)^2 + (k/b)^2 + (l/c)^2} \tag{2.7}$$

Bragg's law does not give any information about the relative intensities of the scattered x-rays from different planes. The intensity of each reflection is determined by how

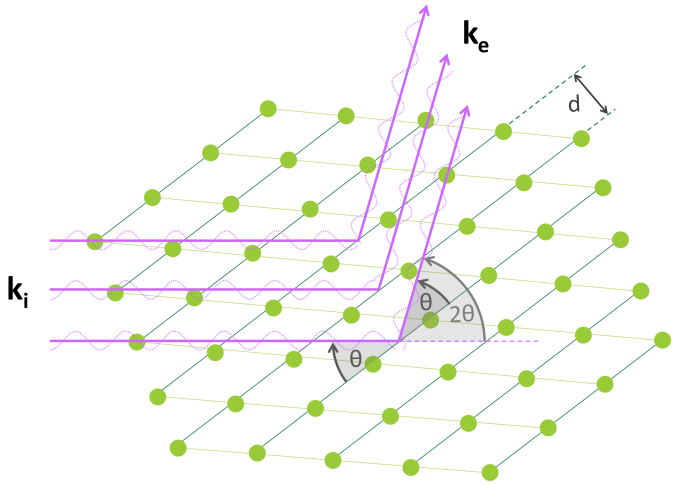

Figure 2.10: The scattering of an x-ray from a lattice.

the reflected x-rays interfere with each other during diffraction as well as the ability for different types of atoms to scatter the x-rays. This can mathematically be calculated using the structure factor ($\mathbf{F_{hkl}}$). This is given by Eqn. 2.8 below:

$$\mathbf{F_{hkl}} = F_{hkl}e^{i\alpha_{hkl}} = \Sigma_j f_j e^{i2\pi(hx_j+ky_j+lz_j)} \tag{2.8}$$

Where f_j is the structure factor for the jth atom in the unit cell (this is equal for atoms of the same species), α_{hkl} is the phase of the diffracted beam, and x_j, y_j and z_j are the coordinates of the jth atom. For some values of (hkl) in some lattices, $\mathbf{F_{hkl}} = 0$. When this is the case, the reflection is considered to be kinematically forbidden.

In reality, XRD peaks have some broadening. Broadening in XRD data can caused by several factors. These include instrument related factors, temperature, thickness of the sample and crystallite size.

In this work, angular dispersive XRD using a synchrotron as a source is used. Angular dispersive XRD uses a fixed wavelength monochromatic source and measures the positions of the diffracted beam.

Experimental details

The XRD measurements in this project were made using the 16ID-B beamline at HPCAT at the Advanced Photon Source in Argonne National Laboratory, USA. This beamline is a dedicated high pressure beamline which uses a high intensity x-ray beam to collect powder diffraction patterns from samples in diamond anvil cells. The source of x-rays for this beamline is an undulator. An undulator is a series of dipole magnets placed in a periodic structure. This causes electrons that pass through it to oscillate and radiate energy. From this process, a bright x-ray source with a narrow energy band is produced. Next the beam is monochromated using a diamond double crystal monochromator which separates the beam into its different energies using Bragg scattering. The beam is then

focused into a small spot (∼3x5μm in this work) using Kirkpatrick-Baez (kb) mirrors. Technical details of this beamline can be found in Ref.[133].

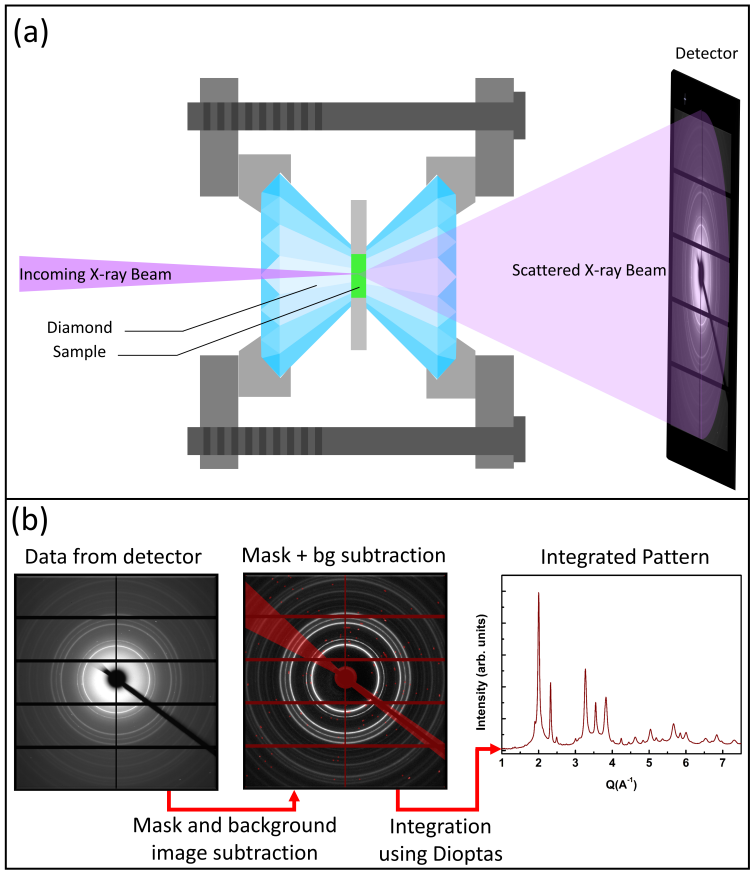

Figure 2.11: (a) The experimental setup of a DAC in a synchrotron powder diffraction beamline. (b) The process of converting the image collected on the detector to a powder diffraction pattern.

The beam is then passed through the sample [see Fig. 2.11 (a)] This can be either through the DAC to measure materials "in-situ" under pressure or the sample can be recovered from the DAC and characterised at ambient pressure. Both of these methods were used in this work. The range of angles that Bragg reflections that can be detected depends on the opening angle of the DAC and the energy of the x-ray beam. After interacting with the sample, the beam then passes through air before hitting a 2D image detector (in this case a Pilatus 1M-F detector). A beam stop is used to prevent the bright undiffracted beam from damaging the detector.

An example of an image from the detector is shown in Fig. 2.11 (b). This image contains powder diffraction rings, and artefacts from impurities, the detector and the beam stop. To convert the image to a 1 dimensional diffraction pattern, radial integration using Dioptas is used.[134] This process involves masking out any unwanted regions and sometimes subtracting a background image and the software (calibrated using a calibration image) to perform the integration. The output is ASCII file that can then be plotted and analysed.

There are several background signals coming from DACs in XRD. These are scattering

of the x-ray beam from the atmosphere, Compton scattering of the diamonds and x-ray scattering of the diamonds. The first two can be subtracted out using an image of the background, whilst the latter tends to cause spots in the diffraction pattern that can be masked out.

2.2.3 Scanning Electron Microscopy

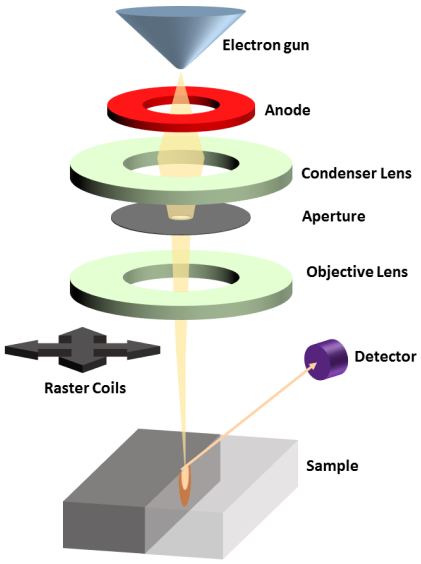

Figure 2.12: A schematic of the basic main components in a scanning electron microscope.

Electron microscopy involves imaging a material using electrons. As electrons have a much shorter wavelength than visual light, electrons are able to resolve much smaller details than light. In scanning electron microscopy, the beam of electrons is rastered across a sample and a detector collects information from each point. Rastering the beam over the same number of points but over a smaller area will result in higher resolution.[135]

The main components of an SEM are an electron gun, a condenser lens, an objective lens, raster coils and a detector. The electron gun is the source of electrons in an SEM. It consists of a filament and a Wehnelt cylinder. The filament, which is either a tungsten filament, LaB_6 crystal or field emission gun, emits the electrons when a current is applied to it. The Wehnelt cylinder is a metal cup with a small hole in it that goes over the filament. The small hole allows for some of the electrons to pass through it creating a beam, whilst the rest of them are conducted away when they hit the cup. An anode attracts electrons in its direction, sending electrons down the beam.[136]

Once a beam of electrons is formed, it is focussed using electromagnetic lenses. The first of these is the condenser lens which controls the spot size of the beam by determining the angle at which the beam converges at. After this the beam is passed through an aperture. The objective lens is used to focus the beam at the sample. Once a probe is formed, the beam is rastered over the sample by raster coils. These raster coils deflect the beam in a controlled manner. Other lenses (not shown) are used to correction for distortions in the lenses, known as astigmatism.[135]

When the beam is at the sample, it interacts with the sample in numerous ways producing radiation such as secondary electrons, back scattered electrons, and x-rays. Secondary electrons are most commonly used for imaging, and generated from the collision of the electron beam and the electrons in the sample. These electrons are low energy meaning that only the secondary electrons created near the surface of the material can escape from the sample.[135]

Once the beam has interacted with the sample, a detector can be used to collect the electrons/x-rays. The most common detector is an Everhart-Thornley detector. This detector has a bias applied to it that can either attract secondary electrons (positive bias), or repel secondary electrons (negative bias) allowing higher energy backscattered electrons only to hit the detector.[135]

2.2.4 Transmission Electron Microscopy

Transmission electron microscopy involves passing high energy (typically 60-300 kV) electrons through a very thin (<300 nm) sample and imaging the transmitted electrons. Like in SEM, the electrons will interact in the sample in many ways, producing different sorts of radiation (secondary electrons, back scattered electrons, Auger electrons, x-rays, elastically scattered electrons, inelastically scattered electrons and an unscattered electron beam). Whilst all these interactions are relevant in TEM, only the electrons which are transmitted through the sample will be considered in this section.[136]

There are two main ways in which electrons can be collected in TEM. Below the sample, the scattering pattern may be imaged. This pattern is dominated by diffraction and is therefore called a diffraction pattern. Alternatively, a change in the lens settings allows for an image to be created from the transmitted electrons. As discussed below, the contrast in the image is the product of mass thickness contrast, diffraction contrast and phase contrast.[136]

Typical set-up of a transmission electron microscope

A schematic of the basic layout of a TEM is shown in Fig. 2.13. Like in an SEM, the first component of a TEM is the electron gun. The electron gun works in the same way as an electron gun in a SEM except that electrons are typically accelerated to significantly higher voltages.[136]

Once a beam is formed, it passes through the condenser lens system, which here is shown to consist of two condenser lenses. These lenses adjust the size of the beam, and the convergence angle of the beam on the sample. The electrons then pass through the condenser aperture. This both reduces the intensity of the beam and reduces spherical aberration.[136]

The beam is then passed through the specimen before a series of electromagnetic lenses and apertures are used to control the imaging conditions. The first of these is the objective lens which focusses the parallel beam passing through the sample.[136]

An objective aperture can be placed on a plane where diffraction is in focus. This allows only the central beam or diffracted beams that are within the area of the aperture to pass through. This makes it such that the image is only composed from the central

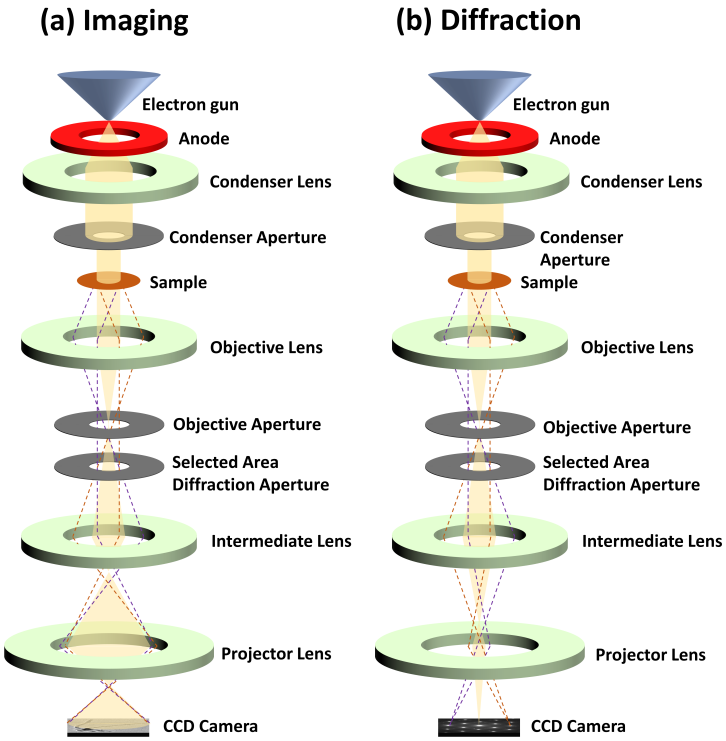

Figure 2.13: A schematic of the layout of a transmission electron microscope in (a) imaging made, (b) diffraction mode.

beam and/or the diffracted spots. This aperture is critical for both bright field and dark field imaging - details of this will be given later on.[136]

On the plane at which the image is in focus, a selected area aperture can be placed. This is used to only allow electrons that come from a particular part of a sample to pass through. This aperture can be used to selectively collect a diffraction pattern from a particular area of the sample.[136]

The intermediate lens is used to select for either imaging or diffraction mode by moving the focus of the beam. The magnification of the image/diffraction pattern is adjusted using the projector lens. A CCD camera is used to collect the image.[136]

Diffraction

Like x-rays, electrons have a wave nature and therefore diffraction is a possible interaction. The underlying physics in electron diffraction is similar to XRD, however differences occur such as effects from thickness of the sample.[136]

In a TEM, one can change between imaging and diffraction by applying the the correct current into the intermediate lens. This is shown in a ray diagram in Fig. 2.13 (c). Like in XRD, electron diffraction can be used to gain structural information about a sample, in particular the region of the sample selected by the selected area aperture.[136]

Like in XRD, the angle at which the sample is oriented will affect the diffraction pattern shown. In a TEM the sample can be tilted to change the diffraction spots recorded.[136]

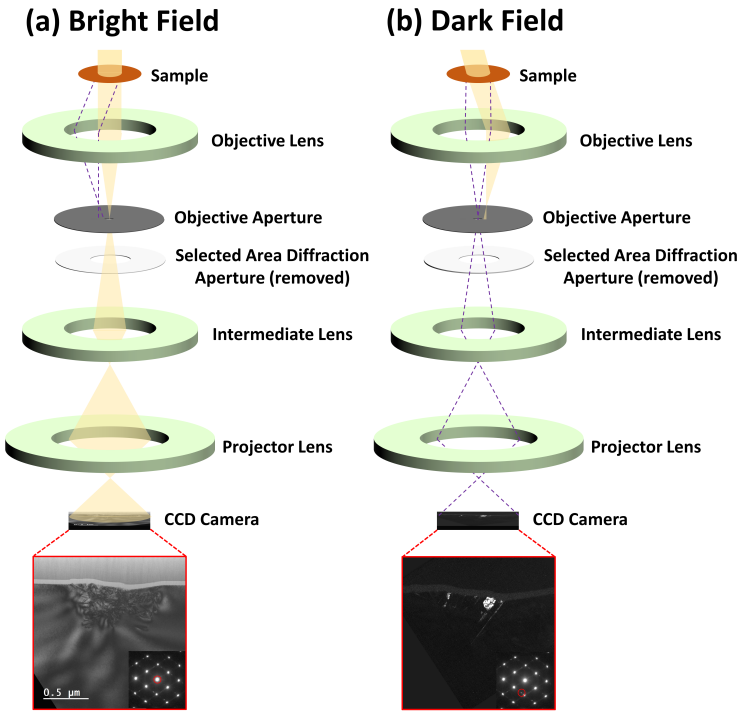

Figure 2.14: A schematic of the layout of (a) bright field imaging, and (b) dark field imaging. Below each schematic is an example image under each condition which has an inset diffraction pattern that shows the position of the objective aperture used.

Imaging

There are several factors than can cause contrast in a TEM image. These include sample mass-thickness contrast, bend/diffraction contrast and phase contrast.[136]

Mass-thickness contrast is due to a specimen allowing different intensities of the beam to pass through due to a difference in the atomic mass of a specimen or changes in the thickness of a specimen. Regions with different atomic masses will scatter differently, whilst thicker regions will scatter more electrons, resulting in less transmitted electrons.[136]

Diffraction contrast is due to variations in the diffraction conditions, such as two crystal grains being next to each other, in a sample. Bend contrast is a special subset of diffraction contrast that occurs due to a sample being bent. When the sample is tilted, the diffraction conditions change, changing the diffraction contrast.[136]

Phase contrast arises from two or more beams (transmitted or diffracted) interfering with each other due to their different phases. Examples where contrast arises due to phase contrast include thickness fringes and columns of atoms [this being the most important effect in high resolution TEM].[136]

The simplest method of imaging is taking an image where no objective aperture is used. These images tend to lack contrast as the image is composed from both the transmitted and diffracted beam.[136]

Bright field (BF) imaging is shown schematically in Fig. 2.14 (a). Here the objective aperture is placed over the central beam (and sometimes some of the diffracted beam)

such that the resulting image is composed only or mostly of the electrons that did not diffract.[136]

Dark field (DF) imaging makes use of the objective aperture to reject all electrons except for those diffracted under specific conditions. This could mean that the image is made up from the diffraction of a particular spot, multiple spots or part of an amorphous ring. DF imaging reveals the region(s) of a sample where the chosen diffraction condition comes from. It is thus useful for highlighting regions such as a phase transformed region in an indent or a particular orientation of crystal. There are two methods of making a DF image; moving the objective aperture over a diffracted spot, or tilting the beam such that the diffraction spot of interest passes directly down the column. The second method is shown in Fig. 2.14 (b).[136]

Focused ion beam milling

For TEM examination of the material underneath a nanoindentation residual impression, sample preparation by focused ion beam (FIB) milling was used. A FIB is an instrument that uses a similar configuration of lenses to an SEM to focus a beam of gallium ions onto a sample. These beam of ions can be rastered across a sample allowing for material to be precisely removed.[137] These days the majority of FIBs also contain an electron beam (or SEM) which can be used for nondestructive imaging of the sample. An FEI Helios 600 NanoLab was used for all FIB work.

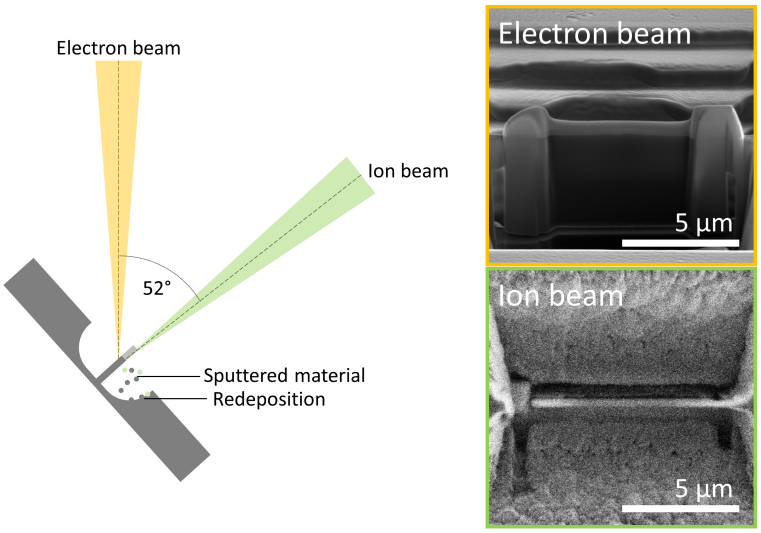

Figure 2.15: The general set up of a focused ion beam with an example of an electron and ion beam image taken at the same tilt.

The FEI Helios 600 NanoLab is a dual beam FIB containing a electron beam directly about the sample and a gallium ion beam at an angle of 52° from the electron beam [Fig. 2.15]. Imaging can be performed with either the electron or ion beam. Imaging with the ion beam is done by either imaging the secondary ions sputtered from the sample or secondary electrons that have been knocked out of their atoms with the ion beam.

When preparing samples using the focused ion beam, there are a number effects that

need to be considered. These include redeposition, ion beam damage (including amorphisation), dynamic annealing and uneven milling such as curtaining.

All the samples prepared for TEM using the FIB were made using the ex-situ lift-out technique.[138] The first step of this process is to protect the surface of the region of interest from ion beam damage. This is done by depositing a ∼200 nm thick layer of Pt using the electron beam. The ion beam is then used to deposit ∼1-1.5 μm on top of the electron beam deposition to further protect the surface. After the Pt is deposited, the ion beam is used to dig a trench on either side of the region of interest. The sample is approximately 1 μm thick at this stage. This is known as a "rough mill". Next, the lamella is cut along the bottom and part of the sides of the sample such that is it still attached in a process called a "J-cut" or a "U-cut". The sample is then further thinned at a grazing angle with decreasing voltage and current ("final thinning") until it is electron transparent by alternate milling on each side. Once thin enough, the lamella is cut free from the sample. The sample is then removed from the FIB and a micromanipulator with a glass needle is used to transfer the lamella onto a carbon coated formvar TEM grid.

Rough milling was typically performed at 30 kV whilst final thinning was performed with a combination of 30, 16, 5 and/or 2 kV, depending on the sample. Note that the lowest voltage was always used last due to a lower penetration depth of the ions, and therefore a thinner damage layer.

Preparation of recovered nanowires

After the nanowires were compressed in a DAC, they were removed from the gasket using a stainless steel needle and placed in a small container containing ∼0.5 mL of either ethanol or isopropanol. The samples were then ultrasonicated for 5 min. A syringe or micropipette was used to transfer the nanowires in solution onto a 200 mesh holey or lacey carbon copper, where the solvent would evaporate, leaving the NWs on the gird.

2.3 Summary

The methods for applying high pressure and the techniques used to characterise the samples *in situ* and after pressure application have been outlined in this chapter and summarised in Fig. 2.16. Nanoindentation and diamond anvils cells were used to apply higher pressure. Nanoindentation involves pressing a sharp diamond tip into a material and continuously monitoring the force applied and the distance penetrated by the tip. This can be performed at both high and low temperatures. DACs involves compressing a material, that is held in place by a gasket, between two diamonds. The pressure is monitored using an internal calibrant.

After the samples were subjected to high pressure, they were characterised by several techniques; Raman spectroscopy, x-ray diffraction, scanning electron microscopy and transmission electron microscopy. Raman spectroscopy involves illuminating a sample using a laser and collecting the inelastically scattered light. The resulting spectrum is characteristic of a material and thus can be used to identify the material. X-ray diffraction uses x-rays to identify a crystal structure based on the positions and intensities of the peaks in the resulting diffraction pattern. Scanning electron microscopy rasters a probe of

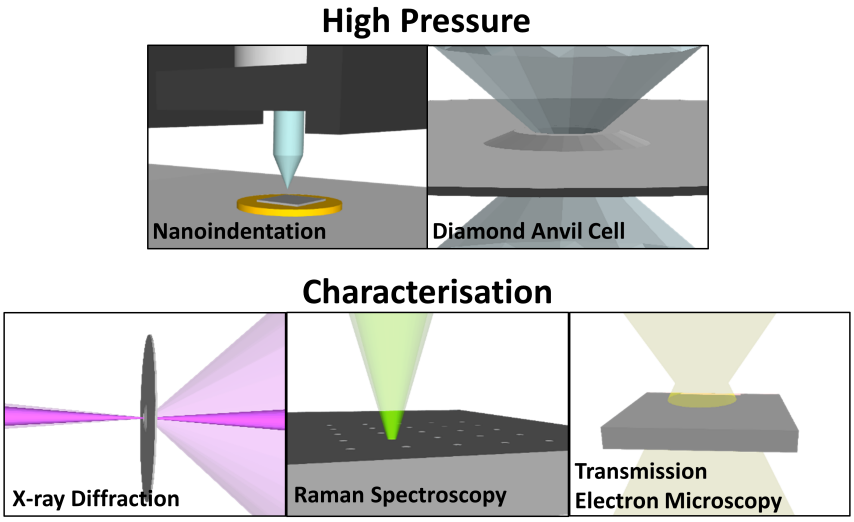

Figure 2.16: Summary of the techniques used to apply high pressure and characterise samples during and after high pressure application.

electrons over a material in order to create a high resolution image of the sample. This was used to understand the morphology of samples after pressure was applied. Transmission electron microscopy involves passing a beam of electrons through an electron transparent material. This was used to gain information about the structure and morphology of both indents and Si nanowires.

Chapter 3

The influence of size on the phase transformation of silicon

In the introduction of this thesis, it was highlighted that the size affects the high pressure phase transformation pathways of Si. Whilst very small and near-bulk material has been studied, the behaviour of Si of intermediate sizes is not known. In this chapter two intermediate sizes of SiNWs will be investigated to further understand the effect of size on the phase transformation behaviour of Si.

3.1 Introduction

As mentioned in Chapter 1, the high pressure phase transformation behaviour of nanoscale Si is not well understood with only limited, and even contradictory studies reported.[94,109,110,139] Only two of these studies reported the behaviour of SiNWs during decompression, one involving 10-50 nm Si nanoparticles and the other using SiNWs. The first study (on 10-50 nm Si nanoparticles) reported β-Sn-Si to exist down to much lower pressures than bulk-Si before phase transformation to a-Si at $\sim$5 GPa.[94] The second study reported that SiNWs with diameters up to 700 nm phase transformed similarly to bulk-Si.[110] As these studies investigated very small material or close to bulk-Si, it would be useful to understand the behaviour in intermediate size ranges.

An additional motivation for this work is to attempt to combine the novel properties of phase pure bc8, r8-Si and possibly hd-Si with the particular geometry of nanowires. This is because nanowires are promising candidates for future electronic and optoelectronic devices. For example, this could result in the creation of SiNWs with strong absorption in the solar region of the spectrum. Si nanoparticles with the bc8-Si phase have also been predicted to be used for solar energy conversion above the Shockly-Queisser limit,[63] and this properly might also be prevalent in SiNWs.

In this chapter, SiNWs of two size ranges (80-150 nm and 200-250 nm) are compressed up to $\sim$22 GPa. Raman spectroscopy and XRD were used to determine the structure of the SiNWs under pressure. SEM and TEM were then performed after high pressure treatment to look at the structure and morphology of the recovered SiNWs.

3.2 Experimental details

This section outlines the specific experimental details for this chapter.

Preparation of the SiNWs

The 80-150 nm SiNWs were grown by A/Prof Alois Lugstein (TU Wien, Austria). Vapor liquid solid growth in a hot wall CVD reactor was used to synthesize the 80-150 nm diameter SiNWs.[140] Before growth, the native oxide layer on the (111) Si substrate was removed using hydrofluoric acid and a 2 nm thick gold layer was deposited via thermal evaporation. This layer was used as a catalyst for growth. The SiNWs were grown with diluted silane gas as a precursor at a pressure of 3 mbar. The growth was done at 500°C at a total pressure of 3 mbar using a 100 sccm flow of silane (2% in a He mixture) and with 10 sccm hydrogen. Once the desired growth was achieved, the silane was switched off and the sample cooled in vacuum. The top down approach of common electron beam lithography and then reactive ion etching was used to fabricate the 200-250 nm SiNWs. These SiNWs were 1.8 μm in height. Figure 3.1 shows images of the SiNWs after fabrication for (a) the 80-150 nm SiNWs, and (b) the 200-250 nm SiNWs. These SiNWs were fabricated by A/Prof Alois Lugstein from TU Wien, Austria and Dr Manfred Reiche from the Max Planck Institute of Microstructure Physics, Halle, Germany, respectively.

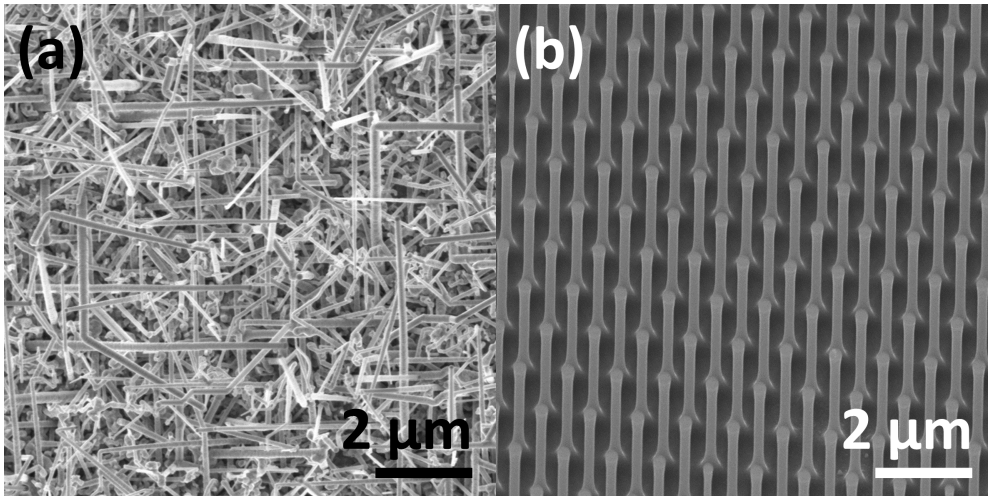

Figure 3.1: SEM images of the SiNWs after fabrication: (a) 80-150 nm diameter SiNWs, (b)200-250 nm diameter SiNWs [Image courtesy of A/Prof Alois Lugstein (TU Wien)].

Diamond anvil cell preparation for SiNWs

Before loading into a DAC, removal of the SiNWs from their substrate was required. Two different techniques were used to remove the SiNWs. The first of these involved ultrasonicating the SiNWs in a mixture of 4:1 methanol:ethanol and allowing time for the SiNWs to agglomerate. Whilst this method worked, it did not yield a high number of SiNWs and therefore a second method was used. This involved using a stainless steel razor blade to carefully 'shave' some SiNWs off the substrate.

After removal from their substrate, the SiNWs were transferred into a DAC using a stainless steel needle. The DAC used had a 400 μm culet size on each diamond. A stainless steel gasket that was preindented to a thickness of 40-60 μm with a 200 μm diameter hole in the centre was used to contain the sample. A small ruby ball was also included in the cell to allow for the measurement of pressure.[129]

A pressure medium was used to both apply a quasihydrostactic pressure and prevent the SiNWs from being pushed together and agglomerating. Two different pressure mediums were used, depending on what was available at the time of loading. A mixture of 4:1 methanol/ethanol was used for the 80-150 nm samples that were characterized with Raman spectroscopy and Ne was used for the 80-150 nm sample characterised using XRD and the 200-250 nm sample where Raman was used.

In-situ measurements and further characterisation

The samples were compressed up to 22 GPa and monitored *in-situ* using Raman Spectroscopy or XRD. Raman spectroscopy was performed using a backscattered geometry through the diamonds on a Renishaw inVia Reflex Raman system using a 532 nm laser, 2400 l/mm grating, $\sim$2.6 μm spot size and $\sim$2 mW intensity. XRD was performed on the 16-ID-B beamline at the Advanced Photon Source at Argonne National Lab. The energy of the x-ray beam was 30 keV and it was detected using a Pilatus 1M-F detector. The resultant powder diffraction patterns were integrated using the Dioptas software package.[134]

After high pressure treatment of the SiNWs, SEM using a FEI Verios SEM operating at 2 kV, 13 pA was performed. The SiNWs were then picked up using a stainless steel needle, ultrasonicated in $<$1 ml of isopropanol and deposited on a holey carbon grid with a syringe. An FEI CM300 TEM operating at 300 kV was used to perform TEM on the SiNWs.

3.3 The phase transformations of 80-150 nm silicon nanowires

Figure 3.2 shows the behaviour of 80-150 nm SiNWs compressed up to 22 GPa and 17 GPa as measured by (a) Raman spectroscopy and (b) XRD, respectively. The Raman data will first be discussed. At 1 GPa, there is a clear dc-Si peak, indicated by a blue star, at 523 cm^{-1} [Fig. 3.2 (a)]. As pressure is increased, this peak shifts towards higher wavenumbers. At 14 GPa this peak is still present and no additional peaks are observed (note that the broad peak, marked by a star, at $\sim$230 cm^{-1} is the dc-Si 2TA mode[141]) indicating that no phase transformation has occurred. Two additional peaks at $\sim$115 and $\sim$397 cm^{-1} indicated by grey triangles are observed at 15 GPa. This indicates that a metallic phase, either β-Sn-Si or Imma Si has started to form. The intensity of the dc-Si peak continues to decrease until 20 GPa at which point it has completely disappeared. At this pressure, only the background signal was observed. This is most likely due to the SiNWs changing completely to sh-Si, a phase of Si that is not Raman active.[142]

The XRD results in Fig. 3.2 (b) will now be discussed. As expected from the Raman

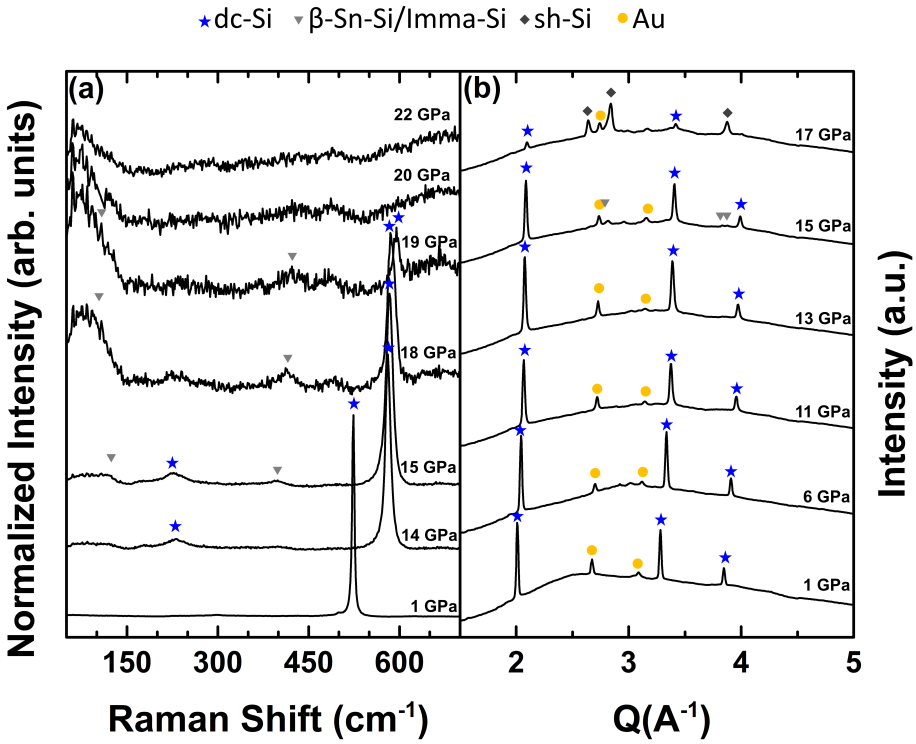

Figure 3.2: The phases present at different pressure for 80-150 nm SiNWs on compression as observed by (a) Raman spectroscopy, (b) X-ray diffraction. Note that sh-Si is not Raman active and therefore is only observed in the XRD data.

results, the SiNWs are initially dc-Si, but additional peaks, indicated by yellow circles are also present. These peaks correspond to the Au found at the top of the SiNWs. This Au is not observed in Raman spectroscopy as metals tend to have no active Raman modes or low Raman signals. Consistent with the Raman data, the SiNWs remain dc-Si until 13 GPa. At 15 GPa, additional peaks, indicated by grey triangles, appear. These peaks could be one of two phases, β-Sn-Si or Imma-Si, however, due to the low intensity of the peaks and the similarity of the XRD patterns of these phases.[17,31] At 17 GPa, these peaks are no longer observed and new peaks corresponding to sh-Si, indicated by grey diamonds, are present. The intensities of the dc-Si peaks have also significantly dropped, indicating that the SiNWs are mostly sh-Si with trace dc-Si at this pressure.

The behaviour of the 80-150 nm SiNWs during decompression is shown in Fig. 3.3. Raman spectroscopy results [Fig. 3.3 (a)] contain only background signal at 22 GPa. When the pressure is decreased to 13 GPa, two weak Raman peaks, indicated by grey triangles are observed. These peaks correspond to either β-Sn-Si or Imma-Si and increase in intensity at 13 GPa. At 6.3 GPa, these peaks are still present but are shifted in wavenumber. Interestingly, phase transformation to r8-Si would already have occurred at this pressure in bulk-Si. At 4.6 GPa, the β-Sn-Si or Imma-Si peaks disappeared and an a-Si signal (red squares) is observed. This indicated that the final phase transformation in SiNWs is to a-Si between 6.3 and 4.6 GPa. Note that a-Si is still observed at 1.6 GPa.

Results taken using XRD during decompression are shown in Fig. 3.3 (b). Firstly, it

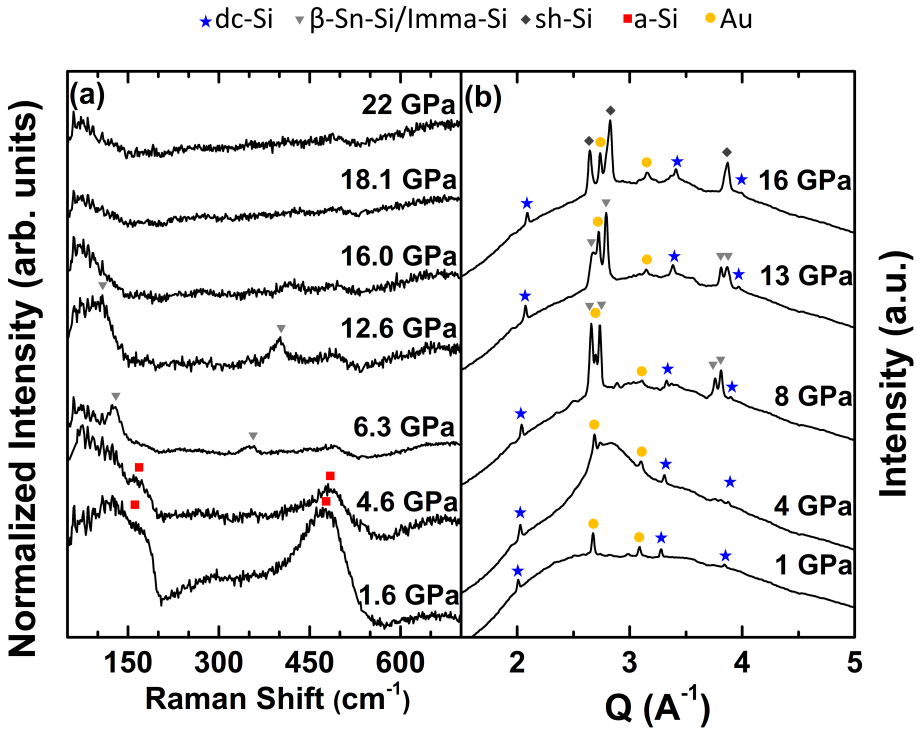

Figure 3.3: The phases present at different pressure for 80-150 nm SiNWs on decompression as observed by (a) Raman spectroscopy, (b) X-ray diffraction.

should be noted that the height of the dc-Si peaks did not noticeably change in intensity during decompression. This suggests that no phase transformation to dc-Si appears to occur during decompression. At 16 GPa, sh-Si is present. This phase transforms to β-Sn-Si between 16 GPa and 13 GPa. This phase is observed down to 8 GPa before it disappears at 4 GPa. This could be due to the formation of a-Si which has a very weak XRD signal which would be significantly less intense than the background signal.

3.4 Investigation of slow decompression rates

In both experiments described in the previous section, decompression occurred in somewhat large increments of 1-4 GPa. In nanoindentation, it is known that rapid decompression leads to the amorphisation, and slow decompression leads to the formation of the crystalline r8/bc8-Si phases.[76] This section, uses the nanoindentation results for inspiration to investigate whether decreasing the decompression rate can allow crystalline phases to form.

Figure 3.4 shows Raman spectra at pressures between 5.7 GPa and 3.4 GPa taken when decompressing β-Sn-SiNWs in ~0.2 GPa increments over several days. At 5.7 GPa and 5.4 GPa, only β-Sn-Si is observed. When the pressure is decreased to 5.3 GPa, additional peaks, marked by green stars, are observed. These peaks correspond to r8-Si.[143] At this pressure, some β-Sn-Si is still present, however lowering the pressure slightly to 4.9 GPa causes this remaining β-Sn-Si to become amorphous. Hence, it is clear that very slow

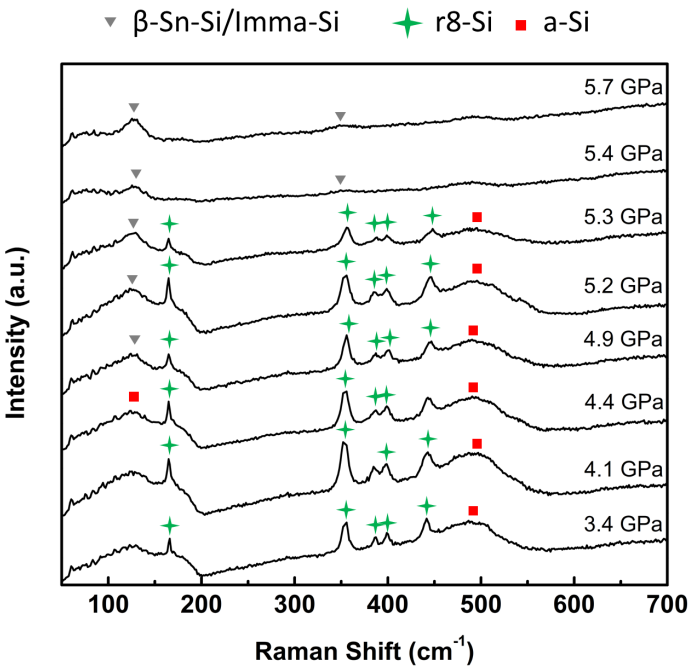

Figure 3.4: A sample of the Raman spectra of 80-150 nm SiNWs taken when decompressing very slowly in ∼0.2 GPa increments over several days. The SiNWs were compressed to a maximum of ∼22 GPa, then lowered to ∼9 GPa and decompressed in small 0.1-0.2 GPa increments.

decompression can be used to allow r8-Si to nucleate in some of the SiNW material. This is in contrast to the SiNWs in the previous section where r8-Si was not observed.

3.5 The phase transformations of 200-250 nm Si nanowires

This section examines the high pressure behaviour of slightly larger 200-250 nm diameter SiNWs. Figure 3.5 shows Raman spectra of 200-250 nm SiNWs during (a) compression and (b) decompression. Like the smaller 80-150 nm SiNWs, the 200-250 nm SiNWs start off in the dc-Si phase, marked by blue stars. This phases is the only phase present until 13 GPa. At 14 GPa, two small and broad peaks (marked by grey triangles) are observed [Fig. 3.5 (a)]. These peaks increase in intensity and the dc-Si peak decreases in intensity until 17 GPa, when the dc-Si peak disappears. This is indicative of a phase transformation from dc-Si to β-Sn/Imma-Si. Between 17 GPa and 20 GPa, the β-Sn/Imma-Si peaks disappeared, indicating sh-Si had formed.

On decompression [Fig. 3.5 (b)] β-Sn-Si forms at ∼16 GPa. The SiNWs remain entirely β-Sn-Si until between 9.2 GPa and 7.9 GPa.[26] Between these pressures, some additional Raman peaks, marked with green stars, that correspond to r8-Si, appear whilst some β-Sn-Si remains.[143] This β-Sn-Si slowly phase transforms to r8-Si until 5.4 GPa. At this pressure, any remaining β-Sn-Si phase transforms to a-Si; two broad peaks indicated by red squares. This indicates that the 200-250 nm SiNWs after decompression are a

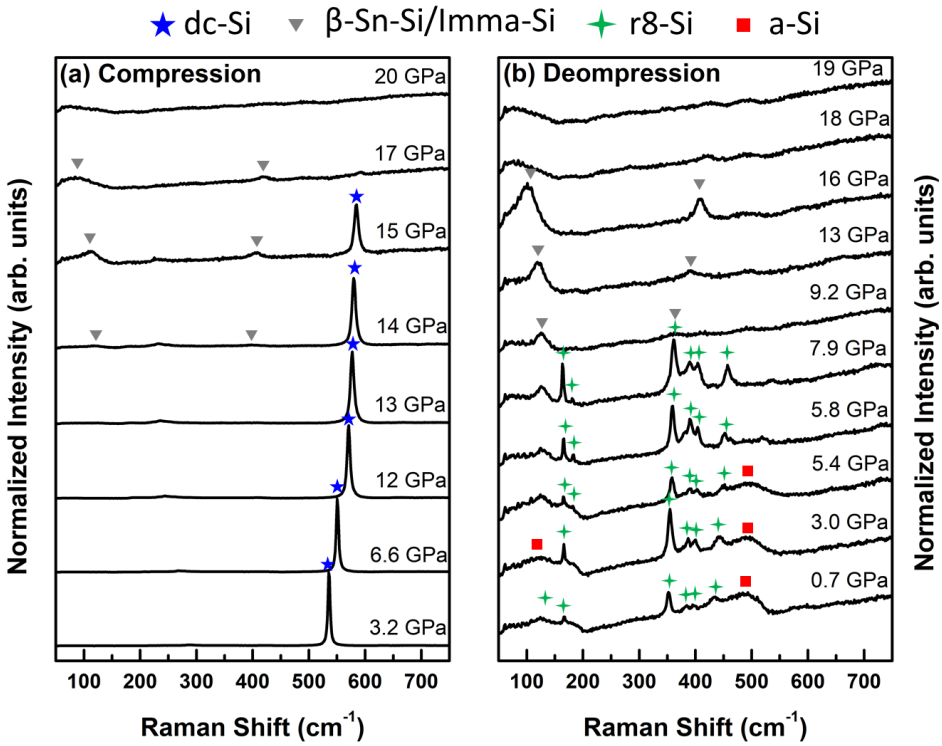

Figure 3.5: *In-situ* Raman spectra of 200-250 nm diameter SiNWs during (a) compression, (b) decompression.

mixture of a-Si and r8-Si.

3.6 Morphology after decompression

As the SiNWs were placed under high pressure, it is important to look at the structural integrity of individual SiNWs and the distribution of phases found in the SiNWs. This section presents some SEM and TEM data on the SiNWs after high pressure treatment.

Figure 3.6 (a) is an SEM of 80-100 nm SiNWs in a gasket (not shown) after removal from the DAC. Here a cluster of randomly oriented SiNWs is observed. Many of these SiNWs are straight and are to ∼5 μm in length. It is quite clear from this image that the SiNWs maintain their nanowire geometry and do not merge together during high pressure treatment.

The TEM results are shown in Fig. 3.6. The 80-150 nm SiNWs will be discussed first. Figure 3.6 (b) shows a bright field image of a SiNW that was compressed to 22 GPa. The inset is a selected area diffraction pattern (SADP) taken from this SiNW. This SADP clearly corresponds to a-Si, as indicated by the diffuse rings present in the SADP. A dark field image of a 80-150 nm SiNW that was compressed to 22 GPa and decompressed slowly is shown in Fig. 3.6 (c). The dark field image is formed from the encircled spot in the inset SADP. This SADP contains a-Si diffuse rings as well as spots that can be indexed to bc8-Si, indicating that this SiNW contains some bc8-Si and a-Si. From the dark field image, it is clear that the bc8-Si is made up of crystallites of ∼20-60 nm in size, and

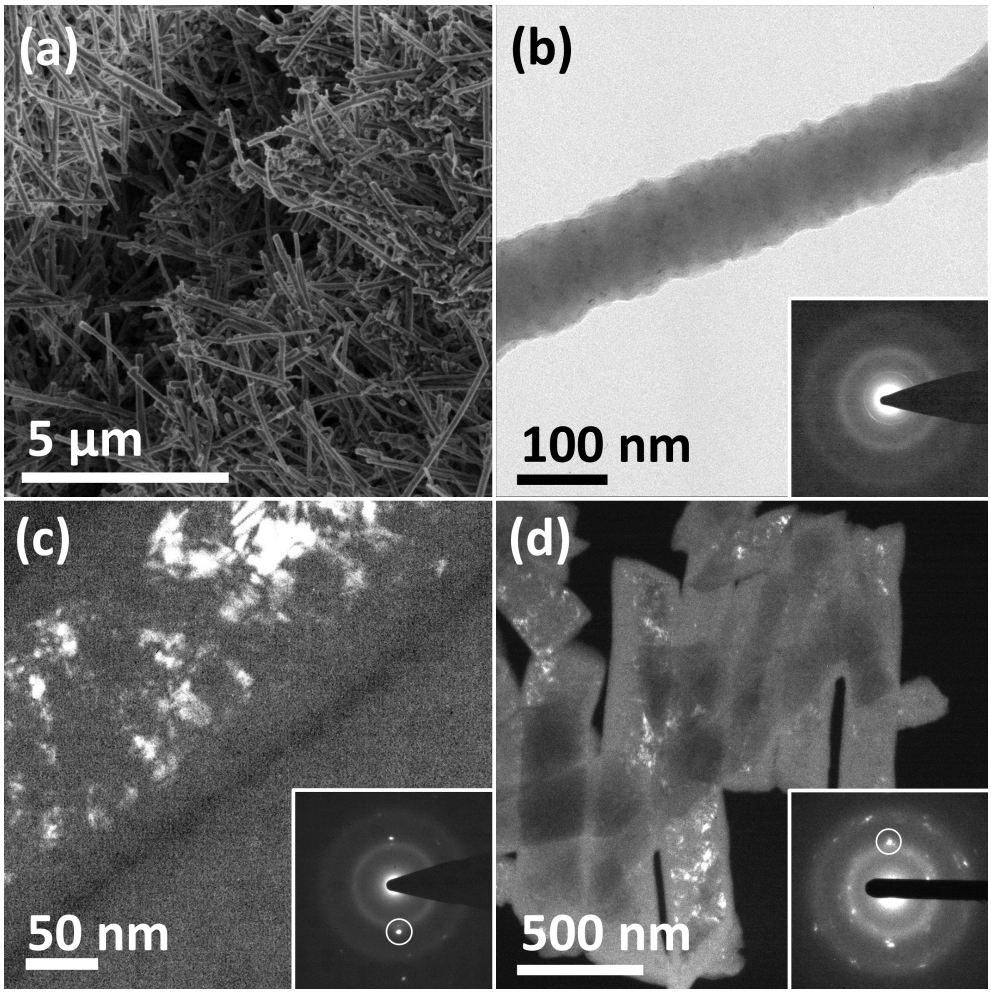

Figure 3.6: (a) A SEM image of 80-150 nm diameter SiNWs after compression, (b) a BF TEM image a SiNW from the 80-180 nm diameter range compressed to 22 GPa with an inset SADP from the SiNW (note that the first inner ring of this SADP is an artefact which occurs when the selected area aperture overlaps both the sample and empty space.), (c) SiNWs from the 80-180 nm diameter range compressed to 22 GPa and decompressed slowly, (d)A DF image of 200-250 nm diameter SiNWs [Image and SADP in (d) courtesy of Dr David Cullen (ORNL)].

hence this NW is polycrystalline.[i] Finally, a DF image of the larger 200-250 nm diameter SiNWs with an inset SADP is shown in Fig. 3.6. Similar to the previous SADP, these SiNWs are either entirely a-Si or a mixture of a-Si and bc8-Si. No entirely bc8-SiNW was observed in this 200-250 nm size range.

3.7 Discussion and comparison to literature

The phase transformation behaviour in both diameter ranges of SiNWs, and the bulk-Si as well as 10-50 nm Si nanoparticles from the literature[6,26,94] are summarised in Fig. 3.7. The phases present during compression are shown on the left and on the right for decompression. Regions with horizontal lines indicate that multiple phases coexist at the given pressure. During compression, both the onset and the completion of phase transformation from dc-Si to metallic Si phases such as β-Sn-Si and sh-Si in the SiNWs (particularly the smaller 80-150 nm diameter ones) is significantly higher than in bulk-Si. Unsurprisingly, this phase transformation for the 10-50 nm Si nanoparticles occurs at even higher pressures, completely bypassing the β-Sn-Si phase and smaller SiNWs were reported not to phase transform up to 15.6 GPa.[139,144] In contrast, other results from the literature reported a lower or similar phase transformation pressure than bulk-Si.[109,110] One of these studies used a large size distribution (50-700 nm diameter) and therefore the results could have been biased towards bulk-Si.[110] The other study[109] might have had a lower onset for phase transformation due to the method of loading the SiNWs into the DAC causing them to agglomerate, or alternatively, a large non-hydrostatic component was present which is known to lower the phase transformation pressure in bulk-Si.[26]

During decompression, the first phase transformation to occur is sh-Si to β-Sn/Imma-Si. This phase transformation appears to occur at a similar pressure to both bulk-Si, the SiNWs studied and the 10-50 nm Si nanoparticles. In the SiNWs β-Sn-Si was observed to exist down to much lower pressures than bulk-Si. In both size ranges of the SiNWs, this phase was observed to occur in at least some of the SiNWs at pressures as low as $\sim$5 GPa. This was consistent with the behaviour of Si nanoparticles.[94] Note that r8-Si was observed to form in some of the 200-250 nm SiNWs and 80-150 nm SiNWs during slow decompression. However, this phase transformation occurred at lower pressure than in bulk-Si. When r8-Si did not form, like the Si nanoparticles, any remaining β-Sn-Si in the SiNWs phase transformed to a-Si at $\sim$5 GPa.

From this work and the few previous studies, it can be deduced that the high pressure phase transformation behaviour of Si depends on particle/SiNW size. Large SiNWs of approximately 600-700 nm in size have very similar phase transformation behaviour to bulk Si. On the other hand, small Si particles/SiNWs were found to have an elevated dc-Si to metallic phase transformation on compression and a depressed phase transformation from β-Sn-Si on decompression. The dominant end phase for Si below $\sim$200 nm in size was a-Si, and r8-Si could occasionally form in the larger sizes or with very slow decompression.

It is quite clear that the phase transformations of SiNWs and nanoparticles differ significantly from bulk-Si and that these difference are due to the size of the SiNWs. This

[i] Note that the $\sim$25 nm region at the edge of this SiNW does not contain any bc8-Si crystallites. This feature will be discussed further in Chapter 5.

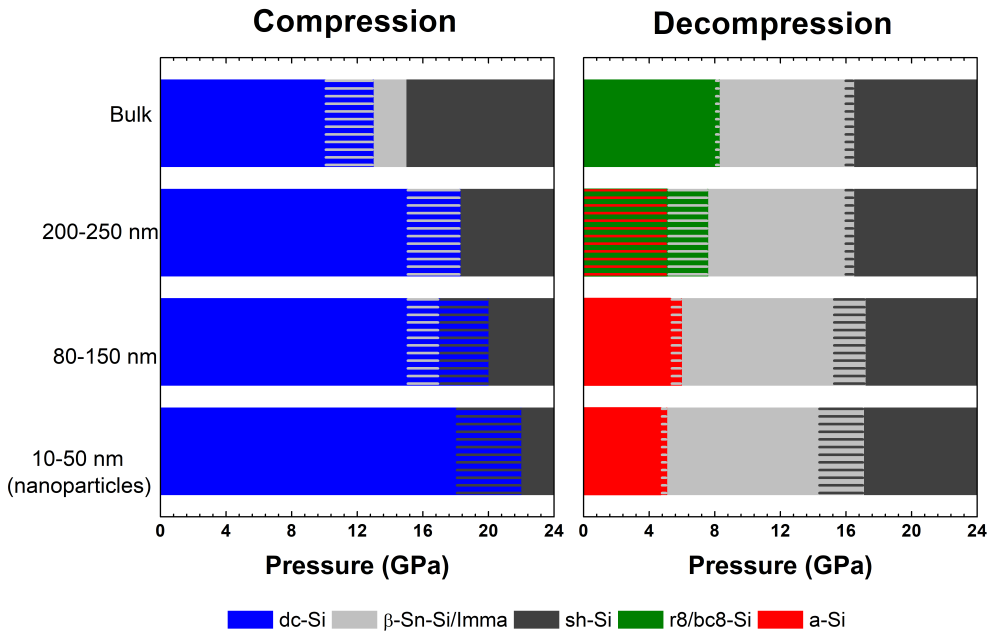

Figure 3.7: A summary of the phases present at the indicated pressures for both compression and decompression of both diameter ranges of SiNWs studied, and bulk-Si and 10-50 nm Si nanoparticles from the literature.[6,26,94]

section examines the phase transformations involved individually to explain some of the observations.

The dc-Si to metallic phase transformation will be discussed first. It is suggested that the elevated phase transition pressure observed for this phase transformation is due to difficultly in nucleating the β-Sn-Si phase. This phase is already difficult in bulk-Si, even being described as "sluggish".[65] The dc-Si to β-Sn-Si phase transformation involves a $\sim$20% decrease in volume and is considered a reconstructive phase transformation, involving the breaking of bonds and therefore requiring considerable energy to change bonding type from covalent to metallic.[27] As this phase transformation is difficult in bulk, the fewer potential nucleate sites available, due to the small volume of SiNWs, makes it even more difficult to nucleate β-Sn-Si. This raises the pressure of the phase transformation and sometimes, for the smaller SiNWs and Si nanoparticles,[94] caused a direct dc-Si to sh-Si transformation.

The sh-Si to β-Sn-Si/Imma-Si phase transformation was found to occur at similar pressures for both bulk-Si and nano Si. This metal to metal phase transformation is displacive in nature, involving the movement of some atoms in each unit cell.[27] The total free energies of β-Sn-Si, Imma-Si and sh-Si were found to be similar in a theoretical study.[30] The displacive nature of the sh-Si to β-Sn-Si phase transformation and the similarity in free energies of the structures might explain why the sh-Si to β-Sn-Si/Imma-Si phase transformation pressure was similar for both bulk-Si and nano Si, which nucleation was not a problem.

The next expected phase transformation, based on the results from bulk-Si,[5] involves β-Sn-Si, with metallic bonding, transforming to r8-Si, which has covalent bonding. Following on from the previous argument, the nucleation of covalent r8-Si from β-Sn-Si would

be expected to have a significantly high kinetic barrier. Similar to the dc-Si to metallic phase transformation, the small size (volume) of the SiNWs limits the number of potential r8-Si nucleation sites and therefore leads to a difficulty in nucleating this phase. Hence, it is observed that the SiNWs can remain β-Sn-Si until a much lower pressure than for bulk-Si. The formation of a-Si is also a result of the difficulty in nucleating the r8-Si phase. We note that difficulty in the nucleation of r8-Si also happens in rapid decompression during nanoindentation of Si.[75,76] This rapid decompression leads to insufficient time for r8-Si to nucleate but r8-Si can form when more time is given for decompression.[75,76] Regarding the SiNWs, it is possible that the smaller volume of SiNWs is somewhat like the rapid decompression in nanoindentation, resulting in nucleation difficulties for r8-Si in SiNWs due to the lack of nucleation sites rather than the lack of time. As pressure is decreased β-Sn-Si becomes unstable and if no crystallines phases can form, a-Si forms becomes more thermodynamically favourable at this highly depressed pressure. In the larger SiNWs (200-250 nm), there are more potential nucleation sites due to the larger size and therefore r8-Si nucleation is less difficult and can form in some SiNWs.

3.8 Conclusions

It is clear that there is a size effect on the high pressure phase transformation behaviour of Si. Small SiNWs and Si nanoparticles phase transform at elevated pressures on compression, sometimes even bypassing the β-Sn-Si phase. On decompression, β-Sn-Si remains until much lower pressures than bulk-Si, and a-Si is the dominant end phase. For intermediately sized SiNWs (200-250 nm), the dc-Si to β-Sn-Si phase transformation is less elevated than in smaller SiNWs, and on decompression r8/bc8-Si is sometimes able to form at a slightly lower pressure ($\sim$8-5 GPa) compared to bulk-Si. For the largest SiNWs, the phase transformation behaviour is reported to be similar to bulk-Si.[110] This size effect can be attributed to the small volume of the SiNWs making it difficult to nucleate new phases.

Although some crystalline bc8-Si can form under very slow decompression or larger diameter SiNWs, high pressure alone cannot be used to reliably produce bc8-SiNWs. Thus, to promote the formation of this technologically useful phase other factors must be explored together with high pressure. It has been reported that high temperature in nanoindentation can increase the formation of r8/bc8-Si.[107] Furthermore, low temperature high pressure work on bulk-Si has been shown to inhibit the nucleation of r8-Si allowing a-Si to form,[22,100] Therefore, it might be possible to use a combination of both pressure and temperature in order to more reliably form bc8-Si in SiNW. This will be the focus of the next chapter where the effect of temperature on the final phases formed after high pressure compression and decompression of bulk-Si and SiNWs will be explored.

Chapter 4

High temperature behaviour of SiNWs

In the previous chapter, it was established that the high pressure phase transformation behaviour of Si has a size dependence. In particular, the small volumes of the SiNWs were observed to suppress the nucleation of new phases such as r8-Si. A possible way to overcome this issue is to increase the temperature during compression and decompression. The main focus of this chapter is the effect of temperature on the high pressure phase transformations of 80-150 nm SiNWs.

4.1 Introduction

Earlier it was discussed that it would be highly desirable to exploit the interesting properties of bc8-Si, r8-Si and hd-Si by forming them in SiNWs. Currently, bc8-SiNWs cannot be produced using conventional growth. In the case of hd-Si, it can only be formed in small regions of NWs either via the application of compressive stresses or by heteroepitaxial growth off GaP NWs.[2,145] However, both methods produce NWs that are not pure hd-Si with the latter method producing NWs with Ga and P impurities which would affect the properties of the NWs.

In the previous chapter, it was shown that for 80-150 nm SiNWs, a-Si was the dominant end phase after high pressure treatment. The formation of bc8-Si was only observed to occur in larger 200-250 nm diameter SiNWs or under extremely slow decompression. In light of the difficulty to nucleate r8-Si in 80-150 nm diameter NWs, it might be possible to encourage r8-Si (which phase transforms to the desirable bc8-Si on further decompression) to more reliably nucleate in 80-150 nm diameter SiNWs by increasing the temperature during compression and decompression.

In this chapter 80-150 nm diameter SiNWs are compressed and decompressed at 25-165°C and compared with bulk-Si compressed under similar conditions. It will be shown that there is a clear temperature dependence on the phase transformations of SiNWs that differs from bulk-Si. Additionally, it will be shown that predominantly phase-pure bc8-SiNWs can form at higher temperatures and that the dc-SiNWs can directly form from β-Sn-SiNWs.

4.2 Experimental Method

Preparation of the SiNWs

The SiNWs were grown by the vapour-liquid-solid method in the ⟨111⟩ direction to a diameter 80-150 nm and length of 5 μm using Au as a catalyst.[140] Further details of the growth can be found in Chapter 3. After growth, the Au was removed from the SiNWs by first etching the native oxide using hydrofluoric acid and then placing the SiNWs into an aqua regia solution.

Diamond anvil cell compression of SiNWs

Symmetric DACs with a 400 μm culet, and a stainless steel gasket (preindented to ∼50 μm in thickness with a 200 μm diameter hole drilled with the HPCAT laser drilling system[146] were used to compress the samples. The SiNWs were removed from their substrate using a stainless steel razor blade and loaded into the DAC along with a small ruby ball. Ne, that was loaded using the GSECARS gas loading system,[147] was used as a pressure medium. In separate loadings, single crystal ⟨100⟩ oriented Si wafers with a 15±2 μm thickness were compressed using a similar method.

The DACs were compressed using a double membrane system at HPCAT.[130] The DAC and membrane system was placed into a resistive heating block with a type K thermocouple connected the outside of the block. The DACs containing the SiNWs were heated to 25, 70, 105, 135 and 165°C before compression, allowing at least one hour for the temperature to equilibrate. The bulk-Si samples were heated to 105 and 165°C. Once equilibrated, the samples were compressed to ∼20-22 GPa, such that the SiNWs had completely phase transformed to the metallic sh-Si phase, as described in the previous chapter. The samples were then decompressed to 9-10 GPa and then decompressed to 2-3 GPa at a rate of ∼2 GPa/hr (5.6 x 10^{-4}GPa/s). The ruby fluorescence method was used to monitor the pressure within the cell.[129]

Characterisation using XRD and TEM

Following the compression and decompression, the gasket containing the sample was removed from the DAC. X-ray diffraction was performed on the 16-ID-B beamline at HPCAT at the Advanced Photon Source in Argonne National Laboratory. A 31 keV beam (for the SiNWs) or 25 keV beam (bulk-Si)[i] with a spot size of 4x6 μm was used. A 2D powder diffraction pattern was collected for 120-180 s (SiNWs) or 30 s (bulk-Si) using a Pilatus 1-M-F detector. Background air scattering measurements were collected by focusing the beam through an empty gasket with a similar diameter hole to the samples. These background measurements were subtracted from the XRD images before integration using Dioptas to form 1D diffraction patterns.[134]

After XRD, the SiNWs were removed from the gaskets with a stainless steel needle and transferred into a small container of isopropanol. The SiNWs were then ultrasonicated

[i]The different energies used were a result of the setting chosen by the previous user and does not affect the results in Q space.

and subsequently dispersed onto a copper lacey carbon TEM grid with a micropipette. The SiNWs were then examined using TEM [Hitachi HF3300 operating at 300 kV (ORNL) and Jeol 2100F operating at 200 keV (ANU)].

In situ measurements

In addition to the *ex situ* measurements described above, some *in situ* measurements were also made. A DAC was loaded with SiNWs and a < 1 μm thick platinum chip. The DAC was placed inside the same resistive heating block and double membrane system as the *in situ* measurements and then irradiated with the same 31 keV x-ray beam. The sample was heated to 105°C and allowed an hour for the temperature to equilibrate. Cubic boron nitride was used for the seat in the downstream direction to allow for a higher region of Q to be probed due to its x-ray transparency.

The pressure was increased until dc-Si was no longer present and then decreased slowly. The pressure was then decreased slowly. XRD measurements (10 s accumulations) were taken during both compression and decompression. The equation of state of Pt was used to determine the pressure within the cell.[148] Pt was chosen as a calibrant due to its low overlap with the XRD reflections of the various phases of Si compared with Au and the requirement to know the pressure whilst constantly monitoring the phase of the SiNWs during decompression.

Thermal stability of bc8-Si nanowires

Two samples, one bulk-bc8-Si and one containing bc8-SiNWs were prepared. These samples were both polycrystalline. Bulk-bc8-Si was formed by compressing single crystal bulk-Si at 105°C and decompressing at 2 GPa/hr. A mixture of essentially phase pure bc8- and dc-SiNWs was formed by compressing 80-150 nm diameter SiNWs at 120°C and subsequently decompressing at a rate which allowed the formation of bc8-Si or dc-Si NWs.

These samples were annealed in their gaskets simultaneously (to allow for direct comparison between bulk-bc8-Si and the bc8-SiNWs) in a Fischer Scientific Isotemp vacuum oven model 282A. The samples were annealed at 120, 140, 150, 160, 170, 180, 190 and 200°C for a period of 30$\pm$1 minutes. Power diffraction patterns were collected on the 16ID-B beamline of the Advanced Photon source at Argonne National initially and after each annealing period. A 6x6 grid size map with a collection time of 5 s per point over a 40x40 μm^2 region at the centre of each sample was collected. The powder images that did not contain impurities were averaged using XDI and these were then integrated (with background subtraction) using Dioptas.[134,149]

4.3 XRD results of SiNWs during and after compression

The end phases after compression and decompression of bulk-Si at different temperatures are shown in Fig. 4.1. At ambient temperature at 105°C, the end phase is found to be

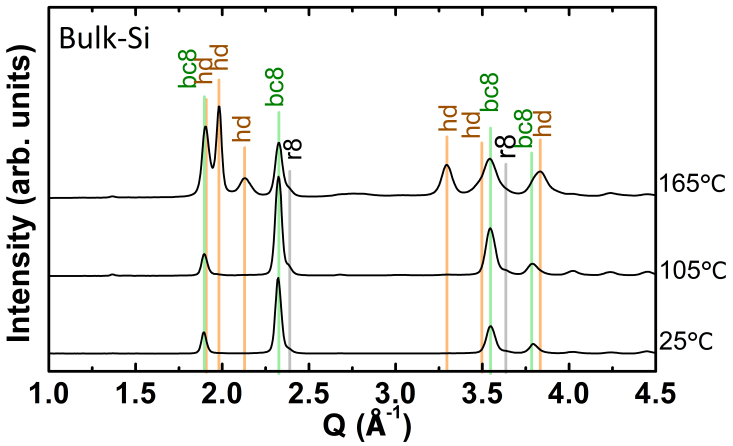

Figure 4.1: Powder diffraction patterns of bulk-Si after compression to ∼20-22 GPa and decompression at ∼2 GPa/hr between 9-3 GPa at the indicated temperature. All measurements were made at ambient temperature and pressure. The most prominent peaks of each phase are labelled.

essentially bc8-Si. This is consistent with literature where dc-Si phase transforms to β-Sn-Si at ∼11 GPa and then to sh-Si at ∼15 GPa on compression,[26] On decompression, sh-Si phase transforms to β-Sn-Si,[26] and then to r8-Si between 10-8 GPa, which then phase transforms to bc8-Si at lower pressures.[5,6] At higher temperatures (165°C), a different end phase is observed in addition to bc8-Si. Here the end phase is a mixture of bc8-Si and hd-Si (with small traces of dc-Si). This is consistent with bc8-Si phase transforming to hd-Si upon annealing.[102]

During compression it was important to ensure that complete phase transformation to sh-Si was achieved so that no dc-Si remained following compression. The reason for this will become clearer once the results are presented. To do this, *in situ* measurements on decompression were performed to allow for a better understanding of the phases that nucleated from β-Sn-Si. The phase transformations observed *in situ* for the SiNWs at 105°Cs are now presented in Fig. 4.2 and 4.3 for compression and decompression, respectively. These figures show a series of *in situ* XRD. The Si peaks were identified by comparing with the literature.[13] The behaviour observed is complicated by the fact that the XRD spot size is ∼4x6 μm^2 and hence this result essentially averages over many NWs. Individual SiNWs were investigated using TEM which will be shown later. TEM indicated that individual SiNWs phase transformed to predominately one phase during decompression. Therefore the behaviour of SiNWS is more complex than bulk-Si.

During compression (Fig. 4.2), the SiNWs start in the dc-Si phase before partially phase transforming to β-Sn-Si at 11.5 GPa. The phase transformation continues until 13.8 GPa where the β-Sn-Si and any dc-Si still present begin to phase transform to sh-Si. At 16.6 GPa, the SiNWs appeared to have completely phase transformed to sh-Si.

Upon decompression (Fig. 4.3), the sh-Si phase transforms to β-Sn-Si (possibly via Imma-Si). Between 9.3 GPa and 7.9 GPa, the β-Sn-Si gradually phase transforms to a mixture of dc-Si and r8 or bc8-Si. Due to the low intensity of the r8 or bc8-Si signal, it is difficult to determine which of the two phases is present. However, by inferring from the bulk-Si literature, it is most likely that r8-Si is present.[6] Based on the behaviour of

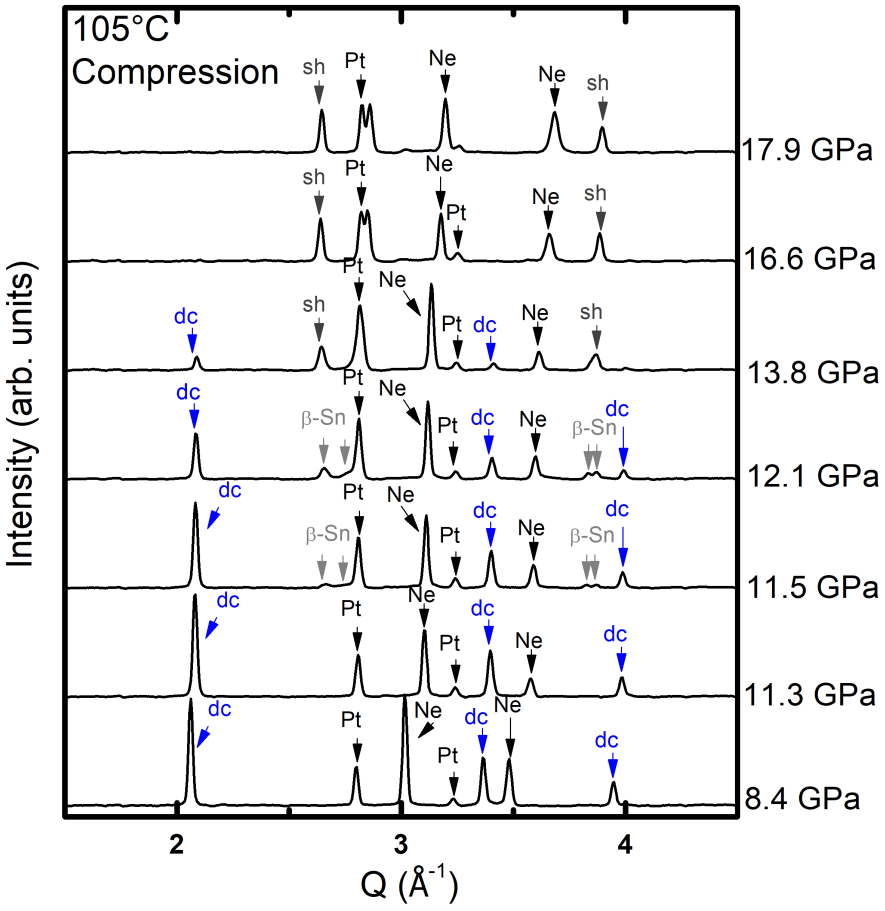

Figure 4.2: Powder diffraction patterns of SiNWs taken *in situ* during compression at 105°C.

bulk-Si, this r8-Si is expected to phase transform to bc8-Si at lower pressures.

Representative powder diffraction patterns of the final phases averaged over all NWs compressed a 25-165°C are shown in Fig. 4.4. After compression and decompression at ambient temperature, the powder diffraction pattern indicates that the SiNWs are no longer entirely dc-Si. Instead, the pattern is dominated by two broad features at Q=∼2.01 $\AA$ and 3.47 $\AA$, which correspond to a-Si. In addition to these broad features, several sharper peaks are also present. These can be indexed to dc-Si and bc8-Si. Note that for equal volumes of material, the intensity of a-Si in XRD is typically much lower than the intensity of crystalline phases. This suggests that the SiNWs are predominately a-Si with trace amounts of the crystalline dc-Si and bc8-Si phases. Nether a-Si nor dc-Si form in bulk-Si under these decompression conditions, indicating that bulk-Si and SiNWs have different phase transformation behaviours under these conditions.

When increasing the temperature to 70°C, more crystalline phases and less a-Si are observed. The fraction of the crystalline phases (dc-Si and bc8-Si) relative to a-Si continues to increase as the temperature of compression is raised to 105°C and 135°C. At these two temperatures, all recovered SiNWs appear to be predominately crystalline, with the dc-Si to bc8-Si ratio varying across different regions of the sample. Intriguingly, dc-Si does not form on decompression from β-Sn-Si for a bulk-Si starting material until 170°C.[101]

At the highest temperature (165°C), dc-Si was the most dominant phase formed and

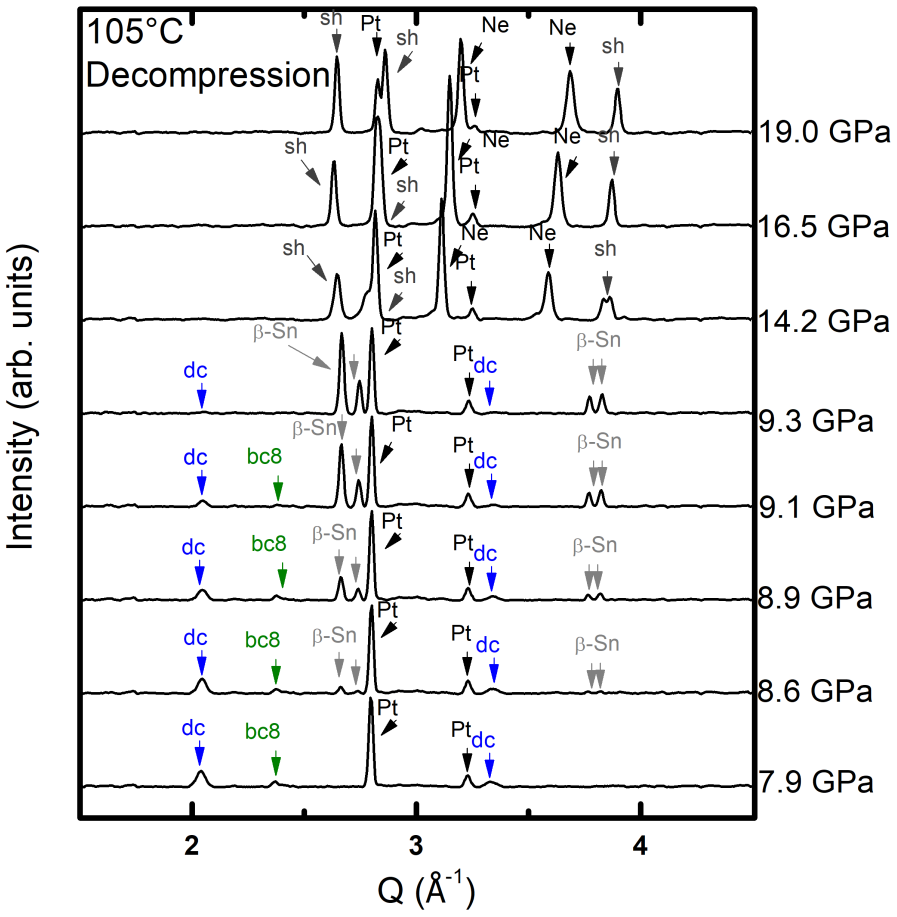

Figure 4.3: Powder diffraction patterns of 80-150 nm SiNWs taken *in situ* during decompression at 105°C. Note that Pt was used as a pressure calibrant and Ne was used as the pressure medium.

only a small amount of bc8-Si was observed. Note that some hd-Si might have formed in the SiNWs but due to the overlap of the main hd-Si peaks with bc8-Si and/or dc-Si peaks, it is difficult to determine if hd-Si is present. Once again, the end phases observed in the SiNWs differed to bulk-Si, where bc8-Si and hd-Si were observed.

From these data, it is quite clear that SiNWs have significantly different high pressure phase transformation behaviour to bulk-Si. This difference in behaviour is pressumably due to the small volume or high surface to volume ratio which results in the suppression of nucleation of the crystalline phases in the SiNWs, as presented in Chapter 3. To further understand this behaviour, the microstructure and phases present in individual SiNWs was also studied using TEM.

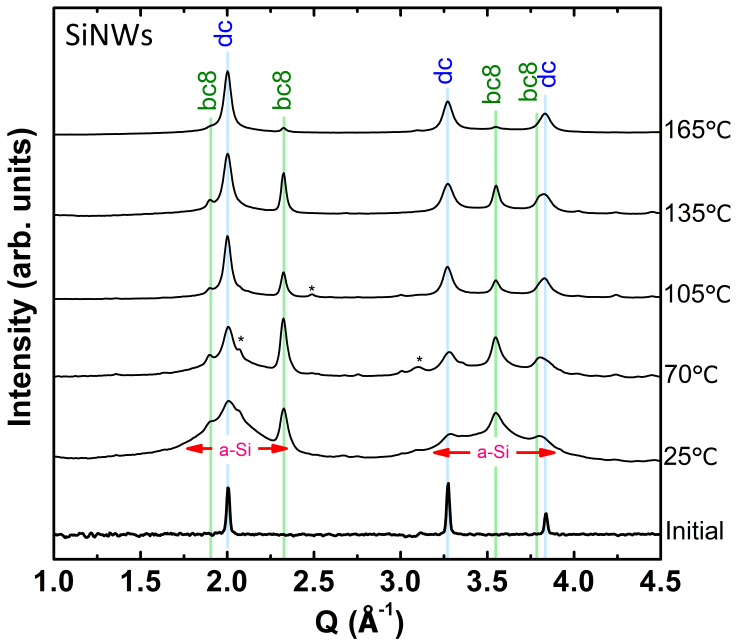

Figure 4.4: Powder diffraction patterns of 80-150 nm SiNWS after compression to ∼20-22 GPa and decompression at ∼2 GPa/hr between 9-3 GPa at the indicated temperature. All measurements were made at ambient temperature and pressure. The peaks indicated by asterisks are thought to be from impurities from the gasket.

4.4 Transmission electron microscopy study of SiNWs after compression and decompression

The TEM data in general indicated that individual SiNWs remained intact[ii] and appeared to be predominately a single phase, either a-Si, bc8-Si or dc-Si. This is in agreement with the XRD data, despite the XRD data indicating multiple phases present over many SiNWs, as the phases observed in TEM match those observed in XRD. When crystalline phases formed in SiNWs, they were found to be polycrystalline.

Representative TEM images of SiNWs that were compressed at ambient temperature are shown in Fig. 4.5. Figure 4.5 (a) shows a DF image of a SiNW with an inset of a SADP taken from the SiNW. Note that the width of the SADP is 15.5 nm^{-1} and this is the same for all the SADPs in this chapter. This SADP contains weak diffuse rings, indicating the presence of a-Si, as well as diffraction spots which correspond to bc8-Si. The DF image is composed of the diffracted electrons from the spot circled [a (112) reflection of bc8-Si], and indicates that the bc8-Si is distributed across the SiNW, which also contains a-Si. A DF image of several different SiNWs is shown in Fig. 4.5 (b). A SADP taken from all these SiNWs collectively can be found in the inset. This SADP contains diffuse rings corresponding to a-Si and several spots which can mostly be indexed to dc-Si. Note that the DF image is formed from the circled spot, a (111) dc-Si reflection (which also contains some of the diffuse a-Si ring). This image reveals that most of the

[ii] Although some of the SiNWs are observed to be "bent" after compression, several NWs were also "bent" before compression (see Fig. 3.1). It is not known how this occurs.

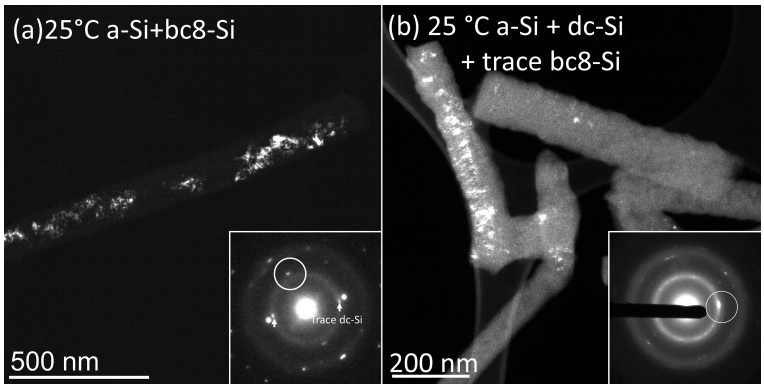

Figure 4.5: TEM images illustrating typical end phases in SiNWs after compression to ∼20 GPa at ambient temperature. (a) A DF image of a SiNW containing bc8-Si and a-Si from from the encircled spot in the inset SADP, (b) A DF image of a group of SiNWs containing dc-Si and a-Si formed from the encircled spot in the inset SADP. (courtesy Dr David Cullen, ORNL)

dc-Si present is contained in one SiNW, whilst the other SiNWs in the image are almost entirely amorphous. From these images, it appears that SiNWs compressed at ambient temperature are either (i) entirely a-Si, (ii) a mixture of bc8-Si and some a-Si or (iii) dc-Si and some a-Si. This is consistent with the XRD data where a-Si is the dominant phase but there are trace amounts of bc8-Si and dc-Si.

When the SiNWs were compressed at higher temperatures (70°C, 105°C and 135°C), the recovered SiNWS were found to be mostly polycrystalline dc-Si or bc8-Si with only traces of a-Si. At the highest temperature studied (165°C), all SiNWs observed in TEM were polycrystalline dc-Si.[iii] Figure 4.6 shows a series of representative TEM images of SINWs that were compressed at higher temperatures. Figure 4.6 (a) contains a DF image of a SiNW compressed at 105°C which is composed of the circled spot in the inset SADP. This suggests that this SiNW is predominately bc8-Si.[iv] Due to multiple crystallites being visible, it is clear that this SiNW is also polycrystalline. Other SiNWs compressed at this temperature were found to be predominately dc-Si. An example of a DF image [from the circled (111) reflection of dc-Si] of two SiNWs where dc-Si dominated, with an inset SADP, is shown in Fig. 4.6 (b). Like the previous example, there is no clear evidence of a-Si in the SADP and the SiNWs are also polycrystalline. At this temperature, no entirely amorphous SiNWs were detected, this was consistent with the XRD data. TEM of the SiNWs that were compressed at 135°C were very similar to the images of SiNWs compressed at 105°C. An example is shown in Fig. 4.6 (c) which contains a polycrystalline bc8-SiNW. An example of SiNWs that were compressed at 165°C is shown in Fig. 4.6 (d). These SiNWs contained polycrystalline dc-Si, as indicated by the rings of spots in the inset SADP, consistent with XRD data where dc-Si was the dominant phase.

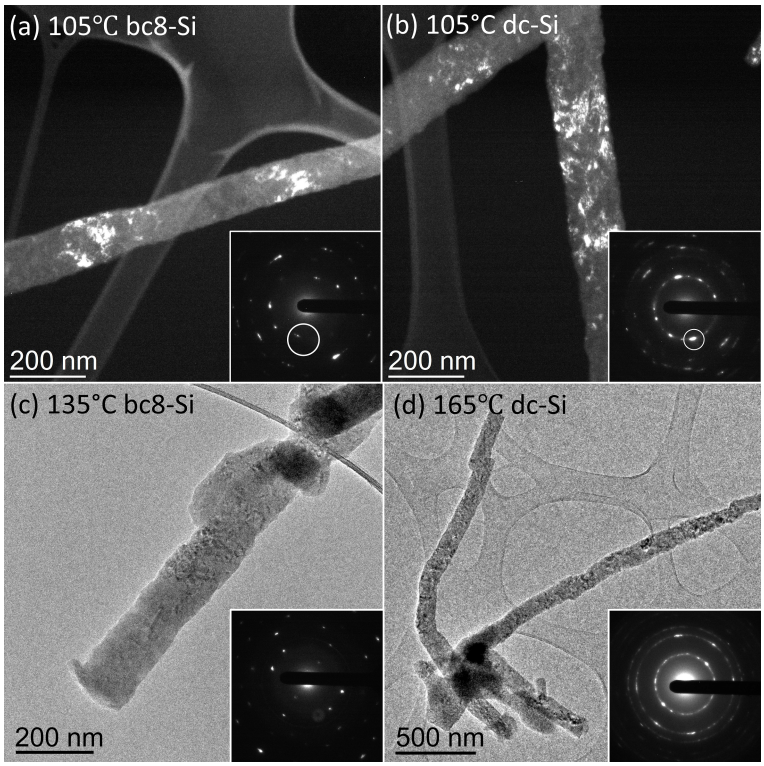

Figure 4.6: TEM images of SiNWs compressed to ∼20 GPa at temperatures ranging between 105-165°C. Each image contains an inset SADP taken from the SiNW shown. (a) A DF image (from the circled spot) of a SiNW compressed at 105°C containing bc8-Si, (b) A DF image (from the circled spot) of a SiNW compressed at 105°C containing predominately dc-Si, (c) A BF image of a SiNW compressed at 135°C containing predominately bc8-Si, (d) A BF image of a SiNW compressed at 165°C containing predominately dc-Si. (All images were taken by Dr David Cullen, ORNL)

4.5 Thermal stability of bc8-SiNWs

It is clear from the previous section that raising the temperature at which SiNWs are compressed affects the final phase recovered at ambient pressure and allows for bc8-Si to form. The stability of bc8-SiNWs is therefore of interest as nanoscale volumes of other metastable phases of Si and Ge (such as st12-Ge[68]) have different temperature stabilities to their bulk counterparts.

Figure 4.7 contains the integrated XRD powder patterns after each incremental 30 min anneal for (a) the SiNWs and (b) bulk-Si. Initially, the bulk Si is predominately bc8-Si, as indicated by the series of peaks marked with green lines. Bulk-Si remains in this phase until 140°C where a peak at Q=∼1.96 $\AA$, which corresponds to hd-Si becomes apparent. This peak, as well as several other peaks, marked with orange lines, increases in intensity with each incremental anneal until the 190°C anneal where bc8-Si is no longer present. This indicates that there is a bc8-Si to hd-Si phase transformation in bulk-Si

[iii]It is likely that bc8-Si was not observed due to the small amount of bc8-Si observed in the XRD data.

[iv]As bc8-Si is denser than dc-Si, it would be expected that the volume of this SiNW would be lower than its initial volume, however, this change in volume cannot be measured by TEM.

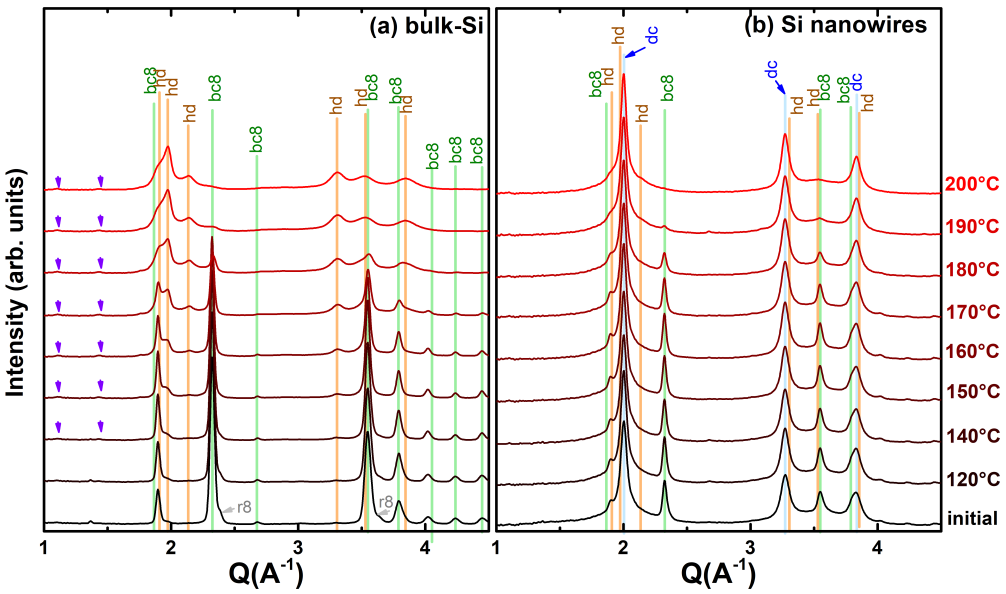

Figure 4.7: Powder diffraction patterns of (a) bulk-Si and (b) SiNWs, taken at ambient temperature after 30 min incremental annealing at the temperatures up to 200°C. The purple arrows indicate the presence of a peaks that may be characteristic of the Si-XIII phase.[102]

which is completed by 190°C. Although this phase transformation is consistent with the literature, hd-Si is not the only phase that forms during the annealing of this sample. At 140°C and above, two weak additional peaks at Q=1.10 $\AA$ and 1.43 $\AA$ (labelled with purple arrows) are observed which are consistent with the reflections observed in Si-XIII, a phase of Si with an unknown structure.[102] Raman spectroscopy of the sample after the final annealing step (not shown) confirmed the presence of Si-XIII. Interestingly, Si-XIII has only previously been reported to occur after the annealing of the r8/bc8-Si phase formed via nanoindentation,[19,102] and not from bc8-Si formed in a DAC.

The behaviour of bc8-SiNWs during annealing under the same conditions as bulk-Si is a little more difficult to discern due to the presence of both dc-Si and bc8-SiNWs in the starting sample. XRD patterns of this sample are shown in Fig. 4.7 (b). Initially these SiNWs are a mixture of both dc-Si and bc8-Si. The powder diffraction patterns appear to be quite similar until the anneal at 170°C where the bc8-Si peaks drop in intensity. These peaks continue to decrease in intensity until 200°C where they are no longer present. After annealing at 200°C, peaks at Q=1.97 $\AA$ and 3.52 $\AA$ become apparent, indicating that the bc8-SiNWs have phase transformed to hd-Si, like bulk-Si. Due to the overlap of the main hd-Si peaks with either dc-Si or bc8-Si, it is difficult to tell whether there is hd-Si present until bc8-Si is no longer present [which is confirmed by the disappearance of the most prominent bc8-Si (112) peak at Q=2.32 $\AA$]. It therefore appears that bc8-SiNWs undergo a phase transformation to hd-Ge which occurs most prominently between 170-200°C. This appears to be quite similar to bulk-Si, however, the presence of dc-Si in the NW case and also the overlap of dc and bc8 peaks with the hd peaks makes it difficult to conclusively determine if subtle differences exist. In particular, the behaviour in the 140-160° range where bulk-Si starts to phase transform cannot be probed in the SiNWs. This is due to the high intensity of the dc-Si peaks. Given that the behaviour at 150-

200°C is very similar to bulk-Si, it is likely that the bc8-Si to hd-Si phase transformation occurs very slowly between 140-160°C as in bulk-Si. In addition, due to the low intensity of the peaks that are unique to Si-XIII, it is not possible to determine if Si-XIII formed in the SiNWs. Both these complexities could be resolved if the recovered sample contained entirely bc8-SiNWs.

4.6 Discussion

It is clear that the compression of SiNWs at high temperatures leads to interesting phase transformation behaviour that differs from bulk-Si. Key observations are provided in table 4.1.

Table 4.1: Summary of the final phases observed after compression and decompression of SiNWs and bulk-Si at various temperatures.

Temperature	Bulk-Si	SiNWs
Ambient	bc8-Si (trace r8, polycrystalline)	a-Si
70°C	-	bc8-Si and/or dc-Si (polycrystalline, trace a-Si)
105°C	bc8-Si (trace r8, polycrystalline)[102]	bc8-Si + dc-Si (polycrystalline)
165°C	bc8-Si + hd-Si (polycrystalline)	Predominately dc-Si (polycrystalline)

A schematic of the phase transformation pathways in bulk-Si and SiNWs is shown in Fig. 4.8. The phase transformation pathways of bulk-Si are shown on the left and the SiNWs on the right. A rough phase diagram for the SiNWs during decompression can be found in Appendix A. For bulk-Si, the end phases after decompression are consistent with previous studies,[5,101,102] as has already been discussed. In bulk-Si the onset of the β-Sn-Si to r8-Si phase transformation at ambient temperature is reported to occur at $\sim$10 GPa.[5,6] In contrast, for NWs the formation r8-Si (from β-Sn-Si) during decompression occurs at lower pressures when compared to bulk-Si (particularly at lower temperatures) due to difficulties in the nucleation. As with the formation of r8-Si, remaining β-Sn-Si becomes more unstable as pressure is reduced, which means that the driving force to phase transform increases. At ambient temperature, some (β-Sn)-Si phase remains down to 5-6 GPa, which is 3-4 GPa below the normal bound of its stability range in bulk-Si. As β-Sn-Si is very unstable at this pressure, a-Si is formed. When crystalline phases do nucleate, in a few SiNWs, the pressures at which they occur are lower than in bulk-Si and a-Si is also found in the same SiNWs, possibly suggesting that growth is suppressed.

More thermal energy is available when decompressing at intermediate temperatures. This extra thermal energy is thought to assist with the growth of crystalline phases such as dc-Si, bc8-Si and r8-Si. This means that unlike at ambient temperature, the β-Sn-Si to r8-Si phase transformation is no longer fully suppressed and occurs in some of the SiNWs.

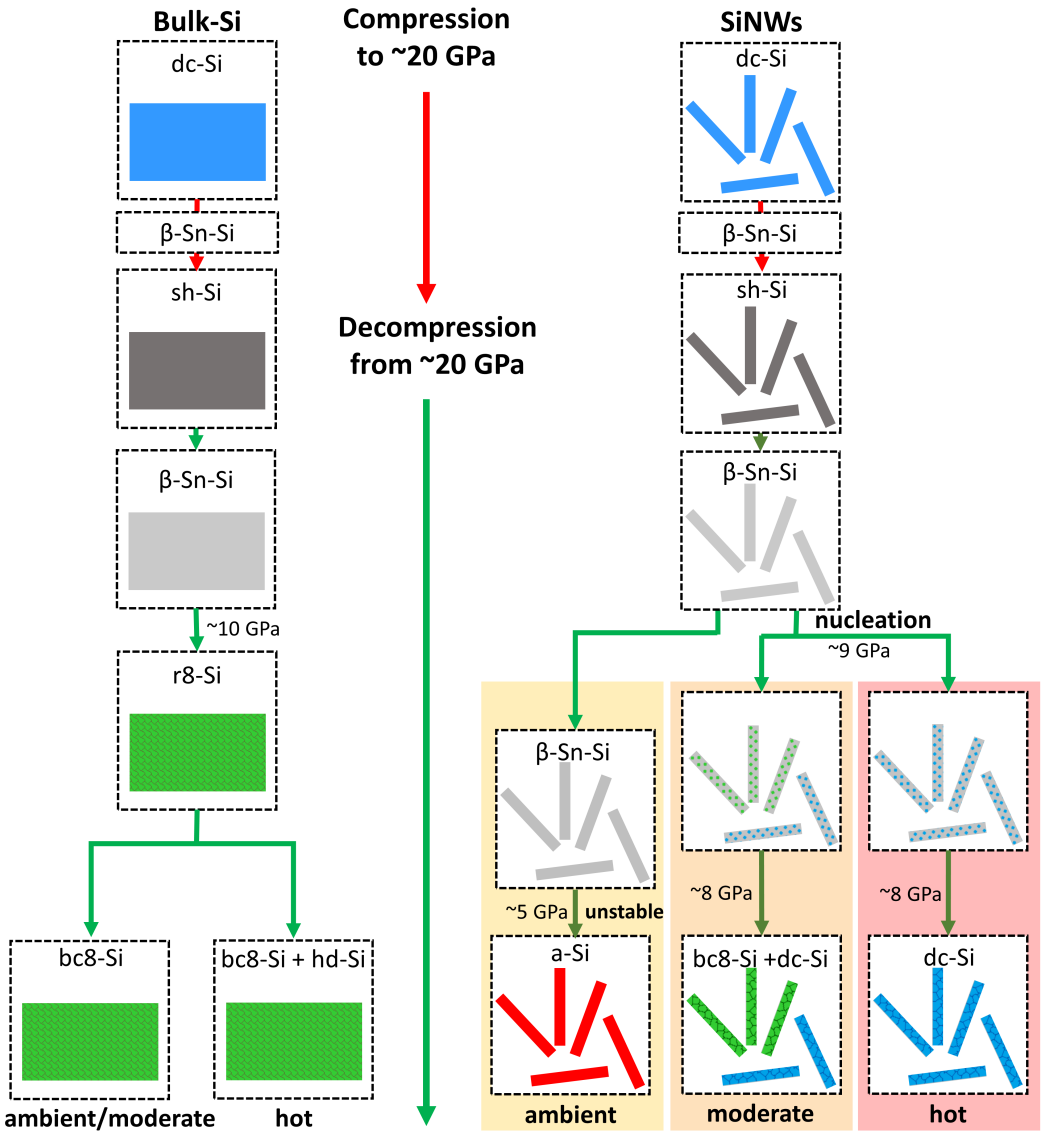

Figure 4.8: A schematic diagram of the phase transformation behaviour of bulk-Si and SiNWs.

The various phase transformation pathways observed after decompression of β-Sn-Si at elevated temperatures will now be examined in terms of thermodynamic and kinetic considerations. Rapp et al.[11] recently calculated the relative enthalpy of various allotropes of Si vs pressure and found that dc-Si would form from β-Sn-Si if there were no kinetic energy barriers for phase transformation. However, the kinetic barrier to form dc-Si from β-Sn-Si around 10 GPa is high,[28] making dc-Si hard to form in bulk-Si. The second lowest enthalpy allotrope below ~10 GPa is hd-Si.[11] This phase has some similarities in structure to dc-Si and therefore a high kinetic barrier to phase transformation is also anticipated. Indeed, the phase with the next lowest enthalpy between about 10 and 2 GPa is r8-Si.[11] This is consistent with the β-Sn-Si to r8-Si phase transformation, and the r8-Si to bc8-Si phase transformation at ~3 GPa observed in bulk-Si at ambient temperature.[5,6] The barrier for the β-Sn-Si to r8-Si phase transformation was reported by Wang et al[28] to be much smaller than that of the β-Sn-Si to dc-Si phase transformation. This is the reason that bc8-Si, not dc-Si, is the dominant end phase after decompression when

bulk Si is the starting material. It is therefore somewhat surprising that dc-Si forms directly from β-Sn-Si. However, the nucleation of crystalline phases from β-Sn-Si in SiNWs is suppressed and highly unstable β-Sn-Si can remain until lower pressures. If there is sufficient thermal energy available, such as at high temperatures, the barriers to formation of all crystalline phases may be significantly reduced, allowing them to nucleate. It might be anticipated at high temperatures, the barrier to the formation of the lowest enthalpy dc-Si phase can be overcome and hence dc-Si crystallites form. In this case, this process is dominant at 165°C. Additionally, it has previously been shown that the growth of dc-Si is significantly enhanced by an order of magnitude by the application of a modest pressure of 2 GPa.[150–152] Therefore, if dc-Si was to nucleate, it might be expected to grow relatively fast under high pressure and temperatures. This scenario could explain why dc-Si is the dominant phase at 165°C. Additionally, at lower temperatures where the barrier to formation of dc-Si is more significant, it may be more energetically favourable for r8 and bc8-Si to nucleate in SiNWs from β-Sn-Si under decompression. Finally, if there is insufficient energy to overcome the energy barriers and nucleation is suppressed, this may lead to a-Si formation. This is consistent with the observation of a-Si being dominant at lower temperatures.

Finally, note that a-Si has also been observed as the end phase in other scenarios where nucleation is suppressed such as rapid decompression of bulk-Si in a DAC,[33,34] as well as under moderate to high unloading rates in nanoindentation experiments.[75,78,80] In fact comparison of the phase transformation of SiNWs to the phase transformations observed in nanoindentation is particularly relevant. This is because nanoindentation is another method which can be used to cause small volumes of Si to phase transform and therefore size effects are relevant. This will be further explored in the next chapter where the phase transformation behaviour of SiNWs is compared to that experienced in nanoindentation.

4.7 Conclusions

By subjecting SiNWs and bulk-Si to temperature ranging from 25-165°C during compression and decompression, it has been shown that there is a clear temperature dependence on the high pressure phase transformations of SiNWs that differs from bulk-Si. At ambient temperatures, a-Si is the dominant end phase in SiNWs whilst in bulk-Si, bc8-Si was the dominant end phase. In the intermediate temperature range (70-135°C), both bc8-Si and dc-Si formed in the SiNWs, whilst bc8-Si was still the dominant phase for bulk-Si. At the highest temperature (165°C), dc-Si was the dominant end phase in the SiNWs whilst a mixture of hd-Si and bc8-Si formed in bulk-Si. From examining individual SiNWs using TEM, it appears that the SiNWs phase transform independently of each other and near phase pure bc8-SiNWs and dc-SiNWs were formed. The bc8-SiNWs were found to have a similar temperature stability and temperature induced phase transformations to bulk-Si.

Chapter 5

A comparison of the phase transformations observed in Si nanowires at high pressures and nanoindentation of Si

The previous chapters have clearly shown that SiNWs at both ambient and high temperatures undergo different phase transformation pathways when compared to bulk-Si. However, the compression of SiNWs is not the only method for producing small volumes of phase transformed material. It is also possible to use nanoindentation.[1,80] Unlike a DAC, nanoindentation is affected by large pressure distributions, high shear and the presence of surrounding material that is not phase transformed.[1] The aim of this chapter is to compare the two techniques in the regime where the depth of the phase transformation volume induced by nanoindentation approaches the diameter of the SiNWs.

5.1 Introduction

Another method of inducing phase transformations in Si is nanoindentation. When using this method, a region of β-Sn-Si is formed underneath a tip on loading and this phase transforms to either r8/bc8-Si or a-Si on unloading.[75,78] The volume of this region of phase transformed material is determined by a combination of the tip chosen and the load applied. It is therefore possible to choose a combination of indenter tip and maximum load that induces a phase transformation volume where its depth approaches the diameters of the SiNWs studied in the previous chapters.

DAC loading and nanoindentation have significant differences that are worth noting. For example, DAC loading can be essentially hydrostatic, with minimal pressure gradients across the compressed volume when using an appropriate pressure medium. In contrast, there are large hydrostatic and shear pressure gradients underneath the tip in nanoindentation. These hydrostatic and shear stresses result in the competition between phase transformation (where the hydrostatic component is high) and the nucleation and propagation of defects (where the shear component is high).[76,81] Secondly, since only the material directly underneath the nanoindentation tip is under pressure (as opposed to all of the material in a DAC) the surrounding material might affect the final phase formed. Finally, the phase transformation volumes (typically sizes of hundreds of nm to μm in

depth and ∼1-10μm in diameter))[80,114] in nanoindentation are typically much smaller than the volume of material in a DAC (∼50x50x20 μm). This might lead to the volume difference in nanoindentation and DAC compression of bulk-Si influencing the end phase formed, similar to the different behaviours observed in SiNWs vs bulk-Si.

Previous nanoindentation studies where a small phase transformation volume was observed, resulted in somewhat similar end phases to the SiNWs, with a-Si and r8/bc8-Si forming at ambient to moderate temperatures,[107,153] and a dc-Si end phase at high temperatures.[107] The observation of dc-Si as an end phase was believed to be a result of an enhanced formation of defects during loading (which reduced the pressure under the tip meaning that phase transformation did not occur) rather than a direct phase transformation from β-Sn-Si to dc-Si during unloading. As the phase transformation pathway of β-Sn-Si to dc-Si was observed for SiNWs in Chapter 5, it is worth also considering the possibility of this phase transformation pathway in nanoindentation.

In this chapter, the similarities and differences between the phase transformation behaviour of SiNWs and nanoindented Si (both dc-Si and a-Si) will be explored. Here, the ongoing theme of nucleation suppression due to small volumes will be explored in nanoindentation by choosing a maximum load and tip that produced a phase transformation volume with a depth of ∼150 nm (as confirmed by TEM). This allows for a comparison with the SiNWs, as the depth of the phase transformation zone had the same order of magnitude to the diameter of the SiNWs. Additionally, the effect of decompression rate and temperature will also be studied.

5.2 Experimental Method

The following sections briefly outline the details of the experimental procedures used in this chapter.

DAC details

The SiNWs were grown using the vapor liquid solid method, as outlined in Chapter 3. Following growth, the Au was removed by dipping the sample into hydrofluoric acid to first remove the native oxide, and then into aqua regia solution.

The SiNWs were removed using a razor blade and transferred into a symmetric DAC with a 400 μm culet size, 45-60 μm gasket thickness, and 220 μm diameter hole. Ne was used as a pressure medium. A small ruby ball was placed in the cell to measure pressure using the ruby fluorescence method with the high temperature correction from Datchi et al.[129,154] A double membrane system was used to control the pressure.[130] During compression and decompression, the DAC was heated using a resistive heating block. A thermocouple was attached to the outside of the block to measure the temperature. Once the temperature had stabilized, the SiNWs were compressed to ∼22 GPa (such that they were completely sh-Si) and then decompressed to ∼9-10 GPa. From here, the decompression rate was carefully controlled down to ∼2-3 GPa. Two sets of experiments were performed: constant temperature (105°C) and varying decompression rate (∼5.6x10^{-4} GPa/s to ∼10 GPa/s), or constant decompression rate (∼4.2x10^{-3} GPa/s)

and temperature varied (between 70-165°C). After high pressure treatment, the gaskets (with the samples attached to them) were removed for characterisation.

Nanoindentation details

Nanoindentation was performed with a conical indenter having a 1.3 μm diameter spherical tip using a Hysitron Ti 900 Triboindenter. To allow for high temperature nanoindentation, the nanoindenter was fitted with a stage based on the design of Trenkle et al.[120] A thermocouple, that was connected to the heating block, was used to measure the temperature.

Nanoindentation was performed in ⟨100⟩ oriented dc-Si and ion-implanted a-Si. The a-Si sample was prepared using a well-established procedure (self ion-implanting Si with ions of energies 0.08, 0.5, 1.0, 1.5 and 2.0 MeV each with a fluence of 1x10^{15} ions/cm^2).[155] This resulted in a layer of a-Si that was 2 μm deep.[155] As only relaxed a-Si readily phase transforms via nanoindentation,[82] the sample was relaxed by annealing at 450°C for 30 min in Ar. This sample remained a-Si after annealing as detailed in Ref.[155] Nanoindentation with a 8 mN maximum load, 10 s loading time and unloading within 1, 10, 40 and 300 s was performed 50 times for each unloading time, on each starting material at 25°C and 105°C. [i] This maximum load was chosen such that the depth of the resulting phase transformation volume approached the diameter of the individual SiNWs. For the high temperature measurements, the tip remained in contact for an hour before each set of 50 tests and for 30 s before each test. Note that due to stage drift from the high temperature, the data obtained is not suitable for contact mechanics analysis (which was not the purpose of this study).

Characterisation

The SiNWs and nanoindentation residual impressions were characterised using XRD, SEM, Raman spectroscopy and TEM.

X-ray diffraction details

XRD was used to determine the phases present in the SiNWs under ambient conditions after being subjected to pressure. The 16 ID-B beamline of the Advanced Photon Source at Argonne National Laboratory was used.[133] A 25 keV beam was used for the ∼10 GPa/s and 0.8 GPa/s samples and a 31 keV beam was used for all other samples. The beam used a transmission geometry and had a 6x3 μm FWHM spot size. 2D diffraction patterns were collected with a Pilatus 1M detector and integrated using Dioptas.[134]

Raman Spectroscopy details

Raman Spectroscopy was used to individually determine the end phase of each indent. A Renishaw Reflex InVia Raman system, with a 532 nm laser with a ∼1 μm spot size, 2400 l/mm grating, and intensities of 1.2 mW (dc-substrate) and 0.12 mW (a-Si substrate) was

[i] Below about 150°C, a-Si is known to phase transform on loading.[155] At and above 150°C a-Si deforms via plastic flow during loading and no phase transformation occurs.[155]

used. These settings were chosen such that no significant heating of the samples occurred. Note that some of the material around the nanoindentation-modified zone overlapped with the laser spot and therefore also contributed to the Raman signal.

Electron microscopy details

SEM was performed using a FEI Varios scanning electron microscope to investigate the morphology of the compressed materials. TEM was performed using Hitachi HF3300 TEM (at ORNL) and Jeol 2100F (ANU) TEM instruments operating at 300 kV and 200 kV, respectively.

The SiNWs were prepared for TEM analysis by dispersion onto a grid. The SiNWs were removed from the gasket using a stainless steel needle and ultrasonicated in isopropanol. A micropipette was used to transfer the dispersed SiNWs onto a lacey carbon TEM grid. The samples prepared via nanoindentation were thinned to electron transparency using the *ex situ* liftout technique in a FIB.[138] A ∼150 nm layer of Pt was first deposited on a region of interest using the electron beam to protect the surface. A further ∼1.2 μm of Pt was then deposited using the ion beam. Rough milling was performed at 30 kV, 6500 nA and final thinning was performed at 5 keV, 81 pA. A micromanipulator was used to place the resulting lamellae onto a carbon coated formvar TEM grid.

5.3 SiNW results

Rate and temperature effects

Before discussing the data from this specific set of experiments, it is important to recall some of the key results from Chapters 3 and 4. In these chapters, the end phase of the SiNWs for both fast and slow decompression at ambient temperature was predominately a-Si, with trace bc8-Si and dc-Si for very slow decompression.

Figure 5.1 shows integrated XRD patterns of SiNWs that were decompressed at higher than ambient temperatures at a rate of ∼4.2x10^{-3} GPa/s (∼15 GPa/hr). The XRD pattern of the SiNWs recovered after compression at 70°C has two broad peaks (labelled with red arrows), indicating a large presence of a-Si. In addition, there are several weaker sharp peaks that correspond to dc-Si and bc8-Si, indicating trace amounts of these phases. Additional peaks marked with asterisks are also present and are likely to result from contamination from the gasket. When the temperature was increased to 105°C and 135°C, a-Si was no longer present and the SiNWs appeared to contain more bc8-Si and dc-Si. When the decompression temperature was further increased to 165°C, the amount of dc-Si present relative to bc8-Si increased. The general trend of a-Si at low temperatures, bc8-Si and dc-Si at moderate temperatures, and a higher proportion of dc-Si at the highest temperatures is similar to the results of the previous chapter where a slower ∼5.6x10^{-4}GPa/s (∼2 GPa/hr) decompression rate was used. Intriguingly, the end phase observed at 70°C for the slower decompression rate of the previous chapter (see Fig. 4.4) was much more crystalline than the almost entirely amorphous 70°C sample in this chapter. This would suggest that, like in nanoindentation,[75,156] there is a decompression rate dependence for the phase transformations in SiNWs.

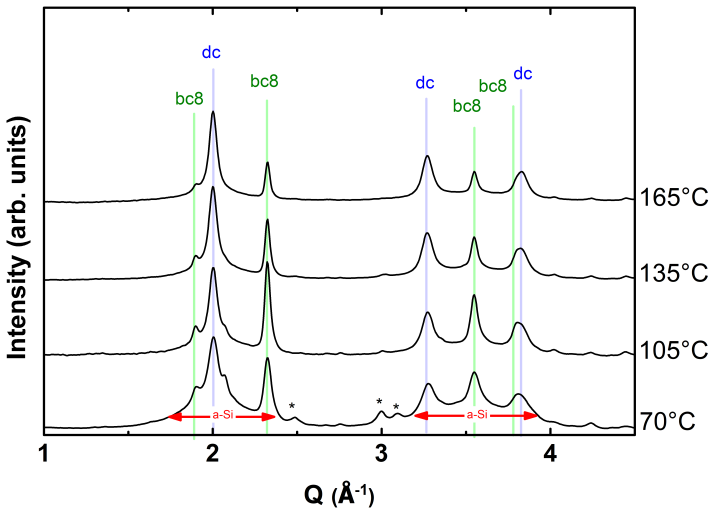

Figure 5.1: Integrated XRD patterns taken after recovery at ambient temperature of SiNWs after compression and decompression (at 4.2x10^{-3} GPa/s between 9-3 GPa) in a DAC at the indicated temperature. The asterisks mark peaks that are likely to be a result of contamination from the gasket.

The possibility of a decompression rate dependence was investigated at 105°C. XRD patterns of SiNWs decompressed at 105°C that were decompressed at different rates are shown in Fig. 5.2. For the fastest decompression rate of 10 GPa/s, a-Si is the dominant phase but traces of bc8-Si and dc-Si are also present. This is similar to the end phases formed at ambient temperature (Fig. 4.4) and at 70°C with a 4.2x10^{-3} GPa/s decompression rate (Fig. 5.1). At slower decompression rates (Fig. 5.2), larger amounts of the crystalline phases are observed. This is already apparent at a decompression rate of 0.8 GPa/s, and even more so at ∼4.2x10^{-3} GPa/s and ∼5.6x10^{-4} GPa/s. This indicates a tendency, similar to nanoindentation, for crystalline phases to form at high temperatures and under slow decompression.[78,107]

Electron microscopy of SiNWs

XRD collects data from all the SiNWs present in the ∼4x6 μm^2 x-ray beam and therefore does not provide information on the behaviour of individual SiNWs. However, TEM can be used to probe the phases present in individual SiNWs. Individual SiNWs appear to be predominately one phase after decompression, where a-Si is observed at lower temperatures/fast decompression rates, and polycrystalline bc8-Si and/or dc-Si SiNWs are observed at higher temperatures and slower decompression rates.

Figure 5.3 (a) contains an image of a SiNW before compression with a SADP in the inset. The diffraction pattern in Fig. 5.3 (a) contains only reflections from the [013] zone axis of dc-Si, indicating that the SiNW is a single crystal. Figure 5.3 (b) shows a high magnification image of this SiNW. This image shows that the SiNW has good crystal quality and a ∼2 nm thick native oxide layer (marked in black) at the edge of the SiNW.

Representative images of SiNWs that were recovered after high pressure treatment are shown in Figs. 5.4 and 5.5. A general observation for both these figures is that after the

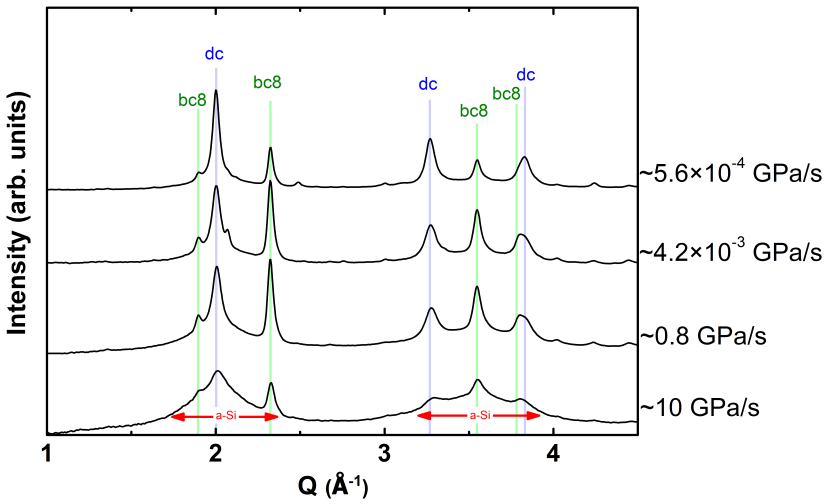

Figure 5.2: Integrated XRD patterns taken after recovery at ambient temperature of SiNWs after compression and decompression at the rates shown between 9-3 GPa in a DAC at 105°C.

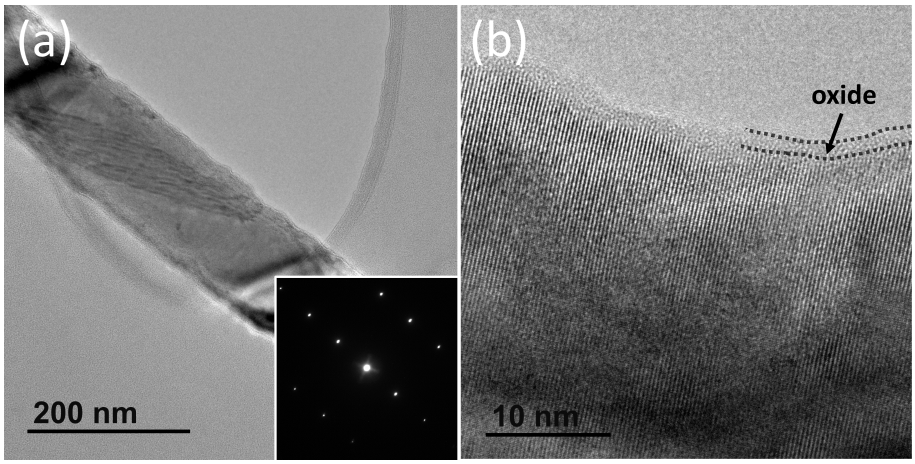

Figure 5.3: (a) A BF TEM image of a SiNW before compression with an inset SAPD. (b) a higher magnification image of the same SiNW showing the ∼2 nm thick oxide layer.

application of pressure, the SiNWs are no longer single crystalline and the new phases formed are polycrystalline and randomly oriented.

Figure 5.4 (a) contains a DF image (taken from the circled spot) of a SiNW (pressurised at 105°C and decompressed at a rate of ∼4.2x10^{-3} GPa/s) with an inset SADP. This SADP contains several spots as well as weak diffuse rings. The spots observed in this SADP correspond to dc-Si and the diffuse rings indicate the presence of some a-Si. Multiple crystallites in the SiNW are highlighted in the DF image, indicating that the SiNW is polycrystalline. A higher magnification image of this SiNW is shown in Fig. 5.4 (b). Consistent with the previous image, this image reveals multiple crystal domains within the NW. Additionally, a region that has a minimum thickness of ∼10 nm is present near and at the edge of the SiNW, as indicated with dotted lines. This region appears to be amorphous and is significantly thicker than the ∼2 nm native oxide layer of the uncompressed SiNW (Fig. 5.3). This suggests that this near-surface amorphous region is

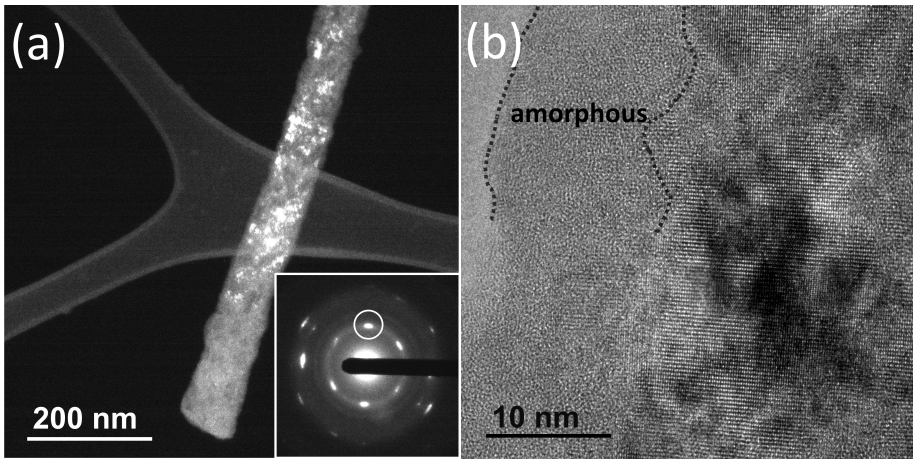

Figure 5.4: Images of a SiNW where dc-Si formed (105°C, 4.2x10^{-3} GPa/s). (a) A DF image of the SiNW taken from the circles spot in the inset SADP, (b) a higher magnification image of this SiNW. (Images courtesy of Dr David Cullen (ORNL)

not entirely composed of the surface oxide of the SiNW as it is thicker than the native oxide.

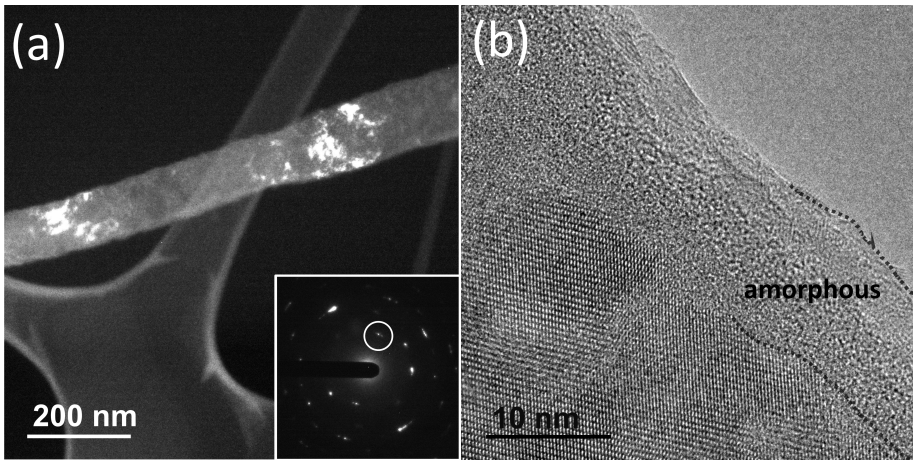

Figure 5.5: (a) A DF image (from the circled spot) of a SiNW decompressed at (105°C, 5.6x10^{-4} GPa/s) where bc8-Si formed with an inset SADP taken from the SiNW, (b) A high magnification image a different SiNW (105°C, 4.2x10^{-3} GPa/s). (Images courtesy of Dr David Cullen (ORNL)

A representative DF image of a SiNW (taken from the circled diffraction spot) where the end phase was predominately bc8-Si (pressurised at 105°C and decompressed at ∼5.6x10^{-4} GPa/s) is shown in Fig. 5.5. The inset image is of an SADP taken from this SiNW and its reflections are consistent with the bc8 phase of Si. Like the previous SiNW shown, this SiNW is also polycrystalline. Figure 5.5 (b) shows a higher magnification image of a different SiNW (pressurised at 105°C and decompressed at ∼4.2x10^{-3} GPa/s) where bc8-Si was the dominant phase formed. Like for the dc-SiNW shown in Fig. 5.4, an amorphous layer with a minimum thickness of ∼10 nm is present at the edge of this SiNW.

From these results, and Chapters 3 and 4, it is clear that SiNWs recovered after high pressure treatment are either entirely a-Si (occasionally with trace dc or bc8-Si) or are polycrystalline where the end phase is either predominately dc-Si or predominately bc8-Si. Regardless of whether dc-Si or bc8-Si is the final crystalline phase, a layer of amorphous material (mainly a-Si) near the surface of the SiNWs is present.

5.4 Nanoindentation results

Rate and Temperature effects

Like in the SiNWs, three different end phases were observed after nanoindentation of Si: dc-Si, r8/bc8-Si and a-Si. In this section, evidence for each of the end phases (from both the nanoindentation curves and Raman Spectroscopy) will be provided and the frequency of each end phase under different indentation conditions will be discussed.

The force-depth curves taken in nanoindentation are a well-established method for identifying the end phases present after nanoindentation.[1,75] Three types of force-depth curves are observed in the nanoindentation of Si: a smooth unloading curve, a pop-out event and an elbow event. Representative examples of each of these curves are shown in Fig. 5.6. Note that these three types of indentation curves were observed under many different conditions in both dc-Si and a-Si starting materials. The first type of curve contains a smooth unloading curve where no obvious features are present in the unloading portion of the curve. An example of this is shown in Fig. 5.6 (a), where this particular example shown was collected at 105°C, with a 300 s unloading time. The second type of unloading curve observed [Fig. 5.6 (b) at a temperature of 25°C and unloading in 10 s] contains a pop-out event during unloading section which in the literature is well understood to be indicative of the β-Sn-Si to r8/bc8-Si phase transformation.[75] Finally, an example of a nanoindentation curve with an elbow event, which is well known to indicate amorphisation,[1,75] is shown in Fig. 5.6 (c). This example shown was collected at 25°C with an unloading tine of 10 s.

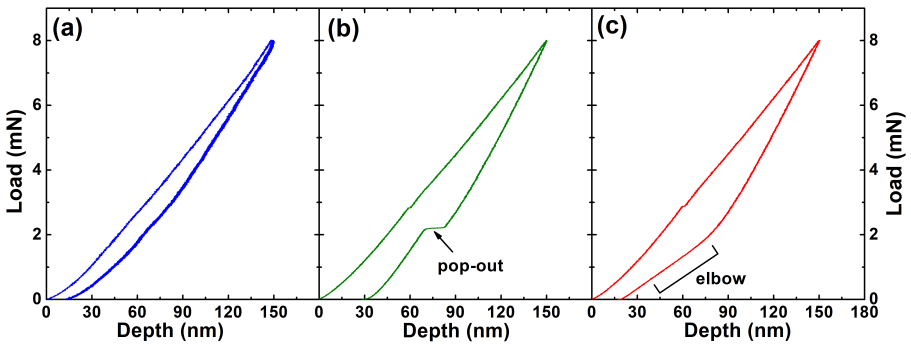

Figure 5.6: Representative force-depth curves of residual impressions from nanoindentation of (100) single crystal dc-Si (a) a smooth unloading curve (105°C, 10 s unloading time), (b) a pop-out event (25°C, 10 s unloading time), and (c) an elbow event (25°C, 10 s unloading time).

Raman spectroscopy is used to confirm the interpretation of the nanoindentation

curves. Figure 5.7 (a) shows an example Raman spectrum of an indent with a smooth unloading curve. This spectrum consists of the 532 cm^{-1} dc-Si peak and an additional small peak to the right. This small peak might suggest the presence of compressive strain in the sample as the dc-Si peak is known to shift to higher wavenumbers under high pressure.[141] It is important to note that for all Raman measurements, there is some contribution from the material surrounding the indented region since the laser spot size (∼1 μm in diameter) is larger than the indented region (∼800 nm in diameter). An example Raman spectrum from a pop-out curve is provided in Fig. 5.7 (b). In addition to the dc-Si peak from the surrounding material, several other peaks (indicated with a bracket), corresponding to the r8/bc8-Si phase,[77] are present. Note that in nanoindentation, residual strain present after nanoindentation stabilizes the r8-Si phase, and therefore a mixture of around 70% r8-Si and 30% bc8-Si is observed after nanoindentation.[77] A Raman spectrum for an elbow event is shown in Fig. 5.7 (c). In this spectrum, several broad peaks, indicated by a bracket, are present. These peaks indicate the presence of a-Si, consistent with elbow behaviour reported in the literature.[75]

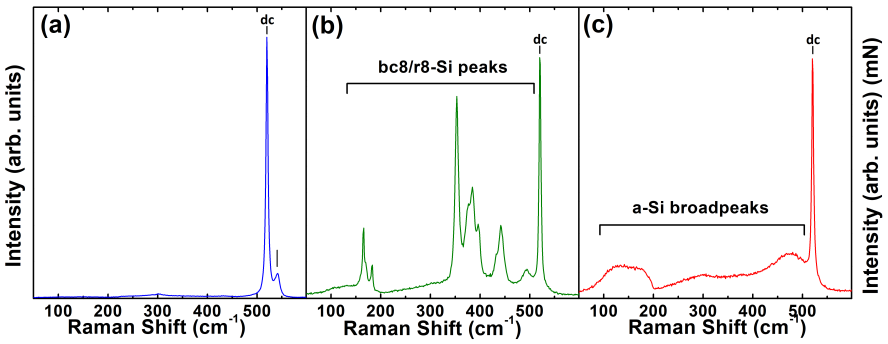

Figure 5.7: Representative Raman spectra of residual impressions from nanoindentation of (100) single crystal dc-Si (a) a smooth unloading curve (105°C, 10 s unloading time), (b) a pop-out event (25°C, 10 s unloading time), and (c) an elbow event (25°C, 10 s unloading time).

Now that the possible end phases have been identified, the occurrence of each end phase under different unloading conditions can be examined. Figure 5.8 shows the number of indents with a particular end phase present after nanoindentation of dc-Si and a-Si starting materials under various conditions. The unloading times (note that all indents had the same loading time) for the indents are indicated to the left. Figure 5.8 (a) shows the end phases observed for indentation performed on dc-Si at 25°C. For rapid, 1 s unloading, 100% of the indents had an a-Si end phase. When the unloading time was increased to 10 s, most of the indents were a-Si; however, 7 indents contained the r8/bc8-Si end phase. Further increasing the unloading time to 40 s, did not change the a-Si and crystalline end phase portions significantly. However, when the unloading time was increased further to 300 s, the formation of r8/bc8-Si was further enhanced to ∼25% of all indents with the remain indents containing the a-Si end phase.

The frequency of each end phase observed when indenting dc-Si at 105°C at different unloading times is shown in Fig. 5.8 (b). In contrast to the equivalent indents at 25°C, unloading for 1 s at 105°C does not lead to the a-Si end phase 100% of the time. Instead, most indents contained a-Si, and 9 of the indents contained r8/bc8-Si. When a 10 s un-

loading time was used, the proportion of r8/bc8-Si indents significantly increased. When the unloading time was increased further to 40 s, the number of indents with a r8/bc8-Si end phase decreased compared with the 10 s unloading time. This observation may seem surprising and will therefore be discussed in more detail in section 5.5. It should be noted that the Raman spectrum of indents with this unloading condition contained a small peak similar to the compressive strain peak observed in the Raman spectrum of indents with a smooth unloading curve (Fig. 5.7. When the unloading time was increased to 300 s, only the dc-Si end phase was observed. Since all indents at 105°C had the same loading conditions, it can be safely assumed that before unloading a phase transformation to β-Sn-Si had occurred in all cases. Thus, it would appear that for the longest unloading time, β-Sn-Si formed and phase transformed back to dc-Si during unloading.

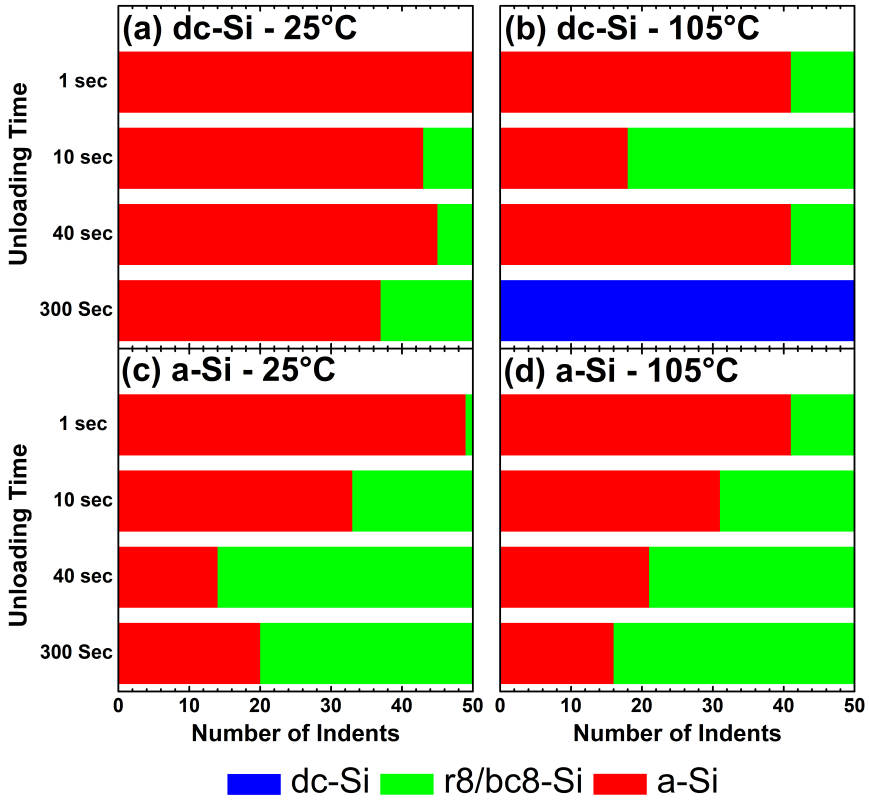

Figure 5.8: The number of indents with a-Si, r8/bc8-Si or dc-Si end phase for 10 s loading time, and 1, 10, 40 and 300 s unloading times under the following conditions, (a) 25°C, dc-Si starting material, (b) 105°C, dc-Si starting material, (c) 25°C, a-Si starting material, and (d) 105°C, a-Si starting material.

Figure 5.8 (c) and (d) shows the number of indents containing each end phase for the a-Si starting material. At 25°C [Fig. 5.8 (c)], the end phase of almost all indents with a 1 s loading time, was found to be a-Si. Similar to the dc-Si starting material at the same temperature, a higher fraction of r8/bc8 in residual indents was generally observed for increasing decompression times. Additionally, more r8/bc8-Si was observed to form in the a-Si starting material when compared with the dc-Si starting material, suggesting that r8/bc8-Si forms more easily when using an a-Si starting material.

When the nanoindentation temperature was increased to 105°C, the only end phases observed for all unloading times were r8/bc8-Si and a-Si.[ii] In general, it was observed that when the unloading time was increased, the proportion of indents with the r8/bc8-Si end phase also increased. For some indents with 40 and 300 s unloading times, trace dc-Si was observed. The end phases obtained when indenting the a-Si starting material at 105°C with an unloading time of 300 s are clearly different from indenting the dc-Si starting material under the same conditions, where 100% dc-Si end phase was observed.

Electron Microscopy

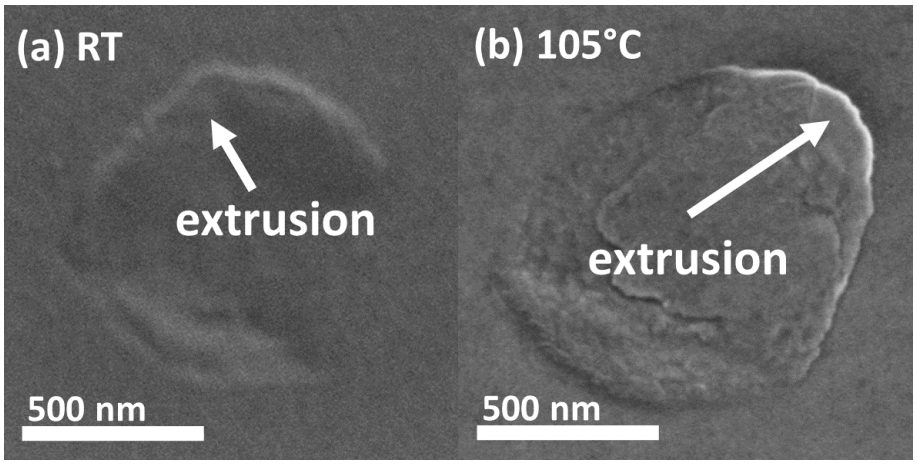

Figure 5.9: SEM images of residual impressions from nanoindentation of a dc-Si substrate with a 300 s unloading time at (a) 25°C, (b) 105°C.

SEM images of regions of dc-Si modified, at 25°C and 105°C with a 300 s unloading time, by nanoindentation are shown in Fig. 5.9. Regardless of the temperature of nanoindentation, all indents appeared to be similar in size, with a diameter of ∼850 nm. Additionally, material that appeared to be extruded from under the tip was also observed for all indents. This extrusion is indicated with arrows in Fig. 5.9. It has been previously established that extrusion of material from under the tip is a signature for phase transformation to the ductile β-Sn-Si metallic phase.[88] Therefore, this observation of extrusion suggests that all indents phase transformed to β-Sn-Si on loading. This observation further supports an argument for a direct β-Sn-Si to dc-Si phase transformation occurring under some conditions.

Figure 5.10 (a) shows a BF image (on the [110] zone axis of the dc-Si substrate) of an indent in dc-Si that was performed at 25°C with a 10 s unloading time. In this image there is a clear lighter region, marked with a dotted line, that is ∼150 nm in depth, and is therefore comparable with the diameter of the SiNWs studied in this chapter and previous chapters. The inset SAPD is taken from entirely within this region, and the reflections contained within this SADP are consistent with polycrystalline r8/bc8-Si, indicating that

[ii]Note that from prior literature, relaxed a-Si phase transforms at 100°C (with pressure induced a-Si being reported as the end phase for fast unloading) but deforms via plastic flow at 150°C.[155] It would therefore be expected that at 105°C, phase transformation to β-Sn-Si occurs.

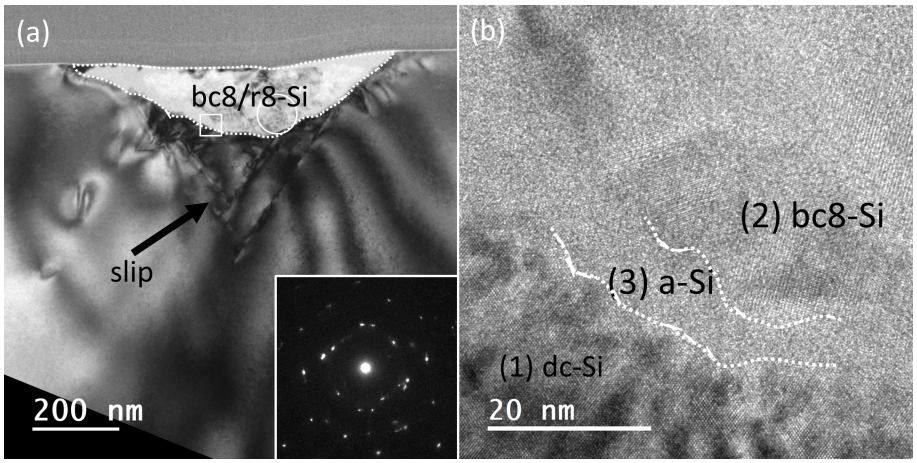

Figure 5.10: Images of an indent formed at 25°C with a 10 s loading time with a pop-out in the unloading curve (formed at 25°C and 40 s unloading time). (a) a BF image with an inset SADP taken from the phase transformation zone, (b) a higher magnification image of the region marked with a white square in (a).

this region has phase transformed. The region underneath this phase transformation zone contains some planar defects, previously reported to be slip.[76] Some of these defects extend up to the bottom of the phase transformation zone. A higher magnification image of the region indicated by a white box, at the bottom of the phase transformation zone is shown in Fig. 5.10 (b). This image contains several distinct regions, each of which has been labelled. These are the (1) crystalline dc-Si surrounding material, (2) bc8-Si crystallites within the indent, and (3) a region of a-Si about 10 nm in thickness between (1) and (2).

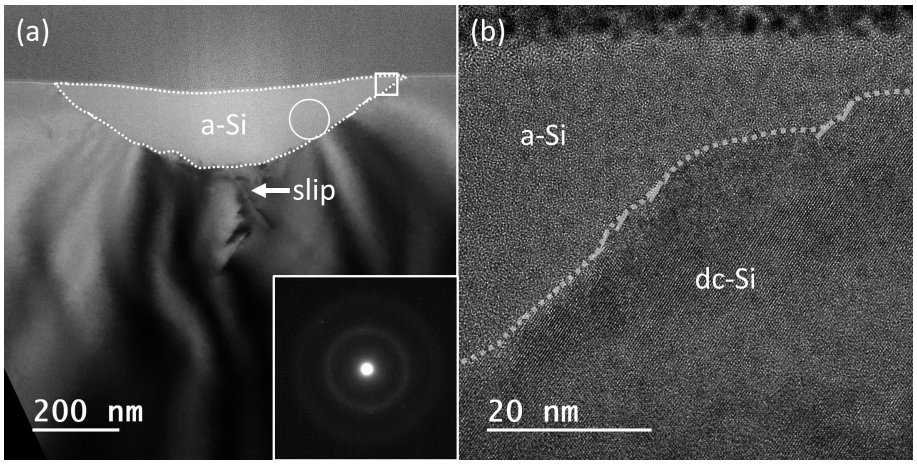

Figure 5.11: Images of an indent with an elbow in the unloading curve (formed at 25°C and 40 s unloading time). (a) a BF image with an inset SADP taken from the circle in the phase transformation zone, (b) a higher magnification image of the region marked with a white square.

Representative TEM images of an indent with elbow unloading curve are shown in Fig. 5.11. This indent was performed at 25°C with a 40 s unloading time. A low magnification image of this indent is shown in Fig. 5.11 (a). Here there is a clear region, outlined with

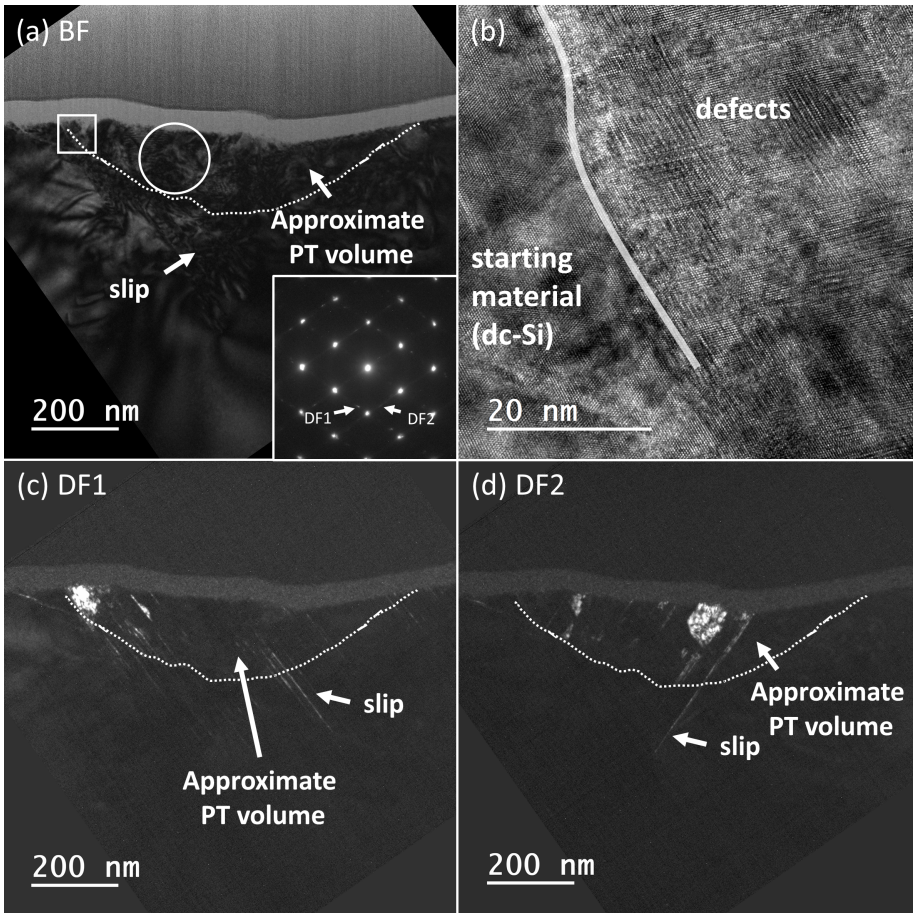

Figure 5.12: Images of an indent with a smooth unloading curve (formed at 105°C and 300 s unloading time). (a) a BF image with an inset SADP taken from the region circled in white, (b) a higher magnification image of the region marked with a white square, (c) and (d) DF images taken from the spots in the SADP labelled DF1 and DF2, respectively. The dotted outline from the phase transformation zone in Fig. 5.11 is superimposed on (a), (c) and (d) to indicate the approximate phase transformation zone.

a dotted white line, that is lighter than the rest of the image. This region is ∼160 nm in depth. When a SADP of this region was taken (shown in the inset), diffuse rings were observed, corresponding to a-Si. This indicates that this region has phase transformed, with a-Si being the final phase, consistent with the nanoindentation curve and Raman spectrum. In addition to the phase transformation zone, some slip (marked with an arrow) is observed under the phase transformed zone. A high magnification image of the white square is shown in Fig. 5.11 (b). This image shows that there is a rough interface between the crystalline substrate and amorphous phase within the phase transformed region.

TEM images of an indent where a smooth unloading curve was observed (at 105°C with a 300 s unloading time) are shown in Fig. 5.12. A BF of this indent is shown in Fig. 5.12 (a). To allow for a comparison with previous indents shown, an outline of the phase transformation zone from the a-Si indent in Fig. 5.11 is superimposed on this image, indicating where phase transformation would be expected. In this region, highly defective material is observed. A SADP taken from the encircled region is inset into this panel. This

reveals basically single crystalline dc-Si with significant twinning, as indicated by the weak diffraction spots observed in one third increments between the main dc-Si diffraction spots (on the [110] zone axis in this case). It will later be argued that some of the defects present are due to phase transformation from β-Sn-Si to dc-Si via defective epitaxial regrowth during unloading. A higher magnification image taken of the region marked with a white square, near the top edge of the defective region is shown in Fig. 5.12 (b). This image contains two distinct regions, perfect single crystal starting material, and twinned and defective single crystal. Unlike for the r8/bc8-Si indent previously shown, there is no a-Si region between what would be the phase transformation zone and the starting material that did not phase transform. Figure 5.12 (c) and (d) show DF images of the diffraction spots in the SADP labelled DF1 and DF2, respectively. Both these diffraction spots are due to twinning, and the DF images of these diffraction spots indicate that the regions of twinning occur within the phase transformation zone. These DF images also highlight slip defects, some which are labelled with arrow. These slip defects originate below where the phase transformation region is expected, and some of them extend to the surface of the sample.

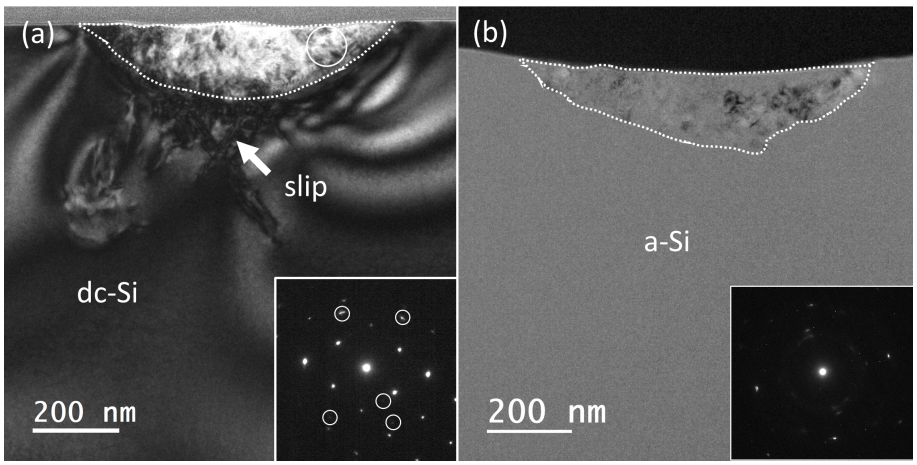

Figure 5.13: BF images with inset SAPDs of indents with (a) dc-Si substrate at 105°C and 40 s unloading time, the circled spots in the SADP are not from the [110] zone axis and are believed to be defect related, and (b) a-Si substrate at 105°C and 300 s unloading time.

Finally, Fig. 5.13 contains TEM images of indents made with a 40 s unloading time at 105°C into dc-Si with an elbow in the unloading curve and a-Si signal in the Raman spectrum [Fig. 5.13 (a)], and with a 300 s unloading time at 105°C into a-Si [Fig. 5.13 (b)]. These conditions are of interest because the former appears not to follow the trend of longer unloading times resulting in more r8/bc8 and the latter resulted in a r8/bc8-Si end phase rather than the dc-Si end phase as obtained under similar conditions when using a dc-Si starting material. A BF image in Fig. 5.13 (a) shows a region, highlighted by a dotted line, that appears to have phase transformed. Like all previous indents, there is a region of slip defects underneath (indicated with a white arrow). A SADP entirely from the phase transformation zone shows the presence of dc-Si ([110] zone axis) as well as some extra spots circled in white which are believed to be related to some sort of defect. This suggests that unlike the majority of indents at 25°C where either a-Si or r8/bc8-Si

were the end phases, the phase transformed region has possibly partially transformed back to dc-Si. This occurred by epitaxial growth from with the surrounding material that did not phase transform acting as a seed. An BF image of an indent into a-Si with a 300 s unloading time at 105°C where r8/bc8-Si was observed to form (according to the Raman spectrum and nanoindentation curve) is shown in Fig. 5.13 (b). This image shows a distinct crystalline region near the surface of the indented region. An SADP from this region is inset in this image and the reflections are consistent with bc8-Si as is expected if there is no dc-Si seed from which to grow a dc-Si end phase.

5.5 Discussion

After presenting the results of both the nanoindentation of Si and DAC compression of SiNWs, it is now possible to make some comments on their similarities and differences. Table 5.1 summarizes the key observations for SiNWs and nanoindentation. A summary of the behaviour from this study, including results from previous chapters, is presented in this table.

Table 5.1: Summary of the final phases observed for SiNWs and nanoindented bulk-Si under different conditions from this work.

Conditions	**Nanoindentation**	**SiNWs**
Ambient temperature (rapid decompression)	Only a-Si	Only a-Si
Ambient temperature (slow decompression)	Indents are either a-Si or r8/bc8-Si with few that are a mixture.	Most SiNWs are entirely a-Si, some bc8-Si or dc-Si in a few SiNWs
105°C (rapid decompression)	either a-Si or r8/bc8-Si with few that are a mixture.	a-Si (trace bc8-Si and/or dc-Si)
105°C (slow decompression)	dc starting material: only dc-Si a-Si starting material: indents either contain r8/bc8-Si or are entirely a-Si	predominately bc8-Si or dc-Si (with a few that are mixed phase.)

For both nanoindentation and SiNWs, rapid decompression from the β-Sn-Si structure [iii] at ambient temperature leads to a-Si being the dominant end phase. If instead, slow decompression at ambient temperature is used, for both nanoindentation and SiNWs, a-Si is the dominant phase but r8/bc8-Si forms in some cases. Under these conditions, about 20-25% of indents are found to be entirely bc8/r8-Si, and some SiNWs contain a significant fraction of bc8-Si. This behaviour is similar to the behaviour observed for rapid decompression at 105°C in both SiNWs and nanoindentation, where a-Si is also the dominant end phase, with crystalline r8/bc8-Si and dc-Si occasionally forming. Individual indents were found to be either entirely a-Si or almost entirely r8/bc8-Si.

[iii] Note the β-Sn-Si in the SiNWs forms from the decompression of sh-Si whilst in nanoindentation, β-Sn-Si forms directly from dc-Si on compression.[72] Although this difference in the formation pathway of β-Sn-Si is not likely to affect the final phases formed, there might be some subtle differences in the texture and crystallite size.

Finally, the behaviour of SiNWs and indented Si during slow decompression at 105°C is more complicated. Here, the behaviour is very dependent on the starting material. For the SiNWs, the final phase observed is a mixture of dc-Si and bc8-Si. For nanoindentation of dc-Si, dc-Si was the only end phase observed. This is likely to have formed from defective epitaxial growth from the surrounding material. In contrast to nanoindentation of dc-Si, nanoindentation of a-Si resulted in increased r8/bc8-Si formation as the unloading time was increased, with only traces of dc-Si observed. Individual NWs were observed to be mostly either bc8-Si or dc-Si with some a-Si close to the SiNW surface, but occasionally mixed bc8/dc-Si NWs were observed. Individual indents with a dc-Si starting material were found to all contain epitaxial but defective dc-Si. For the a-Si starting material, the end phase was found to be either entirely a-Si or entirely r8/bc8-Si.

It is clear that there are a few general trends for both SiNWs and nanoindentation. When temperature and decompression time are increased, the fraction of crystalline end phases increased. The maximum proportion of dc-Si formed in SiNWs at the highest temperature and slowest decompression rate for both SiNWs (165°C, 5.6x10^{-4} GPa/s) and nanoindentation (105°C, 300 s unloading time). Overall, the agreement between the small phase transformation volume nanoindentation behaviour and the behaviour of SiNWs under decompression is remarkably similar. However, there are some subtle differences that are addressed below.

The nucleation of the a-Si, bc8-Si and dc-Si end phases observed to form directly from β-Sn-Si in both nanoindentation and for the SiNWs will be discussed first. As pressure is decreased below 9.5 GPa, β-Sn-Si is no longer the thermodynamically favoured phase.[11] If there is insufficient energy or time for the lowest free energy crystalline phases to form (at low temperatures, or fast decompression rates) β-Sn-Si becomes so unstable that phase transformation to a-Si occurs. This was observed to occur at ∼5 GPa at ambient temperature (see Chapter 3). At higher temperatures and slower decompression rates, r8-Si (which phase transforms to bc8-Si) or dc-Si was observed to form. Given that bc8-Si is the end phase in bulk-Si at the temperatures studied,[102] it is thus unsurprising that bc8-Si forms under these conditions.

The formation of the dc-Si end phase at the higher temperatures and slower decompression rates differs between SiNWs and nanoindentation, and is therefore more complicated than the other end phases. For the SiNWs, this end phase consists of randomly oriented polycrystalline material. In nanoindentation of dc-Si, the dc-Si end phase appears single crystalline but defective, suggesting formation by growth from the surrounding crystalline material. This growth is somewhat comparable to that in solid phase epitaxy whereas the dc-Si formation in the SiNWs is analogous to random nucleation and growth as is observed when a layer of a-Si on SiO_2 crystallises.[157] The relevance of this analogy will become more apparent in the next few paragraphs.

The activation energies involved in each of the phase transformations on decompression (which are summarised in Table 5.2) will now be examined.The activation energies of formation of r8-Si and dc-Si from β-Sn-Si (presumably via nucleation and growth) at 8 GPa were calculated to be ∼0.15 and ∼0.22 eV, respectively.[28] Thus, despite dc-Si being the thermodynamically lowest free energy phase at this pressure, r8-Si has a lower energy barrier to formation and hence it forms more readily at lower and intermediate temperatures. At higher temperatures, more thermal energy is available and this allows

Table 5.2: The activation energies of various phase transfigurations in Si.

Phase Transformation	Activation Energy (eV)
β-Sn to dc (8 GPa)	0.22 eV[28]
β-Sn to r8 (8 GPa)	0.15[28]
a-Si to dc (SPE)	2.7[157]
a-Si to dc (RNG)	4.0[157]

for dc-Si to form directly from β-Sn-Si. Intriguingly, nanoindentation at 105°C with a 300 s unloading time resulted in 100% dc-Si end phase. This unloading (decompression) time was significantly shorter decompression of the SiNWs at 105°C at the two slowest decompression rates where bc8-Si formed. When considering these decompression time in light of the activation energies of solid phase epitaxy (2.7 eV), and random nucleation and growth (4.0 eV),[157] it would seem likely that the activation energy for the β-Sn-Si to dc-Si transformation is much lower when growing from the surrounding material (like in solid phase epitaxy), assuming phase transformation occurs on loading, compared with random nucleation in SiNWs (like in random nucleation and growth). Therefore, the dc-Si end phase is more readily formed during nanoindentation. This is further supported by the fact that when an a-Si starting material was used, dc-Si was only observed in trace amounts as dc-Si could only form via random nucleation and growth due to there being no seed dc-Si.

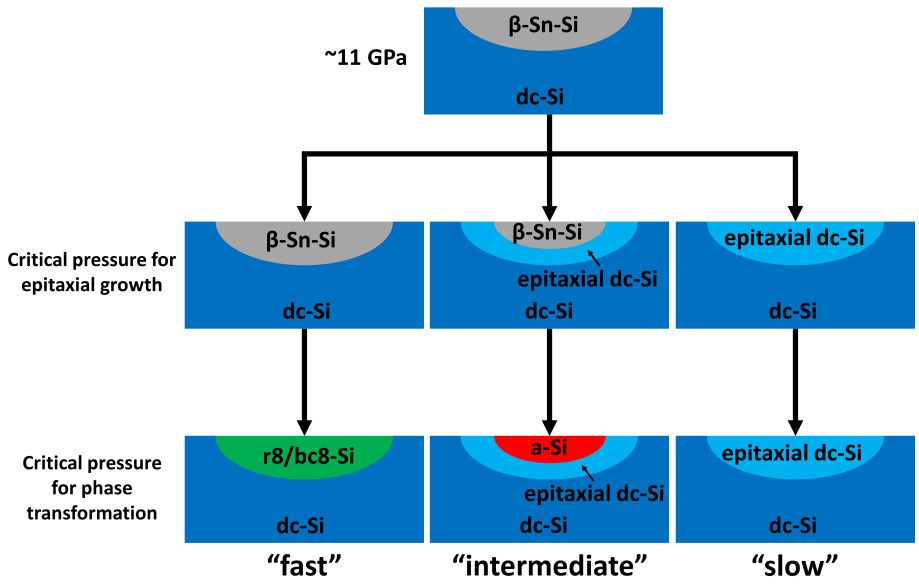

Figure 5.14: A schematic diagram showing the phase transformations when unloading the phase transformed zone formed during nanoindentation of dc-Si at 105°C. In this instance "Fast" refers to an unloading time of 1-10 s, "intermediate" refers to an unloading time of 40 s, and "slow" refers to an unloading time of 300 s.

In terms of the formation of dc-Si via epitaxial growth. It is reported that the solid phase epitaxy growth rate increases exponentially with pressure and also temperature[150–152] This would suggest that during nanoindentation, dc-Si would initially grow

quickly whilst under high pressure and slow down as pressure is decreased during unloading. Figure 5.14 schematically shows how this might affect the end phases after under different unloading conditions at 105°C. For fast unloading, 1-10 s, the pressure within the phased transformed region quickly drops below the regime where epitaxial growth occurs rapidly. This allows the β-Sn-Si to remain until the critical pressure for phase transformations to either r8/bc8-Si or a-Si is reached. For slow unloading, 300 s, decompression is substantially slower, to allow for dc-Si to epitaxially grow into the full phase transformation volume. At an intermediate 40 s unloading time, dc-Si would grow off the surrounding material, but as pressure was decreased, the rate of dc-Si growth would decrease. Once the critical pressure for phase transformations was reached, the remaining β-Sn-Si region, closer to the surface, phase transforms to either r8/Si-Si or a-Si. However, the initial growth of dc-Si reduced the size of the remaining β-Sn-Si volume, making nucleation of r8/bc8-Si more difficult, thus favouring a-Si. This would therefore explain the anomalous high fraction of the a-Si end phase observed when nanoindenting dc-Si at 105°C with a 40 s unloading time.

Another detail regarding epitaxial-like regrowth in nanoindentation is the defective nature of the dc-Si end phase formed via nanoindentation. The TEM of the dc-Si end phase showed evidence of two types of planar defects: slip and twinning. It is understood that slip nucleates underneath the phase transformation.[76] When β-Sn-Si forms over a slip defect, the formation of the new phase will essentially "erase" the slip in the phase transformation zone. During solid phase epitaxy, defects such as slip are known to propagate within a growing crystal.[158] A similar phenomenon might occur when dc-Si forms from β-Sn-Si in nanoindentation, allowing the slip defects at the dc-Si/β-Sn-Si boundary of the phase transformation zone to grow with the epitaxially-grown dc-Si, reaching the surface in some cases. Twinning was observed within what appears to be the phase transformation volume. This twinning might be a result of defective epitaxy in some orientations. Solid phase epitaxial growth of dc-Si is also directionally dependent where $\langle 100 \rangle$ epitaxy is faster than $\langle 110 \rangle$ epitaxy, which is faster than $\langle 111 \rangle$ epitaxy.[159] Indeed, epitaxy of Si in the $\langle 111 \rangle$ direction is known to be more defective than other directions with twinning always occurring.[159] As the phase transformation is approximately a semicircle in shape, epitaxial regrowth would be expected from multiple directions. Some of the regrowth might be in the $\langle 111 \rangle$ direction, resulting in twinning in some regions of the phase transformation zone. Regrowth in the $\langle 100 \rangle$ direction should occur from the bottom of the indent up. In solid phase epitaxy, the $\langle 100 \rangle$ direction is fast and it is less likely for defects to form during growth.[159] This could explain the absence of twinning in some regions of the phase transformation volume. This directional dependence of solid phase epitaxial regrowth might cause slightly different phase transformation behaviour when indenting samples with different orientations.

Another issue for discussion is the effect of confinement and pressure gradients on the phase transformation behaviour of SiNWs and nanoindentation. Each of the SiNWs experience relatively uniform pressure as a result of a hydrostatic Ne pressure medium. This pressure medium is quite soft with a bulk modulus of 0.74 GPa,[160] which should allow for the SiNWs to expand and contract as pressure changes. Indeed, there are significant density changes that occur during phase transformations. For example dc-Si undergoes a 22% decrease in volume when it phase transforms to β-Sn-Si, and there is a $\sim$10% increase

in volume when β-Sn-Si phase transforms to r8-Si.[5,6,26] In the case of nanoindentation, the phase transformed material is confined between the hard diamond tip and the underlying substrate. This confinement may lead to suppression of phase transformation to a less dense phase. For example, the "pop-out" event observed on unloading (see Fig. 5.6), signals a sudden change in density, which is possibly a result of such confinement making the change to a lower density material difficult. The phase transformation volume in nanoindentation is also under a high pressure gradient meaning that the point of critical pressure for phase transformation (i.e. β-Sn-Si to r8/bc8-Si) will move progressively from the deeper extremity of the phase transformed zone to the surface during unloading. For the β-Sn-Si to dc-Si transformation this should aid the epitaxial process at 105°C as the β-Sn-Si/dc-Si interface will reach this pressure first, mirroring thermal solid phase epitaxy-like epitaxial growth. For lower temperatures/faster unloading, the pressure gradient effects could result in the outer regions of the phase transformation zone to decrease in pressure before nucleation of r8-Si can occur, causing them to phase transform into a-Si as the initial pressure decrease is faster than later stages of unloading. This would explain the region of a-Si between the dc-Si substrate and the bc8-Si crystals observed in TEM. The work by Ruffell et al.[99] also supports this behaviour by suggesting that nucleation of r8/bc8-Si occurs away from the edge of the phase transformed region. Such confinement and pressure gradient issues are not relevant for SiNWs in a DAC due to the hydrostatic and compliant pressure medium surrounding the SiNWs, as was discussed earlier.

Nucleation does not appear to occur at the surface of the SiNWs when bc8-Si and dc-Si end phases form (see Fig. 5.4 and 5.5). This may initially seem surprising as nucleation is usually favoured at free surfaces.[161] However, the oxide layer that is present on the surface of the SiNW might suppress the nucleation of crystalline phases. This could be due to one of many different reasons. For example; surface energy considerations may favour wetting of the oxide interface by β-Sn-Si over nucleation of new crystalline phases, or atomic positions in the oxide-Si interface may be incompatible with the atomic positions of the r8-Si phase. At all temperatures and decompression rates, the bc8-Si and dc-Si phases formed are polycrystalline, suggesting that nucleation, despite being suppressed, dominates growth. However, at higher temperatures, the crystallites formed are larger and are able to grow closer to the oxide layer.

Finally, the phase transformations in this study occurred in very small volumes. Given the results of the previous chapters, where it has been shown that the phase transformation behaviour of SiNWs is influenced by their size, it is not surprising that low load nanoindentation of Si is also influenced by size effects. In nanoindentation, there are few studies that directly investigated the influence of size on the end phase observed. However some information of the size dependence of the phase transformation volume can be inferred from the current literature. For example, Zarudi et al.[80] kept the loading and unloading times constant and changed the force applied to a 5 μm radius spherical tip, effectively varying the phase transformation volume. For smaller phase transformation volumes (95-180 nm deep), a-Si was observed. Intermediate phase transformation volumes (270-500 nm depth) contained r8/bc8-Si and a-Si. For the largest volumes, (700-800 nm depth) r8/bc8-Si formed in almost all indents. Furthermore, a study using a Berkovich tip, whilst keeping the unloading displacement rate constant, observed a-Si in indents with lower phase transformation volumes.[162] Additionally, a-Si formed during nanoindentation

was previously reported to usually form at lower pressures than r8/bc8-Si,[162] similar to the case in SiNWs. When nanoindentation conditions are chosen (high loads and slow unloading) such that large phase transformation volumes are formed that approach bulk-Si in size, 100% phase transformation to r8/bc8-Si can occur just like for bulk-Si in a DAC. For example, a 21.5 μm diameter tip with a 700 mN load and 30 s unloading time, or 500 mN loading with a 150 s unloading time, were found to give 100% r8/bc8-Si.[54] These conditions yielded indent with a phase transformation volume that was 650 nm deep and greater than 20 μm^3 in volume.[54,114]

The effect of size volume of the phase transformed zone) is mostly due to the suppression of nucleation of crystalline phases, particularly at ambient temperature. As established in Chapter 3, decompressing at a higher temperature makes nucleation of the crystalline end phases easier. However, when comparing with the phases nucleation in bulk-Si in a DAC, it is quite apparent that size still affects the phases transformation behaviour. At 105°C bc8-Si was the final phase for bulk-Si, whilst in SiNWs, bc8-Si and dc-Si were both reported as final phases, consistent with the results of this study for slow decompression. As bc8-Si is difficult to nucleate due to the small volume of the phase transformed material, this may explain how the lowest free energy phase, dc-Si, can form directly from β-Sn-Si when enough energy is available to overcome the energy barrier to formation.

5.6 Conclusions

In this chapter, the phase transformation behaviour of small volumes of Si was investigated using two different techniques: DAC compression of SiNWs and nanoindentation of dc-Si and a-Si starting materials. In general, the end phases formed were remarkably similar for both SiNWs and nanoindentation, with the size of the phase transformation volume being equally important in determining the end phase. It was found that at ambient temperature, the SiNWs and indents had similar phase transformation behaviour, with a-Si being the only phase after fast decompression and the dominant phase after slow decompression. When the temperature was raised to 105°C, fast decompression led to similar behaviour to slow decompression at ambient temperature. On the other hand, slow decompression at 105°C was more complicated with dc-Si and bc8-Si being the end phase for SiNWs; epitaxial dc-Si for indents into dc-Si; and r8/bc8-Si and a-Si for indents into a-Si.

Chapter 6

Size and temperature effects on the phase transformations of germanium

In the previous chapters, it was established that the pressure induced phase transformations of Si have a size, temperature and decompression rate dependence. A combination of these three factors influences the resulting end phases. As Si and Ge are elements with similar properties and phase transformation behaviours, it is also interesting to determine the effect of size, temperature and decompression rate for Ge. Thus, in this chapter, the phase transformation behaviour of small volumes of Ge will be examined.

6.1 Introduction

Si and Ge belong to the same group in the periodic table. These elements have similar properties and phase transformation behaviour under high pressure. As detailed from previous chapters, the phase transformations in Si via both DACs and nanoindentation are affected by both size and temperature. This chapter explores similar parameters for Ge but in less detail.

The high pressure phase transformation behaviour of Ge at the nanoscale is not currently well known. One study reported that very small ∼5 nm Ge nanoparticles phase transform to a metallic amorphous phase on compression.[111] Other work found that nanocrystalline dc-Ge of 13-100 nm in size displayed a higher threshold for the dc-Ge to β-Sn-Ge phase transformation on compression when compared with bulk-Ge.[112] A study of ∼50 nm diameter GeNWs under high pressure reported that there was a similar onset of the dc-Ge to β-Sn-Ge phase transformation to bulk-Ge but the phase transformation took longer to complete.[113] That study also reported the presence of dc-Ge after decompression from the β-Sn-Ge phase but did not discuss the decompression behaviour in any detail.

In terms of the phase transformation behaviour reported during the nanoindentation of Ge, the situation is complicated. When using spherical tips, the main deformation mechanism reported is deformation via the nucleation of defects such as slip and twinning.[86,87] This process is believed to reduce the magnitude of pressure underneath the indentation tip such that the critical pressure required for the formation of β-Sn-Ge is not reached and thus phase transformation is often not observed.[86] When a-Ge is used as a starting material and there are no crystalline planes to promote slip and the motion of crystalline defects, phase transformation has been reported with dc-Ge and r8-Ge

both being possible end phases (note that r8-Ge quickly phase transforms to hd-Ge at ambient temperature within days).[24,92,93] Phase transformation in dc-Ge has only been observed under so-called extreme conditions such as very fast loading rates, high loads and very sharp tips.[87,89,90] Whilst Si is known to phase transform via nanoindentation at room temperature, similar formation of defects to those in dc-Ge has been reported in Si at temperatures above 150°C.[107] Thus, the effect of reducing the temperature of nanoindentation of Ge will also be explored in this chapter.

6.2 Compression of Ge Nanowires

The high pressure phase transformation behaviour of GeNWs at ambient temperatures was investigated. Here GeNWs were compressed in a DAC and studied *in situ* under high pressure at ambient temperature using both XRD and Raman spectroscopy.

6.2.1 Method

The GeNWs were grown using the vapour liquid solid method using a hot walled chemical vapour deposition reactor. A 2 nm Au layer was sputtered on a Si wafer as the catalyst. The sample was then heated in a quartz tube to 340°C with 2% Germane gas diluted in a mixture of He and H_2 flowing through the tube. The flow rate for both He and H_2 was 100 sccm. Once the initial nucleation of the GeNWs had occurred, the temperature was lowered to 300°C and the GeNWs were allowed to grow for 60 min. These GeNWs were 40-60 nm in diameter and 8 μm in length. The growth was performed by Dr Clemens Zeiner (TUWien). More details of the growth process can be found in Ref.[163].

The GeNWs were removed from their substrate using a stainless steel razor blade and placed in a DAC using a stainless steel needle. The DAC had a 400 μm culet size, and a stainless steel gasket preindented to ∼50 μm in thickness. A 200-250 μm diameter hole was drilled into the gasket. A total of four different cells were loaded. Either Ne or a 4:1 mixture of methanol and ethanol was used as a pressure medium. Pressure was measured using the ruby fluorescence method. The pressure in each cell was incrementally increased to 17 GPa, and then incrementally decreased to ambient temperature. At various pressures, the structure of the GeNWs inside the cell was probed using either Raman Spectroscopy or XRD. Raman spectroscopy was performed *in situ* using a Renishaw Reflew inVia Raman system using a 532 nm laser. The power of the laser was ∼2.1 mW on compression and decompression to 8.5 GPa and ∼0.2 mW on decompression below 8.5 GPa with a spot size of ∼2.6 μm, and a 2400 l/mm grating. *In situ* XRD was performed using the 16-ID-B beamline at HPCAT, Argonne National Laboratory. The spot size was ∼6x3 μm FWHM and energies of 25 keV and 31 keV were used. A Pilatus 1-M-F detector was used and the resulting powder diffraction patterns were integrated using Dioptas.

6.2.2 High pressure compression of germanium nanowires

Figure 6.1 shows (a) Raman spectra and (b) integrated powder diffraction patterns of GeNWs during compression. The Raman data will be discussed first. Initially, the GeNWs

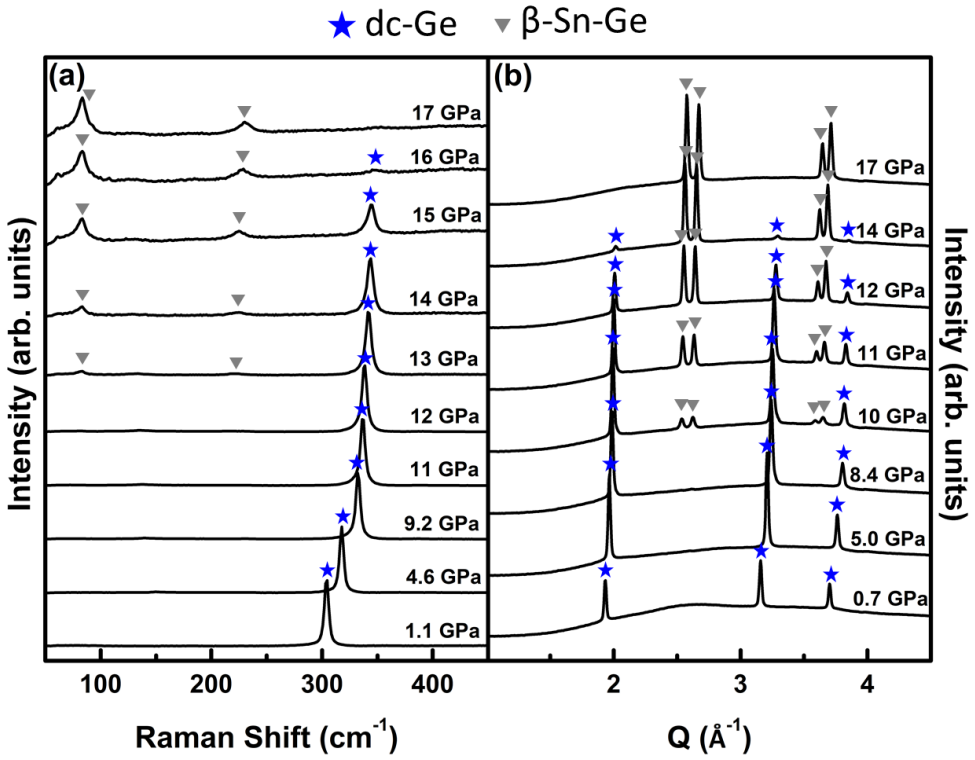

Figure 6.1: The phases observed during compression to 17 GPa of 40-60 nm diameter GeNWs using (a) Raman spectroscopy (b) X-ray diffraction.

contain a sharp peak centred at just above 300 cm^{-1} (marked with blue stars), this peak is characteristic of dc-Ge. As the pressure is increased, this peak shifts to higher wavenumbers. At 13 GPa, two additional weak peaks at 82 and 220 cm^{-1} (marked by grey triangles) are observed. These two peaks correspond to β-Sn-Ge. Between 13 GPa and 16 GPa, the relative intensities of the dc-Ge and β-Sn-Ge change, with the dc-Ge peak decreasing in intensity and the β-Sn-Ge peaks increasing in intensity. This indicates that a phase transformation from dc-Ge to β-Sn-Ge is occurring over this pressure range. At 17 GPa, the dc-Ge peak is no longer present, indicating that the phase transformation is complete. The XRD data on compression [Fig. 6.1 (b)] shows similar behaviour. The dc-Ge phase is characterised at the lowest pressures by three peaks marked with blues stars. The GeNWs remain in this phase until 10 GPa, when peaks indicated by grey triangles begin to appear. These peaks correspond to β-Sn-Ge. Between 10-14 GPa, the β-Sn-Ge peaks increase in intensity whilst the dc-Ge peaks decrease, again indicating a phase transformation from dc-Ge to β-Sn-Ge. At 17 GPa, only β-Sn-Ge remains supporting the finding of the Raman data that the phase transformation is completed before this pressure. This XRD data appears to be broadly consistent with the Raman data with the exception of the onset of the dc-Ge to β-Sn-Ge that appears to be lower in XRD than in Raman. This is likely due to the low intensity of the β-Sn-Ge Raman signal meaning that a relatively larger amount of β-Sn-Ge would need to form before it was detected using Raman than is the case for XRD.

Decompression of GeNWs is more complicated than compression, with phase trans-

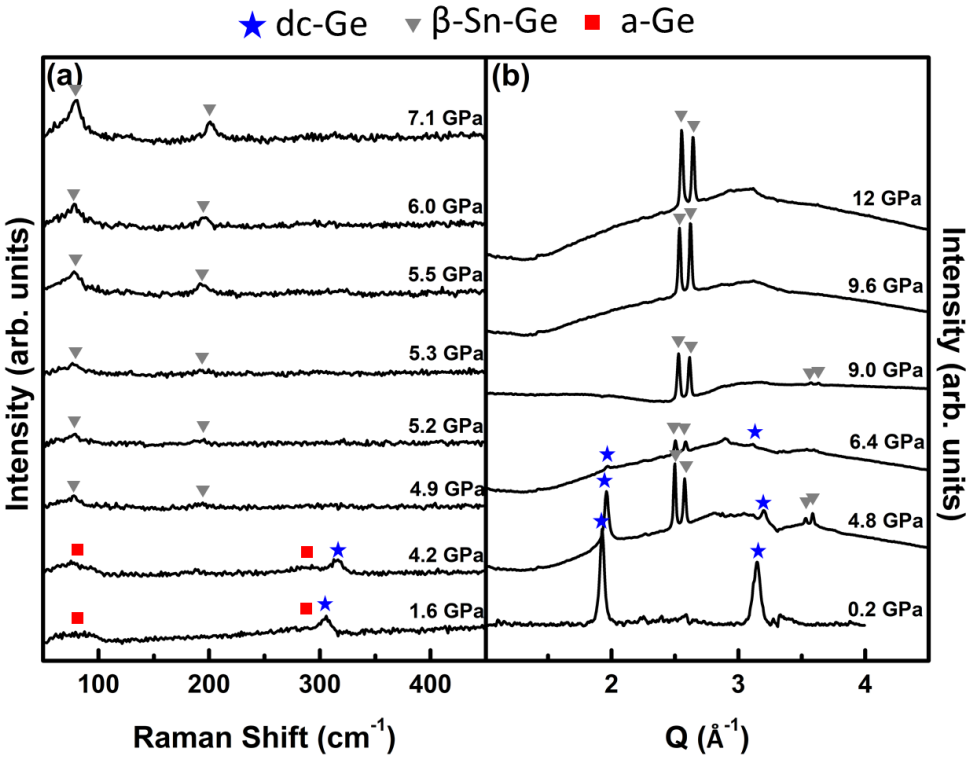

Figure 6.2: The phases observed during decompression of 40-60 nm diameter GeNWs using (a) Raman spectroscopy (b) X-ray diffraction.

formation to three different end phases occurring: dc-Ge, r8-Ge (which phase transforms to hd-Ge at ambient conditions) and a-Ge. Evidence for these end phase transformations is given in Fig. 6.2 (a-Ge and dc-Ge) and 6.3 (r8-Ge, hd-Ge, and dc-Ge). These figures show evidence of two different phase transformation pathways: β-Sn-Ge to dc-Ge and a-Ge, and β-Sn-Ge to r8-Ge and some dc-Ge. It is unclear what the determining factor is that influences which pathway is observed as the samples were loaded the same way, using the same two pressure media. Possible reasons for the two different pathways will be discussed later. These two phase transformations will now be discussed in greater detail.

Evidence of the first phase transformation pathway, β-Sn-Ge to dc-Ge and a-Ge, is presented in Fig. 6.2. Figure 6.2 (a) shows Raman spectra taken during decompression from β-Sn-Ge. At 7.1 GPa, the Raman spectrum of the GeNWs contains two broad peaks (indicated by grey triangles). These peaks correspond to β-Sn-Si. The sample remains β-Sn-Si until 4.9 GPa. This pressure is significantly lower that the 9-8 GPa that bulk β-Sn-Ge is known to phase transform to either r8-Ge or st12-Ge. At 4.2 GPa, two broad peaks marked by red squares and a sharper peak marked with a blue star can be observed. These peaks correspond to a-Ge and dc-Ge, respectively. These phases continue to be present for the rest of the decompression. XRD data on decompression is shown in Fig. 6.2. Initially, the Ge-NWs are in the β-Sn phase (as indicated by a pair of peaks marked with grey triangles). [i] The GeNWs remain β-Sn-Ge until 6.4 GPa where the presence

[i]Note that because of the x-ray energy used (25 KeV) and the small opening angle of the seat in the DAC, only a limited the range in Q was collected meaning the $\langle 113 \rangle$ dc-Ge peak was not observed.

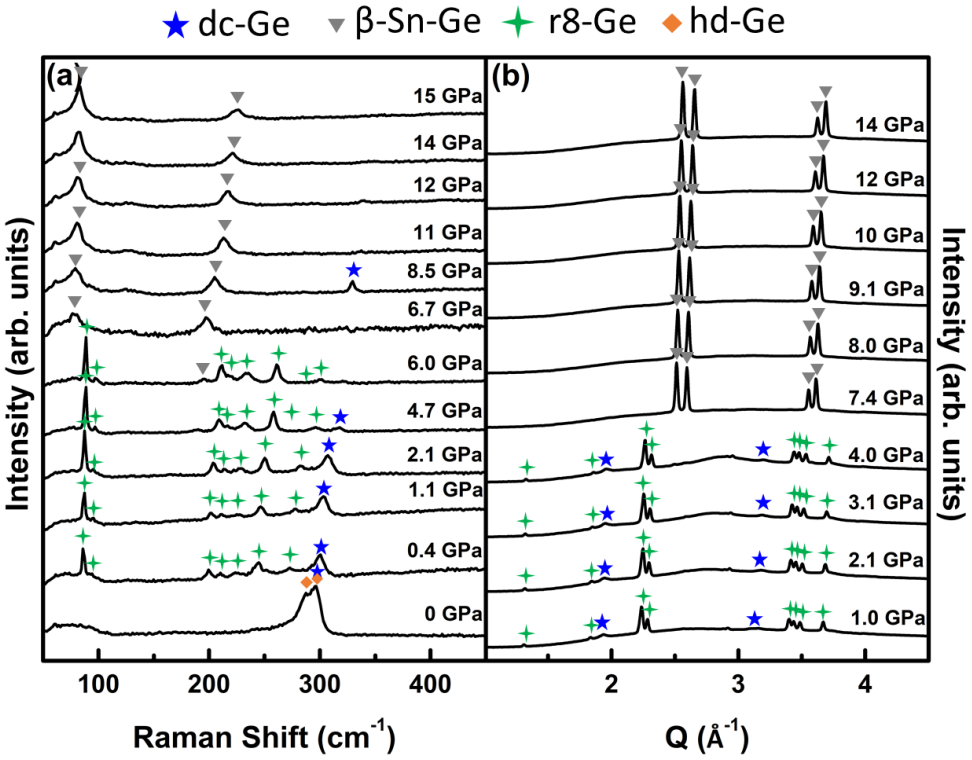

Figure 6.3: The phases observed during decompression of 40-60 nm diameter GeNWs using (a) Raman spectroscopy (b) X-ray diffraction.

of two weak peaks marked with blue stars, corresponding to dc-Ge, are observed. The intensity of the dc-Ge peaks increase whilst the β-Sn-Ge peaks decrease at 4.8 GPa, suggesting a gradually phase transformation. At 0.2 GPa, only dc-Ge in observed. Note that no a-Ge can be observed, this phase is likely to be present but has a low XRD intensity. This data is in agreement with the Raman data, however, dc-Ge is found to start forming at a slightly higher pressure.

Evidence for the β-Sn-Ge to r8-Ge (hd-Ge) phase transformation pathway is presented in Fig. 6.3. Raman spectroscopy data [Fig. 6.3 (a)] shows to GeNWs to be completely β-Sn-Ge at the highest pressure of 15 GPa. On decompression, the GeNWs remain β-Sn-Ge with the peaks shifting towards lower wavenumbers until 6.7 GPa. Between 6.7 GPa and 6.0 GPa, additional (peaks marked with green stars) appear. These peaks correspond to r8-Ge, indicating a phase transformation to r8-Ge in some of the GeNWs. At 4.7 GPa, this phase transformation is completed, however some dc-Ge is observed to form. Both dc-Ge and r8-Ge continue to exist down to 0.4 GPa. Between 0.4 GPa and ambient pressure, the r8-Ge is no longer visible and two peaks at 290 and 300 cm^{-1} (marked with orange diamonds) are present. This is the Raman signature of hd-Ge.[93] It is known that r8-Ge is unstable under ambient conditions and phase transforms to hd-Ge.[93] Some dc-Ge is also expected but due to the overlap of the dc-Ge peak and the hd-Ge Raman spectrum, it is difficult to determine the presence of this phase. XRD data for the same phase transformation is shown in Fig. 6.3 (b). As previously, these GeNWs start in the β-Sn-Ge phase. The GeNWs remain in the β-Sn-Ge phase until somewhere between 7.4 GPa

and 4.0 GPa. At 4.0 GPa, there is no longer any evidence of β-Sn-Ge, instead a number of peaks corresponding to r8-Ge (green stars) and dc-Ge (blue stars) were observed. This indicates a phase transformation from β-Sn-Ge to r8-Ge (and some trace dc-Ge) between 7.4 GPa and 4.0 GPa, consistent with the Raman data.

6.2.3 Comparison with bulk germanium

A summary of the high pressure induced phase transformations found in bulk-Ge and the GeNWs studied is found in Fig. 6.4. Compression is shown on the left side of the figure and decompression is on the right side of the graph. The colours shown indicate the phase(s) present at the pressure shown below where solid colours indicate a single phase being present and multiple colours represent multiple phases being present.

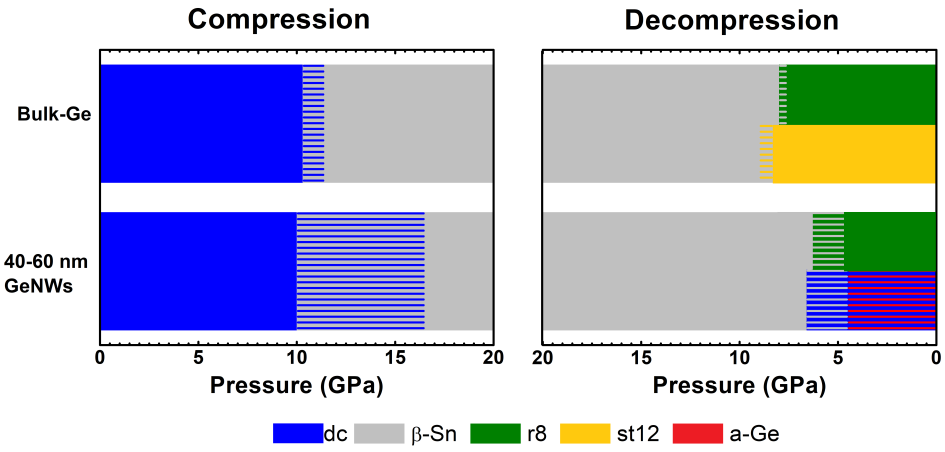

Figure 6.4: A summary of the phases present during the compression and decompression of bulk-Ge and GeNWs. Bulk-Ge data is taken from refs.[13,40]

On compression, both bulk-Ge and GeNWs start in the dc-Ge phase and phase transform to β-Sn-Ge at ~10 GPa. Whilst the onset of this phase transformation is similar to bulk-Ge, the pressure at which the phase transformation is completed differs. For bulk-Ge, the sample is entirely β-Sn-Ge by 11.4 GPa,[13] whilst in GeNWs the phase transformation is not complete until the significantly higher pressure of 17 GPa.

On decompression, bulk-Ge phase transforms from β-Sn-Ge to either r8-Ge or st12-Ge between 9-8 GPa. The end phase that forms is dependent on how hydrostatic the decompression is, with r8-Ge forming under hydrostatic environments and st12-Ge forming when there is a high presence of shear.[40] The GeNWs remain entirely in the β-Sn-Ge phase until at least ~6.4 GPa, a pressure that is much lower than that for bulk-Ge. From this pressure the GeNWs phase transform from β-Sn-Si via one of two different pathways: to a-Ge with some dc-Ge, or to r8-Ge with some dc-Ge.

6.3 Low temperature nanoindentation of Ge

It is clear from the previous section that size impacts the high pressure phase transformation pathways of Ge. In the previous chapter, it was observed that temperature affects the end phases achieved via nanoindentation of Si. This current section aims to determine if similar behaviour is observed in the nanoindentation of Ge by investigating the effect of temperature on end phases of Ge after nanoindentation.

6.3.1 Method

A Hysitron TI 900 TriboIndenter was used to perform nanoindentation. This instrument was fitted with a custom built low temperature stage that works by passing cold nitrogen gas, cooled by liquid nitrogen, through the stage. The rate of flow of the gas determined the temperature which was measured using a Co-Al thermocouple. The indenter chamber containing the stage and transducer was purged using nitrogen gas. This was done to remove the moisture in the chamber and prevent ice formation on the sample.

Using a 1.3 μm diameter spherical tip, arrays of 50 indents were made into a (100) oriented dc-Ge wafer at 20°C and for a series of lower temperatures between 10°C and -45°C. Each indent had a loading and unloading time of 10 sec and a maximum force of 10 mN. Due to the drift in the stage at low temperatures and vibrations from the flow of the N2 gas, the contact pressure could not be determined reliably

After indentation, the sample was warmed to ambient temperature and examined using Raman Spectroscopy. This was done using a Renishaw Reflex inVia Raman system using a 532 nm incident beam with a spot size of ~1 μm, intensity of ~0.1 mW, and a 2400 l/mm grating. After Raman, a FEI Helios Nanolab FIB was used to prepare some samples for TEM characterisation using the *ex situ* lift-out technique, as described in Chapter 2. The sample were initially milled at 30 keV and final thinning was done at 16 keV. The TEM sample were then examined using a Phillips CM300 TEM at 300 kV.

6.3.2 General nanoindentation behaviour

Figure 6.5 shows three distinct nanoindentation curves observed at 20°C [Fig. 6.5 (a)] and 0°C [Fig. 6.5 (b) and (c)]. In all three cases, the loading section of the curve contains a number of small discontinuities (marked with arrows). These discontinuities are known as "pop-in" events. Pop-in events are believed to be indicative of either slip/defect propagation loading.[86]

For indents made at 20°C, a featureless unloading curve is observed [Fig 6.5 (a)]. This is consistent with previous studies at this temperature where deformation is believed to occur primarily via defect propagation.[71,86] A "pop-out" event [Fig 6.5 (b)] is a sudden change in depth that occurs during unloading. Pop-out events in Si are thought to be indicative of a phase transformation from a dense crystalline phase such as β-Sn-Si to a less dense crystalline phase such as r8/bc8-Si.[75,78,98] Finally, an "elbow" event [Fig 6.5 (a)] is a change in the gradient of the unloading curve. In Si, this is indicative of an a-Si end phase.[75,98] In this current work, all the indents made in dc-Ge at 0°C contained either pop-in or elbow events during unloading, with 32% of 50 indents exhibiting a pop-out

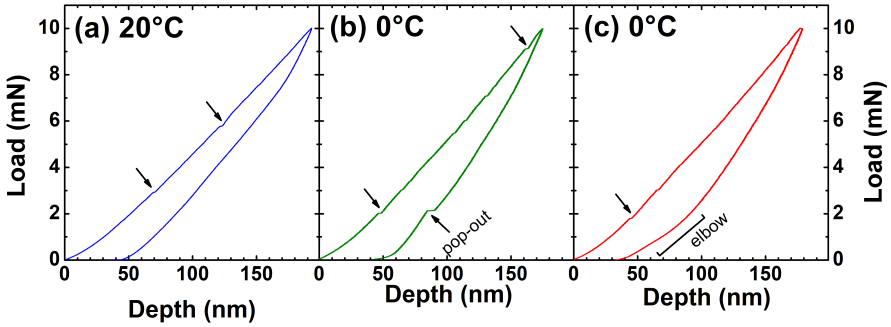

Figure 6.5: Force depth curved taken during nanoindentation of dc-Ge. (a) A typical curve observed at 20°C, and examples of curves displaying (b) "pop-out" and (c)"elbow" events during unloading at 0°C. Note for all three curves that a series of small pop-ins during loading (indicated with arrows) is observed.

and the other 68% having an elbow event.

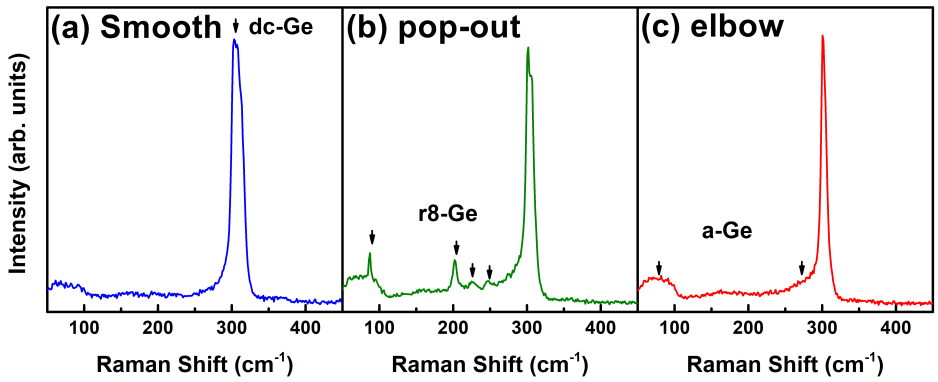

Figure 6.6: Raman spectra of indents displaying (a) featureless unloading curves, (b) "pop-out" behaviour and (c) "elbow" behaviour.

To determine if the indentation curves observed resembled those of Si, Raman spectroscopy was used to determine the structure of the residual indents. Figure 6.6 contains representative Raman spectra for indents that exhibited (a) featureless unloading curves, (b) a pop-out event, and (c) an elbow event. For the featureless curve [Fig. 6.6 (a)] a dc-Ge peak nominally centred at 300 cm^{-1}, that has been broadened to higher wavenumbers when compared to single crystalline dc-Ge (not shown), is observed. This peak is characteristic of dc-Ge that is disordered and/or containing residual stress and does not correspond to another phase of Ge.[57] A characteristic Raman spectrum for an indent with a pop-out event is shown in Fig. 6.6 (b). This Raman spectrum contains a dc-Ge peak and additional peaks at 86, 94, 202, 225, and 249 cm^{-1}. The dc-Ge peak observed is likely to come from the surrounding material due to the similar sizes of the laser spot from the Raman and the residual indents. The additional peaks observed correspond to r8-Ge and were present in most of the indents where pop-out events were observed.[24] It should be noted that r8-Ge is known to phase transform to hd-Ge at ambient temperature.[24,92,93] The Raman spectrum of hd-Ge contains a broad peak centred at 292 cm^{-1} which makes

it hard to differentiate from the dc-Ge peak. Finally, a representative Raman spectrum of a residual indent where an elbow was observed is shown in Fig. 6.6. In addition to the dc-Ge peak, two broad peaks (labelled with black arrows) are present. These broad peaks are indicative of a-Ge.

For further characterisation of the indents, TEM was employed. Figure 6.7 contains representative BF images and SADPs from the circled regions of an indent with a featureless unloading curve [(a) and (b)], a pop-out event [(c) and (d)], and an elbow event [(e) and (f)]. For indents with a featureless unloading curve [Fig. 6.7 (a)], there is clear evidence of defects under the surface. The corresponding SADP [Fig. 6.7 (b)] shows predominately dc-Ge, agreeing with the corresponding Raman spectrum [Fig. 6.6 (a)]. The XTEM image and SADP of a pop-out indent are shown in Fig. 6.7 (c) and (d). This image shows evidence of a phase transformed zone within the indent impression as well as considerable disorder in the dc-Ge below the phase transformed region. The SAPD of the phase transformation region and some of the surrounding dc-Ge material shows dc-Ge with a [110] zone axis. From the SADP, it can be concluded that the phase transformation region contains predominately hd-Ge due to the presence of multiple spots that correspond to the hd-Ge phase. These spots are circled in white. The observation of hd-Ge is consistent with the observation of r8-Ge from Raman spectroscopy as r8-Ge is known to phase transform to hd-Ge at ambient temperature within days.[24,92] Finally, the TEM image and SAPD of an indent where an elbow event was observed during unloading [Fig. 6.7 (e) and (f)] showed evidence of a phase transformed region that was a-Ge, as indicated by diffuse rings in the SADP.

In summary, three different behaviours (one at ambient temperature and the other at 0°C) based on the nanoindentation curves were observed. The first of these was a featureless unloading curve. This was observed for all indents at 20°C and was indicative of defective dc-Ge that had not phase transformed. At 0°C either elbow or pop-out events were observed for all indents, these indicating the formation of r8-Ge and a-Ge, respectively.

6.3.3 Effect of temperature

Given that there was a difference in the end phases present at 20°C and 0°C, there is clearly a strong temperature dependence. To investigate this, 50 indents were made at several different temperatures ranging from -45°C to 20°C. Statistics of the resulting end phases are summarized in Fig. 6.8. As mentioned earlier, at 20°C, all indents were found to contain (based of Raman spectroscopy) defective dc-Ge. When lowering the temperature to 10°C, r8-Ge was observed for a small number of the indents with defective dc-Ge observed for the rest. Further lowering the temperature to 0°C caused all of the indents to have either a r8-Ge end phase or an a-Ge phase. Unlike for higher temperatures, no defective dc-Ge end phase was observed at 0°C. Figure 6.8 shows that further lowering the temperature caused the fraction of r8-Ge end phase to decrease and the portion of a-Ge to increase.

The effect of varying the unloading rate at different temperatures was also investigated. These results indicated that a longer unloading time resulted in the same dc-Ge, r8-Ge and a-Ge end phases forming but there was a shift in the temperature where each end

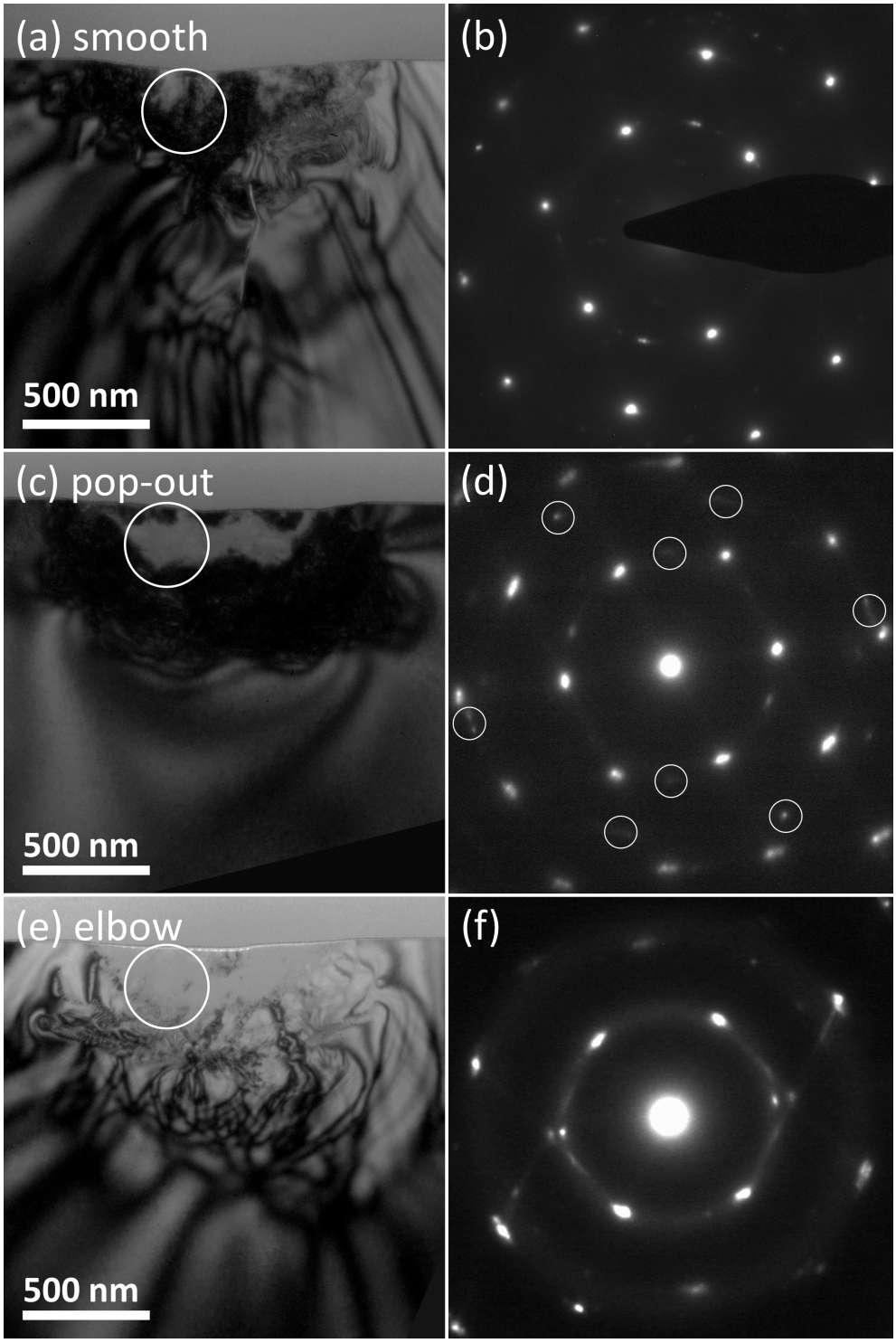

Figure 6.7: TEM images and corresponding selected area diffraction patterns from the circled regions for (a) and (b) featureless unloading curves, (c) and (d) "pop-out" behaviour and (e) and (f) "elbow" behaviour. (Images courtesy of Lachlan Smillie, ANU)

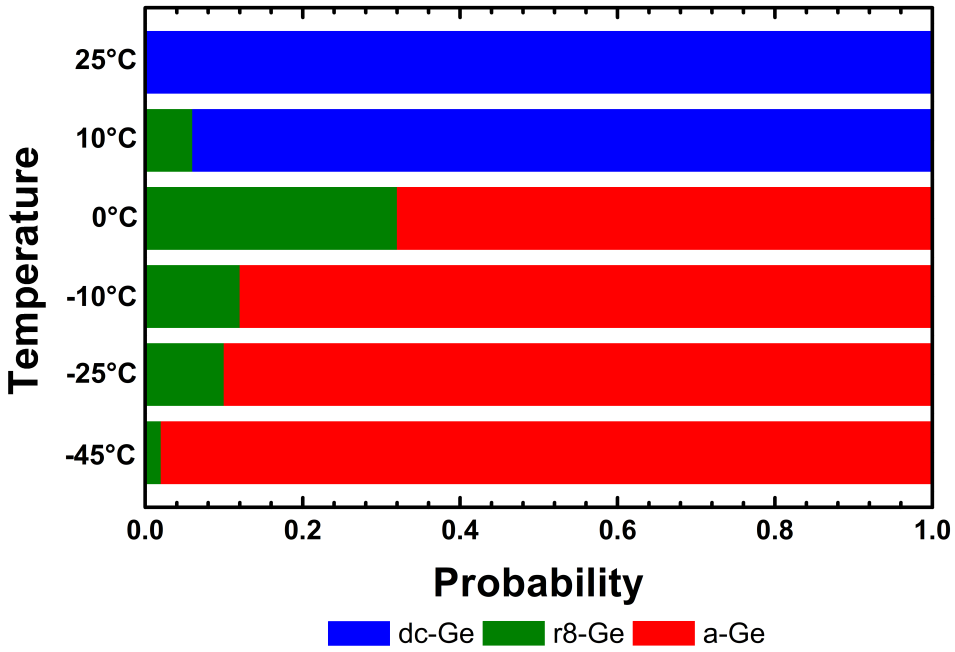

Figure 6.8: The fraction of indents in dc-Ge out of 50 containing a particular end phase (defective dc-Ge, r8/hd-Ge or a-Ge) as a function of temperature.

phase occurred. For example, using a 20 s unloading time (whilst keeping the maximum force and loading time constant) at 0°C, gave results similar to 10°C with a 10 s unloading time where 2 indents containing r8-Ge and 48 indents with defective dc-Ge were observed. More r8-Ge was, however, observed for a 20 s unloading time at -25°C where 13 indents had the r8-Ge end phase and 37 indents had the a-Ge end phase. These results indicated, as observed in Si in the previous chapter, unloading time plays a role in the ability to nucleate crystalline end phases.

6.4 Discussion

Details of the phase transformation behaviour in GeNWs will be discussed first. It has been shown that GeNWs phase transform to β-Sn-Ge over a larger range of pressure (10-17 GPa) than bulk-Ge on compression (10.3-11.2 GPa)[13]. On decompression, β-Sn-Ge remains until much lower pressures than bulk-Ge and phases transforms to either dc-Ge and a-Ge or r8-Ge and dc-Ge. Although the full understanding of the energetics of the phase transformation pathways would require detailed modelling and is thus outside the scope of this work, it is clear that similar to the case of Si as shown in previous chapters, the small size (volume) of the GeNWs influences the phase transformations pathways when compared with bulk-Ge.

The significantly higher pressure at which the phase transformation to β-Sn-Ge on compression is fully completed suggests that, like in the case of SiNWs, the nucleation of β-Sn-Ge becomes more difficult as material volume decreases. The dc to β-Sn phase transformation (like Si) is reconstructive. It can be argued that similar to Si, a combina-

tion of the reconstructive nature of the phase transformation and the small volume of the GeNWs causes the difficulty in the formation of β-Sn-Ge in GeNWs.

Like the dc-Ge to β-Sn-Ge phase transformation, the β-Sn-Ge to r8-Ge phase transformation is also reconstructive and this raises a potential nucleation issue. When combined with the lack of nucleation sites due to the small volume of the GeNWs, nucleation of r8-Ge becomes more difficult and hence the GeNWs remain β-Sn-Ge until much lower pressures. If β-Sn-Ge remains until much lower pressures, it eventually reaches a pressure where it becomes unstable and needs to phase transform. If no crystalline phases have nucleated when this pressure is reached, a-Ge forms. This is essentially a similar argument to the β-Sn-Si to r8/bc8-Si nucleation problem for SiNWs and small volumes.

It is interesting that st12-Ge was not observed during the decompression of the GeNWs. This is likely due to the fact that GeNWs are decompressed in a hydrostatic environment. It is known that st12-Ge is favoured when decompression is done with a high component of shear whereas r8-Ge forms under hydrostatic conditions.[40]

The reason for the different decompression pathways of GeNWs is unclear. Many factors such as the temperature, method of loading the cell, and the size of the GeNWs were kept constant for all the experiments. The pressure medium used did not impact the final phases formed (predominately r8/hd-Ge or predominately a-Ge) as both phase transformation pathways were observed when using two different pressure media.

A possible explanation for the different phase transformation pathways could be the rate of decompression between about 6-7 GPa. When dc-Ge and a-Ge formed, small steps in pressure were used whilst a larger decrease in pressure of 0.7 GPa to 3.4 GPa occurred suddenly when r8-Ge formed. In previous chapters, it was observed that a decompression rate of $\sim$2 GPa/hr resulted in the formation of significantly more dc-Si at 165°C than for decompression at 15 GPa/hr at the same temperature. Another reason for the formation of r8-Ge in some GeNWs could be related to the change in density that occurs during the β-Sn-Ge to r8-Ge phase transformation. The density of r8-Ge is significantly less than β-Sn-Ge and hence the GeNWs need room to expand. In bulk-Ge, a sudden decrease in pressure has been observed to occur between $\sim$7.5 and $\sim$5 GPa during the formation of r8-Ge.[40,164] Thus, the rate of decompression, coupled with nucleation issues for small volumes and density changes during phase transformation could all contribute to the phase transformation pathways observed. Therefore, under some conditions NWs may remain in the β-Sn-Ge phase until quite low pressures, favouring transformation to a-Ge and even dc-Ge rather than r8-Ge that is favoured in bulk Ge. Hence, more experiments on decompression rate would be needed for GeNWs to resolve this issue.

The nanoindentation results show that nanoindentation of dc-Ge at 20°C normally does not induce a phase transformation; defective dc-Ge is the only end phase. However, lowering the temperature to 0°C favours the formation of r8-Ge and a-Ge on decompression, with a-Ge being more favoured at the lowest temperatures. The possible mechanisms for the formation of these observed end phases will now be discussed.

At ambient temperature, defective dc-Ge was the only end phase observed. For this observation, the most likely explanation involves the formation of defects during loading. For instance, plastic deformation during loading involves the sudden formation and propagation of defects (that give rise to the pop-ins observed in Fig. 6.5 (a)) and this process causes the effective pressure under the indenter tip to decrease. This defect formation

is believed to occur at a rate such that it prevents the critical pressure for phase transformation from being easily reached, thus β-Sn-Ge does not form and deformation only occurs via the formation and propagation of defects.

The r8-Ge and a-Ge end phases observed at lower temperatures can be explained in terms of favouring phase transformation on compression and limited nucleation on decompression. Lowering the temperature is suggested to slow the occurrence of deformation via slip/crystalline defect generation on compression. This results in the pressure underneath the tip being able to increase to the critical phase transformation pressure. During unloading β-Sn-Ge transforms into either r8-Ge or a-Ge. As the temperature decreases, the ability to nucleate r8-Ge in a small volume decreases and a-Si is favoured. Thus, as a result of nucleation difficulties, it is clear that temperature plays a critical role in determining the resultant end phase of Ge after the application of pressure. In nanoindentation, lowering the temperature (down to 0°C) favours a phase transformation and enables r8-Ge formation but further lowering the temperature then suppresses the nucleation of r8-Ge since there is less thermal energy at lower temperatures below -10°C. In this case the nucleation of crystalline phases becomes energetically unfavourable and a-Ge is instead observed. Indeed, the nucleation of crystalline phases is also affected by the unloading rate and using a longer unloading time does increase the fraction of r8-Ge observed at lower temperatures.

From the GeNW behaviour, it is clear that size affects the high pressure phase transformation behaviour of Ge. This is less clear in nanoindentation as the formation of defective dc-Ge occurs at ambient temperature rather than phase transformation and this complicates a size-effect study using nanoindentation. However, at lower temperatures, when phase transformation dominates, size may very well be relevant. In the 20°C down to -45°C temperature range in this nanoindentation study, comparison with DAC studies in the literature indicate that bulk-Ge is found to form the crystalline st12-Ge or bc8-Ge phases.[22,43] On the other hand the indents in this study (where the depth of the phase transformation volume was ∼220 nm) had end phases of mostly a-Ge and some r8-Ge. As in the case of Si, the small phase transformation volume reduces the number of potential nucleation sites, suppressing the nucleation of r8-Ge. If no r8-Ge begins to nucleate, the β-Sn-Ge becomes unstable and the high driving force to phase transform leads to amorphisation.

Thus, as in Si, it is clear that size is an important factor in the phase transformation behaviour in Ge. Whilst a less comprehensive study on Ge has been performed when compared with Si in the previous chapters, some general trends can be determined from these data and this can be further extrapolated based on the results of Si.

6.5 Discussion of the phase transformations of silicon and germanium

So far in this thesis, the high pressure phase transformations of small volumes of Si and Ge have been explored and compared with bulk behaviour. It was found that, in general, the same three end phase (amorphous, r8/bc8 and dc) formed during both the decompression of NWs and under nanoindentation experiments. So far, the phase transformation

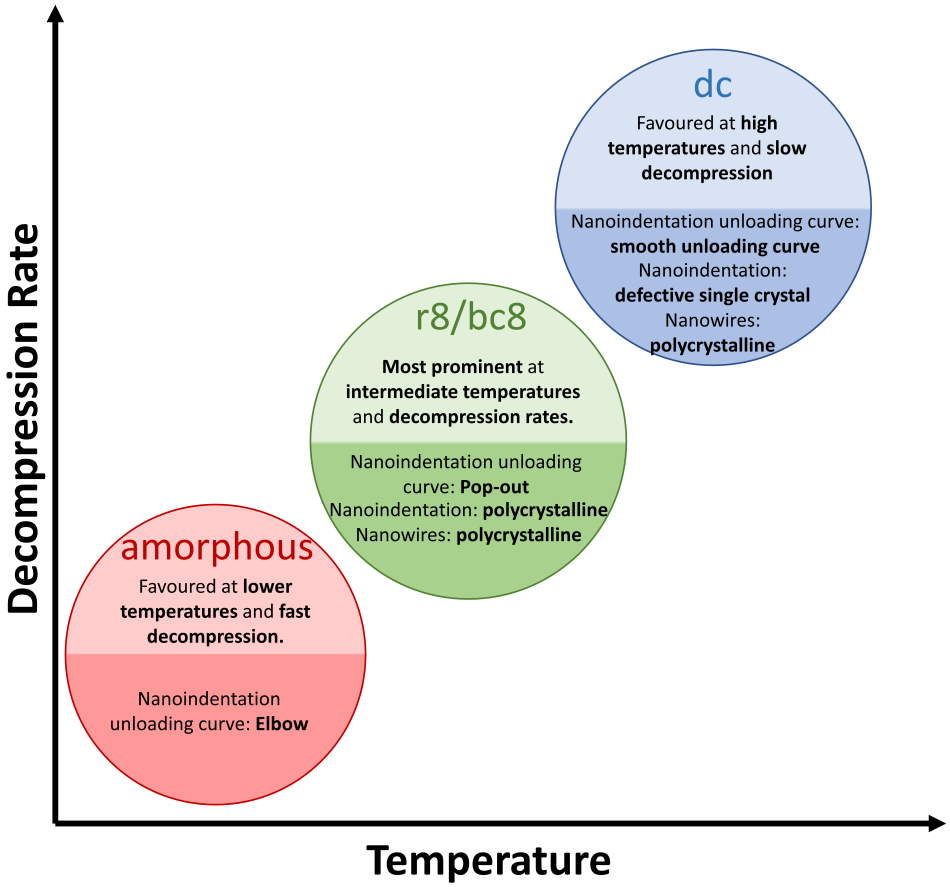

Figure 6.9: General observations for the formation of the three end phases in Si and Ge.

behaviour of each element has been discussed individually. In this section, the phase transformation behaviour of the two elements will be compared and contrasted.

To begin with, a summary of the general conditions and behaviour for the formation of an amorphous, bc8 and dc end phase is presented in Fig. 6.9. All these phases result from the instability of the β-Sn phase on decompression. The specific conditions at which each end phase forms will now be discussed.

The first end phase that will be discussed is the amorphous phase. In general, the amorphous phase is favoured under conditions with fast decompression and low temperatures. These conditions are characteristic of a nucleation limited regime. For both elements, β-Sn was found to persist in a metastable state at pressures lower than those at which the β-Sn is thermodynamically stable.[55,57] Another similarity observed for the amorphous end phase for both elements is the observation of an elbow in the unloading curve during nanoindentation.

Interestingly, the temperature regimes where the amorphous phase is the dominant end phase differs in Si and Ge. For Si "low" temperature was about 25°C whilst for Ge indentation at temperatures below about -25°C resulted in significant formation of a-Ge. Thus, the amorphous phase can form at higher temperatures in Si than in Ge. This would

suggest that the formation of crystalline phases is easier in Ge than in Si, a point that will now be explored.

When the temperature was increased or the decompression rate decreased, the crystalline r8/bc8 and dc phases formed. The formation of the r8/bc8 end phase will be discussed first. In general, this phase was observed to occur at intermediate decompression rates and temperatures. "Intermediate" temperatures for Si (70-135°C) are considered to be much higher than intermediate temperatures for Ge (-25-0°C). In agreement with the literature, the formation of the bc8/r8 end phase was observed to occur if there was a pop-out event in the unloading curve during nanoindentation. Additionally, in both the SiNWs and nanoindentation, individual indents/SiNWs predominately is a single phase that begins to form away from the surface. Due to the limited scope of the Ge study, it is unknown if the recovered GeNWs are single phase but one might expect this to be the case due to similarities in Si and the single end phase observed for nanoindentation of dc-Ge at low temperatures.

There are some differences in the r8/bc8 end phases. For example, whilst bc8-Si is stable at ambient temperature, r8-Ge and bc8-Ge are not stable and phase transform to hd-Ge.[24,40] This was also found to be the case in the NWs where the end phase of some the SiNWs was bc8-Si, whilst the r8-Ge NWs were observed to transform to hd-Ge before reaching ambient pressure. Additionally, in nanoindentation, a residual strain of ∼4GPa stabilises the r8 phase of Si,[77] meaning that the end phase after nanoindentation contains about 70% r8-Si and 30% bc8.[77] This differs from the bc8-SiNWs which appear to contain almost 100% bc8-Si.

The dc end phase is most prominent during slow decompression and at "high" temperature for both Si (165°C) and Ge (25°C). During nanoindentation, this phase was observed to occur when a featureless unloading curve was observed. When dc-Si was the end phase in the SiNWs, it was polycrystalline whilst during nanoindentation of Si, the phase was found to be single crystal with defects. The difference in the crystallinity of the dc-Si end phase is due to the different ways dc-Si forms where crystallites randomly grow in the SiNWs and epitaxially in nanoindentation. For Ge, it would be anticipated that GeNWs with a dc-Ge end phase would also be polycrystalline, However for nanoindentation, the dc-Ge end phase is not a result of phase transformation occurring on loading but deformation by defect propagation.

It appears that there is a general trend where Ge behaves somewhat similarly to Si but at lower temperatures. To put this trend in a wider context, a summary of the phase transformations of Si and Ge arranged by temperature is shown in Fig. 6.10. Here, it is clear that phase transformations in Si occur at a much higher temperature than Ge, for example, the melting point of Si (1412°C) is much higher than the melting point of Ge (940°C).[165] Additionally, all thermally activated phase transformations involving metastable phases such as amorphous to dc, r8/bc8 to hd and hd to dc all also occur at higher temperatures for Si than Ge. Additionally, when the ratio of the phase transformation temperature (T) and the melting point (T_m) are compared for Si and Ge, the values are very similar. These values can be found in Fig. 6.10. Also, the order from lowest to highest temperature of these phase transformations is the same for Si and Ge. As each phase transformation process in Si occurs at a higher temperature than for Ge, the energy barriers for these processes in Si must be higher than for the equivalent processes in Ge.

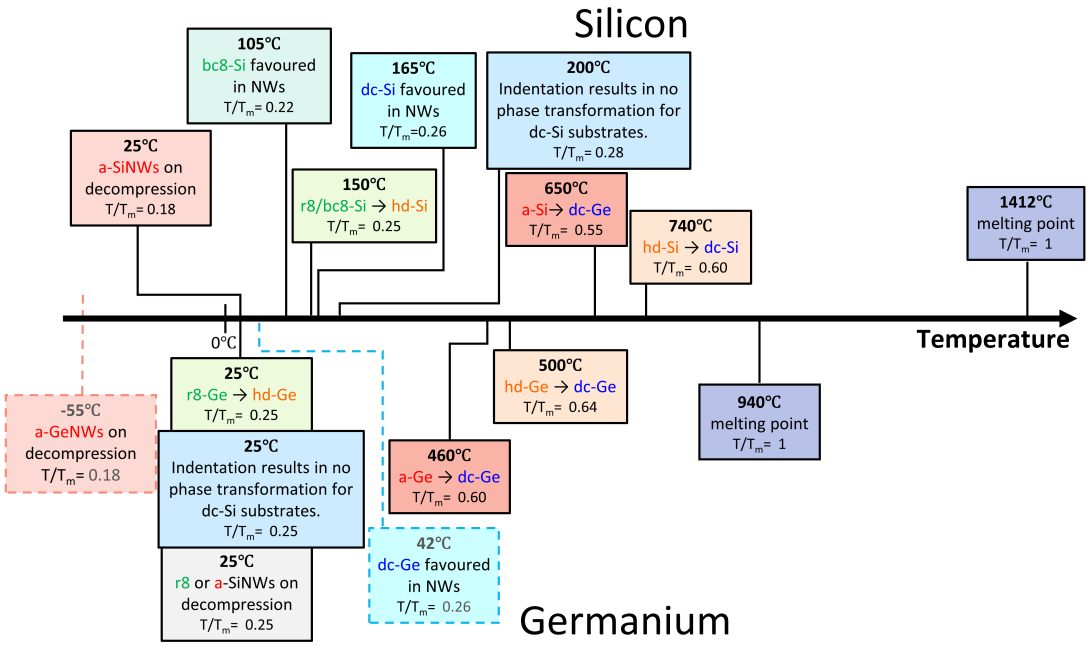

Figure 6.10: A summary of the temperatures at which the phase transformations of Si and Ge occur. Data is from Refs.[22,40,62,107,157,165,166] The ratio of the temperature of phase transformation (T), and the melting point of the material (T_m) is also given.

Given that the phase transformations of Ge appear to occur at lower temperatures than the equivalent phase transformations in Si and T/T_m is for each phase transformation is similar in Si and Ge, some insight can be obtained into possible phase transformations not yet observed. For example, the GeNWs were only compressed at ambient temperature, resulting in a mixture of either hd-Ge and a-Ge or dc-Ge and a-Ge, with no observation where all the GeNWs had an amorphous end phase. As amorphisation of SiNWs occurs at ambient temperature, it is likely that a similar behaviour could be observed below ambient temperature. Based on T/T_m for the formations of a-Si in SiNWs, GeNWs are likely to have an entirely a-Ge end phase at approximately -55°C.

As r8 is unstable at ambient temperature, no r8-GeNWs could be recovered under ambient conditions. If the temperature were to be decreased slightly, below 0°C, it might be possible for r8-Ge to more reliably form in GeNWs. However, once brought to ambient temperature, they would phase transform to hd-Ge.

As dc-Si was the dominant end phase for SiNWs compressed at 165°, there is likely a temperature at which dc-Ge is the only end phase observed after compressing GeNWs. This temperature should be lower than for Si, and slightly higher that the dc-Ge to hd-Ge phase transformation temperature. Therefore, it could be anticipated that predominately dc-GeNWs form at ∼50°C.

6.6 Conclusions

In conclusion, it is clear that for Ge the volume of the material and the temperature both play an important role in determining the end phase after compression Ge to high

pressures. This is true for both GeNWs within DACs and nanoindentation of dc-Ge at the low loads used in this work. Both small phase transformation volumes and low temperature limit the nucleation of crystalline phases, causing phase transformation into a-Ge. It was also found that reducing the temperature in nanoindentation from 20°C to 0°C reduced the formation of defective dc-Ge during nanoindentation and favoured phase transformation. Much of this detail is quite similar to the behaviour observed in Si in the previous chapters.

Chapter 7

Discussion, concluding remarks and future work

The high pressure phase transformation behaviour of small volumes of Si and Ge were explored in the previous chapters. It was found that small volumes of Si and Ge have broadly similar end phases for both the compression of nanowires and nanoindentation. In this chapter concluding remarks, the implications of this work and future work is discussed.

7.1 Conclusions

The high-pressure-induced phase transformation behaviour of Si and Ge is affected by many factors such as shear, impurity level, strain rate, temperature, and volume of material. A summary of the factors that are known to influence the phase transformation behaviour, is found in Table 7.1. In this table, the known results from literature are shown in black whilst the new insights from this thesis are shown in blue. Before this study, the effect on pressure induced phase transformations of material volume had only been studied for very small size and near-bulk to bulk behaviour. This work focused on NWs and also small volume nanoindentation, and has provided the first comprehensive study of size effects during pressure induced phase transformation. In particular, it was found that the dc to β-Sn phase transformation threshold is increasingly suppressed as material volume is decreased. For some of the smallest (80-150 nm) SiNWs, the β-Sn phase was not observed, instead transforming directly to sh-Si. During decompression, a similar suppression of phase transformation was observed where β-Sn-Si was observed to remain until much lower pressures than for bulk materials. At ambient temperature, β-Sn-SiNWs phase transformed to predominately a-Si, in contrast to bulk-Si where bc8-Si formed. However, bc8-Si was observed to occasionally form in the larger SiNWs and also under very slow decompression. This suppression of phase transformation is believed the be caused by the small volumes of the NWs causing difficulties in the nucleation of new crystalline phases. It was additionally observed that SiNWs behave progressively more like bulk-Si as the size is increased. Increasing the temperature at which the SiNWs were compressed and decompressed resulted in the formation of bc8-Si and dc-Si end phases at intermediate temperatures (70-135°C), and predominately dc-Si at the highest temperature (165°C). When these phases formed, they were found to be polycrystalline. This differed from the behaviour observed in bulk-Si where bc8-Si formed at intermediate

Table 7.1: A summary of factors that influence the high pressure phase transformation behaviour of Si and Ge. The blue text indicates the findings from this thesis.

Effect	DAC Si	DAC Ge	Nanoindention of Si	Nanoindention of Ge
Shear	Not studied	On decompression: High shear: β-Sn-Ge $\Rightarrow$ st12-Ge Low Shear: β-Sn-Ge $\Rightarrow$ bc8-Ge[40]	High Shear: Extrusion in a-Si and r8-Si Low Shear: r8-Si	Sharp tips (high shear) *may* induce phase transformation (β-Sn-Ge $\Rightarrow$ r8-Ge or st12-Ge but normally only defect propagation (no phase transformation)
Impurity Level	Phase transformation is suppressed at high impurity levels.[38,101]	Not studied	Phase transformation is suppressed at high impurity levels.[83]	Not studied
Strain Rate	Slow: β-Sn-Si $\Rightarrow$ r8-Si $\Rightarrow$ bc8-Si Fast: β-Sn-Si $\Rightarrow$ a-Si[33,34]	Fast: st12 Slow: bc8 Also affected by shear.[40]	Slow: β-Sn-Si $\Rightarrow$ bc8/r8-Si Fast: β-Sn-Si $\Rightarrow$ a-Si[75,76]	No significant effect observed to date at room temperature (not studied) Fast decompression below ambient temperature increases the probability of an a-Ge end phase
Temperature	Very High: β-Sn-Si $\Rightarrow$ dc-Si[101] High: β-Sn-Si $\Rightarrow$ hd-Si[102] Ambient: β-Sn-Si $\Rightarrow$ r8-Si $\Rightarrow$ bc8-Si[5,26] Low: β-Sn-Si $\Rightarrow$ a-Si[22]	Very High: β-Sn-Ge $\Rightarrow$ dc-Ge[101] High: β-Sn-Ge $\Rightarrow$ hd-Ge[101] Ambient: β-Sn-Si $\Rightarrow$ st12-Ge/ r8-Ge $\Rightarrow$ bc8-Ge[101] Low: β-Sn-Ge $\Rightarrow$ a-Ge[22]	High: defect propagation, no evidence of phase transformation.[107] Ambient: bc8/r8-Si[78] Low: a-Si[107] Under slow decompression at high temperatures, dc-Si can grow from the dc-Si substrate into the β-Sn-Si region.	Ambient: dc-Ge Just below ambient: r8-Ge Low: a-Ge
Material Volume	Bulk: bc8-Si end phase 80-250 nm: mostly a-Si end phase, slow decompression leads to some bc8-Si. 10-50 nm: amorphisation on decompression[94] Increasing the temperature when compressing 80-150 nm SiNWs allows for bc8-Si and dc-Si to form in essentially phase-pure NWs.	<5 nm nanoparticle: pressure induced amorphisation on compression.[111] 40-60 nm NWs: higher transition pressure for β-Sn-Ge formation, β-Sn-Ge is more stable on decompression and transforms to either a-Ge, dc-Ge or r8-Ge. 13-100 nm nanocrystals: higher transition pressure to β-Sn-Ge formation.[112]	Like in SiNWs, the dominant end phase of indents with small phase transformation volumes is a-Si.	Whilst dc-Ge deforms via defect formation and propagation at ambient temperature, the a-Ge end phase observed at lower temperatures would indicate a size effect as bulk-Ge will always have a crystalline end phase at the temperatures studied.[22]

temperatures, and a mixture of bc8-Si and hd-Si was observed at 165°C. This difference in the end phases of Si after the application of high pressure is also believed to be due to the size of the SiNWs. Here the small size of the SiNWs suppresses the nucleation of r8-Si such that the kinetic barrier to the formation of the thermodynamically more favourable dc-Si phase from β-Sn-Si can be overcome at elevated temperatures when more thermal energy is available. The phase transformation behaviour of SiNWs and low load nanoindentation, where the volume under pressure was similar in both cases, were also compared. Despite the phase transformation volume in nanoindentation being subjected to significantly higher pressure gradients and being surrounded (confined) by dc-Si, low load nanoindentation of Si behaves remarkably similar to SiNWs in a DAC. For example, at ambient temperature, like for SiNWs, a-Si was the dominant end phase after the application of pressure. Additionally, the r8/bc8-Si end phase was found to occur at similar temperatures (105°C) to SiNWs. The dc-Si end phase was also observed in nanoindentation at 105°C, but only during slow unloading. However, instead of randomly nucleating in the phase transformation volume as is the case for SiNWs, the dc-Si grows from the dc-Si substrate. From these results, it appears that the size of the phase transformation volume affects the end phase observed after nanoindentation in a somewhat similar way to SiNWs but some behaviour is clearly different and presumably a result of significant stress gradients and confinement in the case of nanoindentation.

The temperature dependence of nanoindentation of Ge was also explored. It was well established that dc-Ge deforms via plastic flow and propagation of defects at ambient temperature. This behaviour is quite similar to the dc-Si observed during high temperature nanoindentation of Si.[107] Nanoindentation studies of dc-Ge in this work showed that whilst at ambient temperature, defect propagation in dc-Ge was dominant, r8-Ge and a-Ge end phases formed once the temperature was reduced to 0°C. At lower temperatures, a-Ge was the dominant end phase. As the load during nanoindentation was low, it is possible that the phase transformation behaviour was affected by the phase transformation volume. This is because the amorphous end phase, which is a characteristic end phase for small volumes, was observed at temperatures where crystalline phases form in bulk-Ge.[22] The effect of volume on the phase transformations of Ge has only been reported for very small $<$ 5nm nanocrystals, and for polycrystalline starting material. To further understand the effect of size on the phase transformations of Ge, 40-60 nm diameter GeNWs were compressed using a DAC. On compression, the onset of the dc-Ge to β-Sn-Ge phase transformation was similar to that of bulk-Ge; however, significantly more pressure was required to complete the phase transformation. Similar to SiNWs, the β-Sn-Ge phase was found to persist to much lower pressures than in bulk-Ge. For the GeNWs, hd-Ge (which forms from via r8-Ge), dc-Ge, and a-Ge were all observed after decompression from β-Sn-Ge. Based from the results of this work and the prior literature, there are clearly some similarities in the high pressure behaviour of Si and Ge. For example, the suppression of all phase transformations is observed as volume is reduced and similar dc, amorphous and bc8/r8 end phases were observed on decompression. Additionally, similar end phases in nanoindentation of Si and Ge were observed to occur but in different temperature regimes. In summary, this thesis has clearly highlighted the differences between bulk and small volumes of Si and Ge, especially the suppression of phase transformation as volume decreases and difficulties nucleating crystalline end phases. In particular, the

following new insights have emerged from this work:

- Progressive suppression of dc to metallic phase transformation for both Si and Ge as size decreases and total suppression of the β-Sn phase in favour of sh-Si for some of the smallest SiNWs.
- Phase transformation is also suppressed on decompression, where the β-Sn phase remains until much lower pressures than in the bulk and phase transformation to crystalline allotropes is suppressed.
- Crystalline bc8-Si and dc-Si form on decompression of SiNWs at higher temperatures. Bc8-Si forms most prominently at 70-135°C and dc-Si is the dominant end phase at 165°C.
- Both r8-Ge and a-Ge were observed to form in GeNWs during decompression.
- Low load nanoindentation with small phase transformation regions has parallels with SiNWs in a DAC.
- When the crystalline phases formed the resulting phase transformed NWs/indents appear to be near-phase-pure.
- When dc-Si is the end phase for the SiNWs, it forms via random nucleation and growth, whereas for nanoindentation, it grows from the underlying material. For fast decompression rates or the lowest temperatures, the formation of r8-Ge is suppressed.
- Lowering the nanoindentation temperature of Ge suppresses defect propagation on loading allowing for phase transformation with r8-Ge and a-Ge observed as end phases.
- Like in nanoindentation, the decompression rate of SiNWs in a DAC (at 105°) affects the final phase, with fast decompression rates suppressing the nucleation of crystalline phases.

7.2 Technological implications of this work

This study has shown that near-phase-pure Si (and Ge) NWs of bc8/hd phases can be produced under compression/decompression. This opens up the possibility of exploiting various metastable phases of Si and Ge for technological applications. As near phase pure bc8-SiNWs were successfully synthesized in this work, the next step would be to measure their properties. This is of importance as bc8-Si nanoparticles have been predicted to be useful for multiple exiton generation solar energy conversion.[63] Hd-Si is known to form via the annealing of bc8-Si,[12] and is predicted to have a direct bandgap when strained.[56] Thus, the fabrication of pure bc8-SiNWs could lead to the formation of impurity free hd-SiNWs that could easily be strained to create a direct band gap form of Si.[56] In addition, bc8-Si has recently been shown to have a 0.03 eV band gap.[52] As hd-Ge was the final phase for some of the GeNWs, it now should also be possible to test the optical and electronic

properties of this phase. This phase is of technological interest as it is predicted to have a direct band gap of 0.19-0.55 eV.[57,60] Additionally, low temperature nanoindentation of Ge provides an alternative method to form hd-Ge that does not require the dc-Ge substrate to be amorphised first. To do this, appropriate unloading conditions that produce a high portion of hd-Ge need to be determined. If this is achieved, nanoindentation could be used to produce large arrays of this phase, enabling the fabrication of devices that exploit its desirable properties.

7.3 Future work

Whilst this work has significantly improved the understanding of the high pressure phase transformation behaviour of Si and Ge, some further questions naturally arise. Possible future work is listed below:

- As near phase pure bc8-SiNWs and hd-GeNWs were successfully synthesized, it would be interesting to measure the optical and electronic properties of bc8-SiNWs, hd-SiNWs (made from annealing bc8-SiNWs), and hd-GeNWs. This will determine of the suitability these materials for various technological applications.

- It would also be interesting to explore alternative methods to produce pure NWs with different crystal structures. For example, nanoindentation can be used to reliably produce r8/bc8-Si and hd-Ge in a scalable manner. It might be possible to use the material produced from nanoindentation as a seed for growing nanowires with these exotic phases using conventional NW growth. This would be a technologically more attractive pathway than synthesizing these phases using high pressure.

- During the annealing study (Chapter 4), Si-XIII was observed to form in the bulk-Si sample above 140°C. This phase has only been previously reported to form after annealing the mixed r8/bc8-Si phase formed via nanoindentation and has an unknown structure.[19] Further experiments to maximise the amount of Si-XIII could be performed to determine its structure.

- In this work, only one diameter range of GeNWs was studied. To further understand the effect of size in the phase transformation behaviour of Ge, a larger volume range of GeNWs is needed. Additionally, the temperature dependence of GeNWs would also be important to study.

- In Chapter 5, it was proposed that under the right conditions, dc-Si could form from β-Sn-Si via epitaxial regrowth from the dc-Si substrate . As epitaxial growth rates are known to be dependent on orientation, it is likely that nanoindentation on wafers with different orientations could yield different results for the same nanoindentation conditions. This would therefore be worthwhile investigating.

- In this study, the influence of temperature on the nanoindentation induced phase transformations of Ge was only performed on dc-Ge. As a-Ge has been shown to have a dc-Ge or hd-Ge end phase at ambient temperature,[92] it is likely that a temperature

dependence study for an a-Ge starting material would reveal substantial differences to dc-Ge.

- Additionally, nanoindentation of Ge was only performed at one maximum load of 10 mN, resulting in a phase transformation depth ∼200 nm. It is therefore possible that these results were influenced by the small volume used and it would therefore be interesting to perform low temperature indentation of Ge at higher loads which would result in larger phase transformation volumes.

Appendix A

Phase diagram of 80-50 nm SiNWs

Figure A.1 contains a diagram showing the phases formed when decompressing 80-150 nm SiNWs from the β-Sn-Si phase. The circles showed on the diagram indicate the phases present under the pressure temperature conditions shown, where grey indicates β-Sn-Si, blue indicates dc-Si, green indicates bc8-Si, and red indicates a-Si

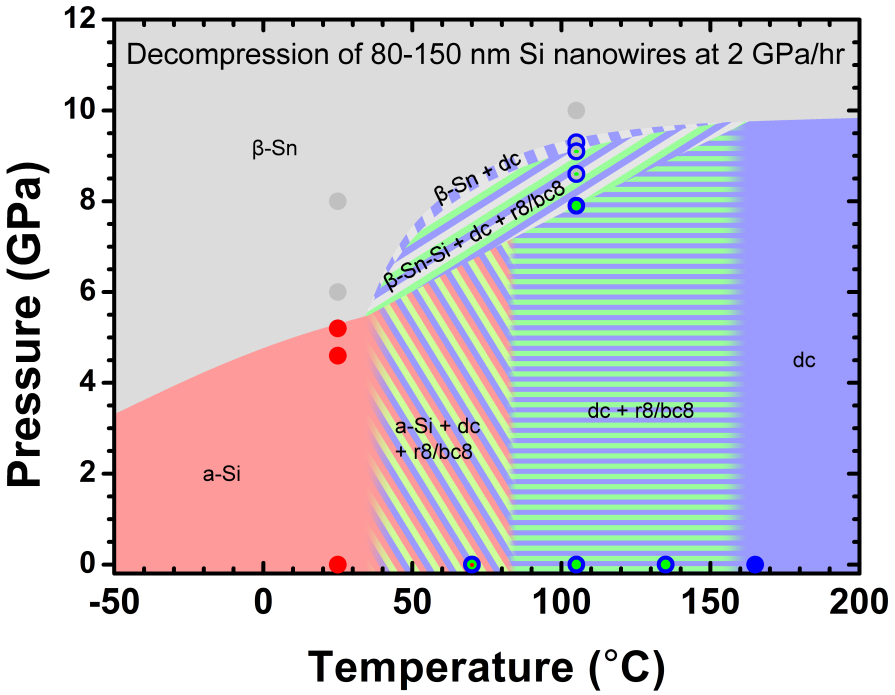

Figure A.1: A pressure temperature diagram of the phases formed in 80-150 nm SiNWs during decompression at ~2 GPa/hr. The slope of the β-Sn-Si/a-Si line is inferred from the behaviour of bulk-Si at low temperatures from Imai et al.[43].

Bibliography

[1] Mangalampalli S.R.N. Kiran, Bianca Haberl, Jodie E. Bradby, and James S. Williams. Chapter five - nanoindentation of silicon and germanium. In Lucia Romano, Vittorio Privitera, and Chennupati Jagadish, editors, *Defects in Semiconductors*, volume 91 of *Semiconductors and Semimetals*, pages 165 – 203. Elsevier, 2015.

[2] H. I. T. Hauge, M. A. Verheijen, S. Conesa-Boj, T. Etzelstorfer, M. Watzinger, D. Kriegner, I. Zardo, C. Fasolato, F. Capitani, P. Postorino, S. Kölling, A. Li, S. Assali, and E. P. A. M. Stangl, J.and Bakkers. Hexagonal Silicon Realized. *Nano Letters*, 15(9):5855–5860, 2015.

[3] A. Jayaraman. Diamond anvil cell and high-pressure physical investigations. *Review of Modern Physics*, 55:65–108, 1983.

[4] J. S. Kasper and S. M. Richards. The crystal structures of new forms of silicon and germanium. *Acta Crystallographica*, 17:752, 1964.

[5] R. O. Piltz, J. R. Maclean, S. J. Clark, G. J. Ackland, P. D. Hatton, and J. Crain. Structure and properties of silicon XII: A complex tetrahedrally bonded phase. *Physical Review B*, 52(6):4072–4085, 1995.

[6] J. Crain, G. J. Ackland, J. R. Maclean, R. O. Piltz, P. D. Hatton, and G. S. Pawley. Reversible pressure-induced structural transition between metastable phases of silicon. *Physical Review B*, 50(17):13043–13046, 1994.

[7] B. D. Malone, J. D. Sau, and M. L. Cohen. Ab initio study of the optical properties of Si-XII. *Physical Review B*, 78:161202(R), 2008.

[8] J. M. Besson, E. H. Mokhtari, J. Gonzalez, and G. Weill. Electrical properties of semimetallic silicon III and semiconductive silicon IV at ambient pressure. *Physical Review Letters*, 59(4):473–476, 1987.

[9] S. Minomura and H. G. Drickamer. Pressure induced phase transitions in silicon, germanium and some III-V compounds. *Journal of Physics and Chemistry of Solids*, 23(5):451–456, 1962.

[10] J. C. Jamieson. Crystal structures at high pressures of metallic modifications of silicon and germanium. *Science*, 139:762–764, 1963.

[11] L. Rapp, B. Haberl, C.J. Pickard, J.E. Bradby, E.G. Gamaly, J.S. Williams, and A.V. Rode. Experimental evidence of new tetragonal polymorphs of silicon formed through ultrafast laser-induced confined microexplosion. *Nature Communications*, 6:7555, 2015.

[12] J. S. Kasper and Jr. R. H. Wentorf. Hexagonal (Wurzite) silicon. *Science*, 197(4303):599, 1977.

[13] H. Olijnyk, S. K. Sikka, and W. B. Holzapfel. Structural phase transitions in Si and Ge under pressures up to 50 GPa. *Physics Letters*, 103A(3):137–140, 1984.

[14] M. Hanfland, U. Schwarz, K. Syassen, and K. Takemura. Crystal structure of the high-pressure phase silicon VI. *Physical Review Letters*, 82:1197–1200, 1999.

[15] Y.-X. Zhao, F. Buehler, J. R. Sites, and I. L. Spain. New metastable phases of silicon. *Solid State Communications*, 59(10):679–682, 1986.

[16] S. J. Duclos, Y. K. Vohra, and A. L. Ruoff. Hcp to fcc transition in silicon at 78 GPa and studies to 100 GPa. *Physical Review Letters*, 58:775–777, 1987.

[17] M. I. McMahon and R. J. Nelmes. New high-pressure phase of Si. *Physical Review B*, 47(13):8337–8340, 1993.

[18] R. J. Nelmes, H. Liu, S. A. Belmonte, J. S. Loveday, M. I. McMahon, D. R. Allan, D. Häusermann, and M. Hanfland. *Imma* phase of germanium at ∼80 gpa. *Physical Review B*, 53:R2907–R2909, 1996.

[19] D. Ge, V. Domnich, and Y. Gogotsi. Thermal stability of metastable silicon phases produced by nanoindentation. *Journal of Applied Physics*, 95(5):2725–2731, 2004.

[20] F. P. Bundy and J. S. Kasper. A new dense form of solid germanium. *Science*, 139:340, 1963.

[21] C. H. Bates, F. D, and R. Roy. High-pressure transitions of germanium and a new high-pressure form of germanium. *Science*, 147:860, 1965.

[22] V. V. Brazhkin, A. G. Lyapin, S. V. Popova, and R. N. Voloshin. Solid-phase disordering of bulk Ge and Si samples under pressure. *Journal of Experimental and Theoretical Physics (Pis'ma Zh. Eksp. Teor. Fiz.)*, 56(3):152–156, 1992.

[23] K. Takemura, U. Schwarz, K. Syassen, M. Hanfland, N. E. Christensen, D. L. Novikov, and I. Loa. High-pressure Cmca and hcp phases of germanium. *Physical Review B*, 62:10603–10606, 2000.

[24] B. C. Johnson, B. Haberl, S. Deshmukh, B. D. Malone, M. L. Cohen, J. C. McCallum, J. S. Williams, and J. E. Bradby. Evidence for the **R**8 phase of germanium. *Physical Review Letters*, 110:085502, 2013.

[25] Christopher A. Schuh. Nanoindentation studies of materials. *Materials Today*, 9(5):32 – 40, 2006.

[26] J. Z. Hu, L. D. Merkle, C. S. Menoni, and I. L. Spain. Crystal data for high-pressure phases of silicon. *Physical Review B*, 34(7):4679–4684, 1986.

[27] A. Mujica, Angel Rubio, A. Munõz, and R. J. Needs. High-pressure phases of group-IV, III-V, and II-VI compounds. *Reviews of Modern Physics*, 75(3):863–912, 2003.

[28] J.-T. Wang, C. Chen, H. Mizuseki, and Y. Kawazoe. Kinetic origin of divergent decompression pathways in silicon and germanium. *Physical Review Letters*, 110:165503, 2013.

[29] A. Mujica, C. J. Pickard, and R. J. Needs. Low-energy tetrahedral polymorphs of carbon, silicon, and germanium. *Physical Review B*, 91:214104, 2015.

[30] S. P. Lewis and M. L. Cohen. Theoretical study of high-pressure orthorhombic silicon. *Physical Review B*, 48:16144–16147, 1993.

[31] M. I. McMahon, R. J. Nelmes, R. I. Wright, and D. R. Allan. Pressure dependence of the Imma phase of silicon. *Physical Review B*, 50(2):739–743, 1994.

[32] S. J. Duclos, Y. K. Vohra, and A. L. Ruoff. Experimental study of the crystal stability and equation of state of Si to 248 GPa. *Physical Review B*, 41(17):12012–12028, 1990.

[33] N. Garg, K. K. Pandey, K. V. Shanavas, C. A. Betty, and S. M. Sharma. Memory effect in low-density amorphous silicon under pressure. *Physical Review B*, 83:115202, 2011.

[34] K. K. Pandey, N. Garg, K. V. Shanavas, S. M. Sharma, and S. K. Sikka. Pressure induced crystallization in amorphous silicon. *Journal of Applied Physics*, 109:113511, 2011.

[35] P. F McMillan, M. Wilson, D. Daisenberger, and D. Machon. A density-driven phase transition between semiconducting and metallic polyamorphs of silicon. *Nature Materials*, 4(9):680–684, 2005.

[36] D. Daisenberger, M. Wilson, P. F. McMillan, R. Quesada Cabrera, M. C. Wilding, and D. Machon. High-pressure X-ray scattering and computer simulation studies of density-induced polyamorphism in silicon. *Physical Review B*, 75:224118–1–224118–11, 2007.

[37] O. Shimomura, S. Minomura, N. Sakai, K. Asaumi, K. Tamura, J. Fukushima, and H. Endo. Pressure-induced semiconductor-metal transition in amorphous Si and Ge. *Philosophical Magazine*, 29:547–558, 1974.

[38] B. Haberl, M. Guthrie, D. J. Sprouster, J. S. Williams, and J. E. Bradby. New insight into pressure-induced phase transitions of amorphous silicon: the role of impurities. *Journal of Applied Crystallography*, 46(3):758–768, 2013.

[39] Y. K. Vohra, K. E. Brister, S. Desgreniers, A. L. Ruoff, K. J. Chang, and M. L. Cohen. Phase-transition studies of germanium to 1.25 Mbar. *Physical Review Letters*, 56:1944–1947, 1986.

[40] B. Haberl, M. Guthrie, B.D. Malone, J. S. Smith, S. V. Sinogeikin, M. L. Cohen, J. S. Williams, G. Shen, and J. E. Bradby. Controlled formation of metastable germanium polymorphs. *Physical Review B*, 89:144111, 2014.

[41] K. Tanaka. Amorphous ge under pressure. *Physical Review B*, 43:4302–4307, 1991.

[42] K. Tanaka. Pressure-induced structural transformations in amorphous semiconductors. *Journal of Non-Crystalline Solids*, 150(1):44 – 48, 1992. Proceedings of the Fifth International Conference on the structure of Non-Crystalline Materials (NCM 5).

[43] M. Imai, T. Mitamura, K. Yaoita, and K. Tsuji. Pressure-induced phase transitions of crystalline and amorphous silicon and germanium at low temperatures. *High Pressure Research*, 15:167–189, 1996.

[44] O. I. Barkalov, V. G. Tissen, P. F. McMillan, M. Wilson, A. Sella, and M. V. Nefedova. Pressure-induced transformations and superconductivity of amorphous germanium. *Physical Review B*, 82:020507, 2010.

[45] A. Di Cicco, A. Congeduti, F. Coppari, J. C. Chervin, F. Baudelet, and A. Polian. Interplay between morphology and metallization in amorphous-amorphous transitions. *Physical Review B*, 78:033309, 2008.

[46] E. Principi, A. Di Cicco, F. Decremps, A. Polian, S. De Panfilis, and A. Filipponi. Polyamorphic transition of germanium under pressure. *Physical Review B*, 69:201201, 2004.

[47] M. Durandurdu and D. A. Drabold. First-order pressure-induced polyamorphism in germanium. *Physical Review B*, 66:041201, 2002.

[48] F. Coppari, J. C. Chervin, A. Congeduti, M. Lazzeri, A. Polian, E. Principi, and A. Di Cicco. Pressure-induced phase transitions in amorphous and metastable crystalline germanium by raman scattering, x-ray spectroscopy, and ab initio calculations. *Physical Review B*, 80:115213, 2009.

[49] S. Minomura. Pressure-induced transitions in amorphous silicon and germanium. *Journal de Physique Colloques*, 42:C4–181–C4–188, 1981.

[50] K. Tsuji, J. Katayama, N. Koyama, Y. Yamamoto, J.-Q. Cheng, and M. Imai. Amorphization from quenched high-pressure phases in tetrahedrally bonded materials. *Journal of Non-Crystalline Solids*, 156-158:540–543, 1993.

[51] C. Kittel. *Introduction to Solid State Physics*. Wiley, 2004.

[52] Haidong Zhang, Hanyu Liu, Kaya Wei, Oleksandr O. Kurakevych, Yann Le Godec, Zhenxian Liu, Joshua Martin, Michael Guerrette, George S. Nolas, and Timothy A. Strobel. Bc8 silicon (si-iii) is a narrow-gap semiconductor. *Physical Review Letters*, 118:146601, 2017.

[53] S. Ruffell, K. Sears, J. E. Bradby, and J. S. Williams. Room temperature writing of electrically conductive and insulating zones in silicon by nanoindentation. *Applied Physics Letters*, 98(5):052105, 2011.

[54] S. Wong. *Controlling Indentation-induced Phases of Silicon*. PhD thesis, Australian National University, 2018.

[55] B. D. Malone, J. D. Sau, and M. L. Cohen. Ab initio survey of the electronic structure of tetrahedrally bonded phases of silicon. *Physical Review B*, 78:035210, 2008.

[56] C. Rödl, T. Sander, F. Bechstedt, J. Vidal, P. Olsson, S. Laribi, and J.-F. Guillemoles. Wurtzite silicon as a potential absorber in photovoltaics: Tailoring the optical absorption by applying strain. *Physical Review B*, 92:045207, 2015.

[57] B. D. Malone and M. L. Cohen. Electronic structure, equation of state, and lattice dynamics of low-pressure Ge polymorphs. *Physical Review B*, 86:054101, 2012.

[58] A. Mujica and R. J. Needs. First-principles calculations of the structural properties, stability, and band structure of complex tetrahedral phases of germanium: St12 and bcs. *Physical Review B*, 48:17010, 1993.

[59] S Q Wang and H Q Ye. First-principles study on the lonsdaleite phases of c, si and ge. *Journal of Physics: Condensed Matter*, 15(12):L197, 2003.

[60] J. D. Joannopoulos and M. L. Cohen. Electronic properties of complex crystalline and amorphous phases of ge and si. i. density of states and band structures. *Physical Review B*, 7:2644, 1973.

[61] Z. Zhao, H. Zhang, D. Y. Kim, W. Hu, E. S. Bullock, and T. A. Strobel. Properties of the exotic metastable ST12 germanium allotrope. *Nature Communications*, 8, 2017.

[62] L. Q. Huston, B. C. Johnson, B. Haberl, S. Wong, J. S. Williams, and J. E. Bradby. Thermal stability of simple tetragonal and hexagonal diamond germanium. *Journal of Applied Physics*, 122(17):175108, 2017.

[63] S. Wippermann, M. Vörös, D. Rocca, A. Gali, G. Zimanyi, and G. Galli. High-pressure core structures of Si nanoparticles for solar energy conversion. *Physical Review Letters*, 110:046804, 2013.

[64] R. J. Kobliska and S. A. Solin. Raman spectrum of wurtzite silicon. *Physical Review B*, 8:3799–3802, 1973.

[65] R. H. Wentorf, Jr. and J. S. Kasper. Two new forms of silicon. *Science*, 139(3552):338–339, 1963.

[66] R. J. Nelmes, M. I. McMahon, N. G. Wright, D. R. Allan, and J. S. Loveday. Stability and crystal structure of bc8 germanium. *Physical Review B*, 48:9883, 1993.

[67] R. J. Kobliska, S. A. Solin, M. Selders, R. K. Chang, R. Alben, Thorpe M. F, and D. Weaire. Raman scattering from phonons in polymorphs of si and ge. *Physical Review Letters*, 29(11):725–728, 1972.

[68] S. J. Kim, O. K. Quy, L-S. Chang, E. A. Stach, C. A. Handwerker, and Al. Wei. Formation of the st12 phase in nanocrystalline ge at ambient pressure. *Journal of Materials Chemistry*, 20:331–337, 2010.

[69] I. V. Gridneva, Y. V. Milman, and V. I. Trefilov. Phase transition in diamond-structure crystals during hardness measurements. *Physica Status Solidi A: Applied Research*, 14:177–182, 1972.

[70] A. P. Gerk and D. Tabor. Indentation hardness and semiconductor-metal transition of germanium and silicon. *Nature*, 271:732–733, 1978.

[71] G. M. Pharr, W. C. Oliver, R. F. Cook, P. D. Kirchner, M. C. Kroll, T. R. Dinger, and D. R. Clarke. Electrical resistance of metallic contacts on silicon and germanium during indentation. *Journal of Materials Research*, 7(4):961–971, 1992.

[72] Y. B. Gerbig, C. A. Michaels, and R. F. Cook. In situ observation of the spatial distribution of crystalline phases during pressure-induced transformations of indented silicon thin films. *Journal of Materials Research*, 30(3):390–406, 2015.

[73] E. R. Weppelmann, J. S. Field, and M. V. Swain. Observation, analysis, and simulation of the hysteresis of silicon using ultra-micro-indentation with spherical indenters. *Journal of Materials Research*, 8(4):830–840, 1993.

[74] E. R. Weppelmann, J. S. Field, and M. V. Swain. Influence of spherical indentor radius on the indentation-induced transformation behaviour of silicon. *Journal of Materials Science*, 30(9):2455–2462, 1995.

[75] V. Domnich, Y. Gogotsi, and S. Dub. Effect of phase transformations on the shape of the unloading curve in the nanoindentation of silicon. *Applied Physics Letters*, 76(16):2214–2216, 2000.

[76] J. E. Bradby, J. S. Williams, J. Wong-Leung, M. V. Swain, and P. Munroe. Mechanical deformation in silicon by micro-indentation. *Journal of Materials Research*, 16(5):1500–1507, 2001.

[77] S. Wong, B. Haberl, B. C. Johnson, A. Mujica, M. Guthrie, J. C. McCallum, J. S. Williams, and J. E. Bradby. Formation of an r8-dominant si material. *Physical Review Letters*, 122:105701, 2019.

[78] J. E. Bradby, J. S. Williams, J. Wong-Leung, M. V. Swain, and P. Munroe. Transmission electron microscopy observation of deformation microstructure under spherical indentation in silicon. *Applied Physics Letters*, 77(23):3749–3751, 2000.

[79] I. Zarudi, L. C. Zhang, and M. V. Swain. Behavior of monocrystalline silicon under cyclic microindentation with a spherical indenter. *Applied Physics Letters*, 82(7):1027–1029, 2003.

[80] I. Zarudi and L. C. Zhang. Structure changes in mono-crystalline silicon subjected to indentation — experimental findings. *Tribology International*, 32(12):701 – 712, 1999.

[81] D. Chrobak, Kwang-Ho Kim, K. J. Kurzydłowski, and R. Nowak. Nanoindentation experiments with different loading rate distinguish the mechanism of incipient plasticity. *Applied Physics Letters*, 103(7):072101, 2013.

[82] B. Haberl, J. E. Bradby, M. V. Swain, J. S. Williams, and P. Munroe. Phase transformations induced in relaxed amorphous silicon by indentation at room temperature. *Applied Physics Letters*, 85(23):5559–5561, 2004.

[83] S. Ruffell, J. Vedi, J. E. Bradby, J. S. Williams, and B. Haberl. Effect of oxygen concentration on nanoindentation-induced phase transformations in ion-implanted amorphous silicon. *Journal of Applied Physics*, 105:083520, 2009.

[84] B. Haberl, J. E. Bradby, S. Ruffell, J. S. Williams, and P. Munroe. Phase transformations induced by spherical indentation in ion-implanted amorphous silicon. *Journal of Applied Physics*, 100:013520–1–013520–9, 2006.

[85] E. P. Donovan, F. Spaepen, D. Turnbull, J. M. Poate, and D. C. Jacobson. Calorimetric studies of crystallization and relaxation of amorphous Si and Ge prepared by ion implantation. *Journal of Applied Physics*, 57(6):1795–1804, 1985.

[86] J. E. Bradby, J. S. Williams, J. Wong-Leung, M. V. Swain, and P. Munroe. Nanoindentation-induced deformation of ge. *Applied Physics Letters*, 80:2651, 2002.

[87] D. J. Oliver, J. E. Bradby, J. S. Williams, M. V. Swain, and P. Munroe. Rate-dependent phase transformations in nanoindented germanium. *Journal of Applied Physics*, 105:126101, 2009.

[88] G. M. Pharr, W. C. Oliver, and D. S. Harding. Electrical resistance of metallic contacts on silicon and germanium during indentation. *Journal of Materials Research*, 6(6):1129–1130, 1991.

[89] Y. Gogotsi, V. Domnich, S. N. Dub, A. Kailer, and K.G. Nickel. Cyclic nanoindentation and Raman microspectroscopy study of phase transformations in semiconductors. *Journal of Materials Research*, 15(4):871–879, 2000.

[90] J. Jang, M. J. Lance, S. Wen, and G. M. Pharr. Evidence for nanoindentation-induced phase transformations in germanium. *Applied Physics Letters*, 86(13), 2005.

[91] Koji Kosai, Hu Huang, and Jiwang Yan. Comparative study of phase transformation in single-crystal germanium during single and cyclic nanoindentation. *Crystals*, 7(11), 2017.

[92] S. Deshmukh, B. Haberl, S. Ruffell, P. Munroe, J. S. Williams, and J. E. Bradby. Phase transformation pathways in amorphous germanium under indentation pressure. *Journal of Applied Physics*, 115(15), 2014.

[93] J. S. Williams, B. Haberl, S. Deshmukh, B. C. Johnson, B. D. Malone, M. L. Cohen, and J. E. Bradby. Hexagonal germanium formed via a pressure-induced phase transformation of amorphous germanium under controlled nanoindentation. *Physica Status Solidi RRL*, 7:355, 2013.

[94] S. H. Tolbert, A. B. Herhold, L. E. Brus, and A. P. Alivisatos. Pressure-induced structural transformation in Si nanocrystals: Surface and shape effects. *Physical Review Letters*, 76(23):4384–4387, 1996.

[95] Y. Ikoma, K. Kumano, K. Edalati, K. Saito, Q. Guo, and Z. Horita. Phase transformation of germanium by processing through high-pressure torsion: strain and temperature effects. *Philosophical Magazine Letters*, 97(1):27–34, 2017.

[96] A. Kailer, K. G. Nickel, and Y. G. Gogotsi. Raman microspectroscopy of nanocrystalline and amorphous phases in hardness indentations. *Journal of Raman Spectroscopy*, 30:939–946, 1999.

[97] S. Ruffell, J. Vedi, J. E. Bradby, and J. S. Williams. Effect of hydrogen on nanoindentation-induced phase transformations in amorphous silicon. *Journal of Applied Physics*, 106:123511, 2009.

[98] V. Domnich and Y. Gogotsi. Phase transformations in silicon under contact loading. *Reviews on Advanced Materials Science*, 3:1–36, 2002.

[99] S. Ruffell, J. E. Bradby, J. S. Williams, and P. Munroe. Formation and growth of nanoindentation-induced high pressure phases in crystalline and amorphous silicon. *Journal of Applied Physics*, 102:063521/1–8, 2007.

[100] M. Imai, K. Yaoita, Y. Katayama, J.-Q. Chen, and K. Tsuji. Amorphization from the quenched high-pressure phase of silicon and germanium. *Journal of Non-Crystalline Solids*, 150:49–52, 1992.

[101] V. V. Brazhkin, A. G. Lyapin, S. V. Popova, and R. N. Voloshin. Non-equilibrium phase transitions and amorphization in Si, Si/GaAs, Ge and Ge/GaSb at the decompression of high pressure phases. *Physical Review B*, 51(12):7549–7554, 1995.

[102] B. Haberl, M. G., S. V. Sinogeikin, G. Shen, J. S. Williams, and J. E. Bradby. Thermal evolution of the metastable r8 and bc8 polymorphs of silicon. *High Pressure Research*, 35(2):99–116, 2015.

[103] G. A. Voronin, C. Pantea, T. W. Zerda, J. Zhang, L. Wang, and Y. Zhao. In situ X-ray diffraction study of germanium at pressures up to 11 GPa and temperatures up to 950 K. *Journal of Physics and Chemistry of Solids*, 64(11):2113–2119, 2003.

[104] P. Pirouz, U. Dahmen, K.H. Westmacott, and R. Chaim. The martensitic transformation in silicon—iii. comparison with other work. *Acta Metallurgica et Materialia*, 38(2):329 – 336, 1990.

[105] Eremenko V. G. and Nikitenko V. I. Electron microscope investigation of the microplastic deformation mechanisms of silicon by indentation. *physica status solidi (a)*, 14(1):317–330, 1972.

[106] V. Domnich, Y. Aratyn, W. M. Kriven, and Y. Gogotsi. Temperature dependence of silicon hardness: Experimental evidence of phase transformations. *Reviews on Advanced Materials Science*, 17:33–41, 2008.

[107] M.S.R.N. Kiran, T.T. Tran, L.A. Smillie, B. Haberl, D. Subianto, J.S. Williams, and J.E. Bradby. Temperature-dependent mechanical deformation of silicon at the nanoscale: Phase transformation versus defect propagation. *Journal of Applied Physics*, 117(20), 2015.

[108] S. Bhattacharyya, D. Churochkin, and R. M. Erasmus. Anomalous raman features of silicon nanowires under high pressure. *Applied Physics Letters*, 97:141912, 2010.

[109] Yuejian Wang, Jianzhong Zhang, Ji Wu, Jeffrey L. Coffer, Zhijun Lin, Stanislav V. Sinogeikin, Wenge Yang, and Yusheng Zhao. Phase transition and compressibility in silicon nanowires. *Nano Letters*, 8(9):2891–2895, 2008.

[110] H. K. Poswal, N Garg, S. M. Sharma, E. Busetto, S. K Sikka, G. Gundiah, F. L. Deepak, and C. N. R. Rao. Pressure-induced structural phase transformations in silicon nanowires. *Journal of Nanoscience and Nanotechnology*, 5(5):729–732, 2005.

[111] N. R. C. Corsini, Y. Zhang, W. R. Little, A. Karatutlu, O. Ersoy, P. D. Haynes, C. Molteni, N. D. M. Hine, I. Hernandez, J. Gonzalez, F. Rodriguez, V. V. Brazhkin, and A. Sapelkin. Pressure-induced amorphization and a new high density amorphous metallic phase in matrix-free ge nanoparticles. *Nano Letters*, 15(11):7334–7340, 2015.

[112] H. Wang, J. F. Liu, Y. He, Y. Wang, W. Chen, J. Z. Jiang, J. Staun Olsen, and L. Gerward. High-pressure structural behaviour of nanocrystalline ge. *Journal of Physics: Condensed Matter*, 19(15):156217, 2007.

[113] Y. Wang, W. Yang, G. Zou, J. Wu, J. L. Coffer, S. V. Sinogeikin, and J. Zhang. Anomalous surface doping effect in semiconductor nanowires. *The Journal of Physical Chemistry C*, 121(21):11824–11830, 2017.

[114] S. Wong, B. Haberl, J. S. Williams, and J. E. Bradby. Phase transformation as the single-mode mechanical deformation of silicon. *Applied Physics Letters*, 106(25):252103, 2015.

[115] A.C. Fischer-Cripps. *Nanoindentation*. Springer-Verlag, New York, 2004.

[116] W. C. Oliver and G. M. Pharr. An improved technique for determining hardness and elastic modulus using load and displacement sensing indentation experiments. *Journal of Materials Research*, 7(6):1564–1583, 1992.

[117] Y. Ganesan, Y. Lu, C. Peng, H. Lu, R. Ballarini, and J. Lou. Development and application of a novel microfabricated device for the in situ tensile testing of 1-d nanomaterials. *Journal of Microelectromechanical Systems*, 19(3):675–682, 2010.

[118] S. Shim, H. Bei, M.K. Miller, G.M. Pharr, and E.P. George. Effects of focused ion beam milling on the compressive behavior of directionally solidified micropillars and the nanoindentation response of an electropolished surface. *Acta Materialia*, 57(2):503 – 510, 2009.

[119] R. Branco, E-J. Pearsall, C. A. Rundle, R. G. White, J. E. Bradby, and A. R. Hardham. Quantifying the plant actin cytoskeleton response to applied pressure using nanoindentation. *Protoplasma*, 254(2):1127–1137, 2017.

[120] J. C. Trenkle, C. E. Packard, and C. A. Schuh. Hot nanoindentation in inert environments. *Review of Scientific Instruments*, 81(7):073901, 2010.

[121] Hysitron. http://www.hysitron.com.

[122] R. Boehler. Diamond cells and new materials. *Materials Today*, 8(11):34 – 42, 2005.

[123] R. Boehler. New diamond cell for single-crystal x-ray diffraction. *Review of Scientific Instruments*, 77(11):115103, 2006.

[124] Diacell SymmDAC 60. https://diamondanvils.com/shop/diamond-anvil-cells/diacell-symmdac-60/.

[125] D J Dunstan and I L Spain. Technology of diamond anvil high-pressure cells: I. principles, design and construction. *Journal of Physics E: Scientific Instruments*, 22(11):913–923, 1989.

[126] E. Soignard and P. F. McMillan. An introduction to diamond anvil cells and loading techniques. In Andrzej Katrusiak and Paul McMillan, editors, *High-Pressure Crystallography*, pages 81–100, Dordrecht, 2004. Springer Netherlands.

[127] G. J. Piermarini, S. Block, and J.D. Barnett. Hydrostatic limits in liquids and solids to 100 kbar. *Journal of Applied Physics*, 44(12):5377–5382, 1973.

[128] J. D. Barnett, S. Block, and G. J. Piermarini. a. *Review of Scientific Instruments*, 44(1):1–9, 1973.

[129] A. Dewaele, M. Torrent, P. Loubeyre, and M. Mezouar. Compression curves of transition metals in the mbar range: Experiments and projector augmented-wave calculations. *Physical Review B*, 78:104102, 2008.

[130] S. V. Sinogeikin, J. S. Smith, E. Rod, C. Lin, C. Kenney-Benson, and G. Shen. Online remote control systems for static and dynamic compression and decompression using diamond anvil cells. *Review of Scientific Instruments*, 86(7):072209, 2015.

[131] H.A. Szymanski. *Raman Spectroscopy Theory and Practice*. Springer US, 1 edition, 1967.

[132] D. A. Lang, editor. *Raman Spectroscopy*. McGraw-Hill International Book Company, London, 1977.

[133] G. Shen, P. Chow, Y. Xiao, S. Sinogeikin, Y. Meng, W. Yang, H-P. Liermann, O. Shebanova, E. Rod, A. Bommannavar, and H-K. Mao. HPCAT: an integrated high-pressure synchrotron facility at the advanced photon source. *High Pressure Research*, 28(3):145–162, 2008.

[134] C. Prescher and V. B. Prakapenka. Dioptas: a program for reduction of two-dimensional x-ray diffraction data and data exploration. *High Pressure Research*, 35(3):223–230, 2015.

[135] M. Dufek. Helios NanaLab 450/450S/450ML/650/600i User Operation Manual, 2012.

[136] D. B. Williams and C. B. Carter, editors. *Transmission Electron Microscopy*. Springer US, USA, 1996.

[137] L. A. Giannuzzi, editor. *Introduction to Focused Ion Beams*. Springer US, USA, 2005.

[138] R. M. Langford and A. K. Petford-Long. Preparation of transmission electron microscopy cross-section specimens using focused ion beam milling. *Journal of Vacuum Science and Technology A*, 19(5):2186–2193, 2001.

[139] Sevak Khachadorian, Konstantinos Papagelis, Harald Scheel, Alan Colli, Andrea C Ferrari, and Christian Thomsen. High pressure Raman scattering of silicon nanowires. *Nanotechnology*, 22(19), 2011.

[140] R. S. Wagner and W. C. Ellis. Vapor liquid solid mechanism of single crystal growth. *Applied Physics Letters*, 4(5):89–90, 1964.

[141] B. A. Weinstein and G. J Piermarini. Raman scattering and phonon dispersion in Si and GaP at very high pressure. *Physical Review B*, 12(4):1172–1186, 1975.

[142] H. Olijnyk. Raman scattering in metallic Si and Ge up to 50 GPa. *Physical Review Letters*, 68(14):2232, 1992.

[143] H. Olijnyk and A. P. Jephcoat. Effect of pressure on Raman spectra of metastable phases of Si and Ge. *Physica Status Solidi (B): Basic Solid State Physics*, 211:413–420, 1999.

[144] S. H. Tolbert and A. P. Alivisatos. The wurtzite to rock salt structural transformation in cdse nanocrystals under high pressure. *The Journal of Chemical Physics*, 102(11):4642–4656, 1995.

[145] L. Vincent, D. Djomani, M. Fakfakh, C. Renard, B. Belier, D. Bouchier, and G. Patriarche. Shear-driven phase transformation in silicon nanowires. *Nanotechnology*, 29(12):125601, 2018.

[146] R. Hrubiak, S. Sinogeikin, E. Rod, and G. Shen. The laser micro-machining system for diamond anvil cell experiments and general precision machining applications at the High Pressure Collaborative Access Team. *Review of Scientific Instruments*, 86(7), 2015.

[147] M. Rivers, V. B. Prakapenka, A. Kubo, C. Pullins, C. M. Holl, and S. D. Jacobsen. The compres/gsecars gas-loading system for diamond anvil cells at the advanced photon source. *High Pressure Research*, 28(3):273–292, 2008.

[148] Y. Fei, A. Ricolleau, M. Frank, K. Mibe, G. Shen, and V. Prakapenka. Toward an internally consistent pressure scale. *PNAS*, 104(22):9182–9186, 2007.

[149] R. Hrubiak, J. S. Smith, and G. Shen. Multimode scanning x-ray diffraction microscopy for diamond anvil cell experiments. *Review of Scientific Instruments*, 90(2):025109, 2019.

[150] E. Nygren, M. J. Aziz, D. Turnbull, J. M. Poate, D. C. Jacobson, and R. Hull. Effect of pressure on the solid phase epitaxial regrowth rate of Si. *Applied Physics Letters*, 47(3):232–233, 1985.

[151] G. Q. Lu, E. Nygren, M. J. Aziz, D. Turnbull, and C. W. White. Pressure-enhanced solid phase epitaxy of germanium. *Applied Physics Letters*, 56(2):137–139, 1990.

[152] G. Q. Lu, E. Nygren, and M. J. Aziz. Pressure-enhanced crystallization kinetics of amorphous Si and Ge: Implications for point-defect mechanisms. *Journal of Applied Physics*, 70(10):5323–5345, 1991.

[153] S. Ruffell, J. E. Bradby, J. S. Williams, D. Munoz-Paniagua, S. Tadayyon, L. L. Coatsworth, and P. R. Norton. Nanoindentation-induced phase transformations in silicon at elevated temperatures. *Nanotechnology*, 20(13):135603, 2009.

[154] F. Datchi, A. Dewaele, P. Loubeyre, R. Letoullec, Y. Le Godec, and B. Canny. Optical pressure sensors for high-pressure–high-temperature studies in a diamond anvil cell. *High Pressure Research*, 27(4):447–463, 2007.

[155] M. S. R. N. Kiran, B. Haberl, J. S. Williams, and J. E. Bradby. Temperature dependent deformation mechanisms in pure amorphous silicon. *Journal of Applied Physics*, 115(11):113511, 2014.

[156] J. E. Bradby. *Nanoindentation-Induced Deformation of Semiconductors*. PhD thesis, Australian National University, 2002.

[157] G. L. Olson and J. A. Roth. Kinetics of solid phase crystallization in amorphous silicon. *Materials Science Reports*, 3(1):1–77, 1988.

[158] K.V. Ravi. Crystallographic defects in epitaxial silicon films. *Thin Solid Films*, 31(1):171 – 183, 1976.

[159] L. Csepregi, E. F. Kennedy, J. W. Mayer, and T. W. Sigmon. Substrate-orientation dependence of the epitaxial regrowth rate from si-implanted amorphous si. *Journal of Applied Physics*, 49(7):3906–3911, 1978.

[160] D. N. Batchelder, D. L. Losee, and R. O. Simmons. Isotope effects in the lattice constant and thermal expansion of ^{20}Ne and ^{22}Ne single crystals. *Physical Review*, 173:873–880, 1968.

[161] S. Karthika, T. K. Radhakrishnan, and P. Kalaichelvi. A review of classical and nonclassical nucleation theories. *Crystal Growth & Design*, 16(11):6663–6681, 2016.

[162] T. Juliano, Y. Gogotsi, and V. Domnich. Effect of indentation unloading conditions on phase transformation induced events in silicon. *Journal of Materials Research*, 18(5):1192, 2003.

[163] C. Zeiner. *Germanium Nanowire Heterostructures and Devices*. PhD thesis, Technischen Universitatat Wien, 2014.

[164] B. Haberl. personal communication, March 2019.

[165] R. C. Weast, editor. *CRC Handbook of Chemistry and Physics*. CRC Press, 61 edition, 1988.

[166] B. C. Johnson, P. Gortmaker, and J. C. McCallum. Intrinsic and dopant-enhanced solid-phase epitaxy in amorphous germanium. *Physical Review B*, 77:214109, 2008.